Simulation and optimization of the in-service behavior of coated inserts for turning and milling

Dissertation

zur Erlangung des akademischen Grades

Doktor der montanistischen Wissenschaften

an der Montanuniversität Leoben

eingereicht von

Ivan Krajinović

Institut für Mechanik

Montanuniversität Leoben

July, 2016

All this would not be possible without mercy and love for this sinful man that I am of our God, Father, Son and Holy Spirit. Without Holy Virgin Mary and St. Joseph, St. Thomas Aquinas, St. John the Apostle, St. John the Baptist, St. John of the Cross, St. Thérèse of Lisieux and all the other saints to who I pleaded for help in hours of need this work would not be done.

Abstract

Within this work, a state-of-the-art finite element approach to the problem of the tool loading during milling processes is presented. The studied tool is based on an industrial hard coated fine-grained hard metal tool with 8 wt.% Co. The Arbitrary Lagrangian-Eulerian formulation of the continuum is used to create 2D orthogonal cutting and 2D milling models. The whole milling process over several cycles of cutting and cooling is studied using a 3D tool milling process model. Measured and literature based thermal and mechanical material parameters are used to describe the material behavior of the coatings and the substrate.

The 2D orthogonal cutting model is validated by comparing to the orthogonal cutting experiments at different cutting speeds and cutting depths. The results show that the 2D ALE cutting model can be used for modeling of the tool loading.

The 2D milling model is created as a tool box for parametric studies which provide guidelines for design of the tool design. It shows the importance of coatings as a thermal shield which decreases the plastic deformation of the hard metal substrate. Also, the model enables to study the influence of the tool loading on the hard metal substrates with different thermo-mechanical properties. The role of friction as a source of heat and damage is studied, too.

The 3D tool milling process model allows investigating the behavior of stress-strain-temperature fields during multiple milling cycles. It shows the build-up of tensile out-of-plane stresses during cooling parts of the cycles. These stresses are responsible for the creation of combcracks which limit the tool service life. The build-up of tensile out-of-plane stresses occurs in the same region as experimentally discovered. The model also gives an insight in the plastic deformation of the substrate during the first milling cycles under conditions of high von Mises stresses and relatively low temperatures.

Zusammenfassung

Diese Arbeit behandelt Finite Elemente Modellierungen eines Fräsprozesses, um die Werkzeugbelastungen zu bestimmen. Die Arbeit untersucht vor allem die Belastung eines beschichteten Hartmetallwerkzeugs, dessen Substrat aus feinkörnigem zementiertem Wolframkarbid mit 8% Kobalt Anteil besteht. Eine „Arbitrary Lagrangian-Eulerian" (ALE) Formulierung wurde für die kontinuumsmechanische Modellierung des zweidimensionalen Schneid- und Fräsmodells verwendet. Der gesamte Fräsprozess wurde auch dreidimensional modelliert. Dabei wurden mehrere Zyklen untersucht, wobei ein Zyklus aus dem Schneid- und einem Abkühlungsprozess besteht. Für die Materialparameter der Beschichtung als auch des Substrates wurden sowohl gemessene als auch Literaturwerte verwendet.

Das orthogonale Schneidmodell wurde für mehrere Schneidgeschwindigkeiten und Schneidtiefen validiert. Es konnte gezeigt werden, dass eine Schneidsimulation mit ALE Formulierung die Werkzeugbelastung gut widerspiegelt.

Das zweidimensionale Fräsmodell wurde als Simulationssystem entwickelt, das über parametrische Studien Richtlinien für das Design von Werkzeugen liefert. Die Simulationen zeigen die Bedeutung der Beschichtungen als thermische Schilder auf. Durch diesen thermischen Schutz erfolgt eine geringere Plastizierung im Hartmetall. Die Werkzeugbelastung kann für unterschiedliche thermo-mechanische Materialparameter ermittelt werden. Auch der Einfluss unterschiedlicher Reibwerte zwischen Werkstück und Beschichtung auf die Temperatur- und damit Schädigungsentwicklung wurde untersucht.

Das dreidimensionale Fräsprozessmodell erlaubt die Berechnung von Spannungs- und Dehnungsfeldern in Abhängigkeit vom Prozessverlauf, d.h. Aufheiz- und Abkühlprozesse während mehrerer Fräsvorgänge. Durch die dreidimensionale Modellierung können die Spannungen in der dritten Raumrichtung erfasst werden, welche während des Abkühlvorganges entstehen. Diese Spannungen sind für die Entstehung von Kammrissen verantwortlich, welche sehr oft die Lebenszeit des Werkzeuges beenden. Das Modell berechnet die höchsten Spannungen an den Stellen des Werkzeuges, an denen auch die Bildung von Kammrissen festgestellt wird. Das Modell beschreibt auch die plastische Verformung im Inneren des Substrats während der ersten Fräszyklen. Diese Verformungen entstehen bei sehr hohen Vergleichsspannungen bei gleichzeitig niederen Temperaturen.

Affidavit

I declare in lieu of oath, that I wrote this thesis and performed associated research myself, using only literature cited in this volume.

Leoben, December 2015

Ivan Krajinović

Content

1 Introduction

1.1 Introduction to cutting

Machining of metals is an important industrial process which consumes a significant amount of energy, time and money. This process produces the desired shapes of metal objects from bulk material. It is indispensable for example in automotive, aviation or arms industry.

Cutting processes of metals are very complex. Both the cutting tool and the workpiece are subjected to extreme loading conditions which influence the tool service life and the quality of the machined surfaces. There are several parameters characterizing these conditions. The most important parameter is the heat generated between the chip and the tool during cutting. Other parameters of importance are contact conditions between the tool and the workpiece like friction coefficient dependent on the shear stress or contact pressure. Cutting speed, type of the workpiece material and tool materials and their coating play also major roles during cutting. All these parameters are mutually interdependent and interconnected. It is in fact hard to distinguish which parameter influences what and to what extent.

In the past, most of the improvements in metal cutting were achieved using a trial and error method in more or less sophisticated experimental set-ups. With the development of science in the 19th century first mathematical models were suggested by Ernest and Merchant [1]. These models were developed by Zvorykin and others but due to the complexity of the cutting process and some limitations of their description of the cutting process, their outcome was limited, too. With an improvement of the technological possibilities more sophisticated experiments emerged. Precise measurement of cutting forces or temperatures became available. The experiments were now able to provide a better understanding of such an interconnected system. However, due to its complexity, they still cannot reproduce the full picture. Understanding of the cutting process benefited much from the development of computers which enabled application of different numerical theories for the description of the cutting problem. Previously it was impossible to use these theories due to fact that there is no simple analytical solution to their governing equations. The numerical approach enhances understanding and can provide detailed insight in the process. In combination with an experimental investigation it is a powerful tool for prediction and optimization of the cutting process.

The work presented in this manuscript was part of a bigger project which involved three PhD students and several senior scientists. The goal of the project was to obtain a better knowledge of the tool loading and its damage process in a real industrial milling process. The project was divided into three parts. One was dealing experimentally with the substrate of the tool consisting of hard metals. The second dealt again experimentally with hard coatings. Such coatings are used to extend the tool service life. This work at hand describes the third part of the project. In this work numerical simulations are used to combine knowledge gained from experiments and measurements into the models of the milling process. The created models allow not only the detailed and quantitative investigation of the coated tool loading but also provides a detailed physically based insight expressed in terms of temperature, stress and plastic strain into the tool behavior during milling.

The numerical approach chosen here is based on the Finite Element Method (FEM) which has proven as a reliable method in many fields, and in combination with modern software it is a powerful tool for solving engineering problems.

To simulate cutting processes several methods are available within FEM. These are e. g. the Eulerian, Lagrangian and Arbitrary Eulerian-Lagrangian method. Each has its own strengths and weaknesses which will be described later. Here the choice is the Arbitrary Eulerian-Lagrangian method which combines the advantages of the other two methods and also provides stable procedures for taking into account the contact conditions which are most important for the investigation of the tool load.

A part of this work is also dedicated to present and discuss the thermo-physical properties of the workpiece, hard coatings and hard metals. To obtain precise numerical results it is essential to use realistic models for the behavior of the materials. Most of the presented thermo-physical values are experimentally obtained in the related project parts and are available for the first time.

The milling process is modeled in 2D. As mentioned, the ALE method is used. For validation of this approach the milling model has been modified to be usable as a turning model and the results were then compared to orthogonal cutting tests at several cutting depths and speeds. The milling model itself is validated by comparing the numerical results to the milling experiments.

The 2D milling model is used for a detailed study of the different influences of process parameters on the tool loading. The influence of coatings, substrates, friction

coefficients and geometries is calculated. This study provides guidelines for the design of optimized tools.

A further task within the project is the description of the formation of combcracks. Such cracks are observed at the rake face of the tool during cutting or milling. The combcracks propagate in planes perpendicular to the cutting edge of the tool. To study this kind of cracks a 3D tool process model has to be developed. A reason for the formation of combcracks is assumed to be tensile stresses developing in a direction normal to their formation i.e. out-of-plane stresses to the cutting plane. The numerical results show that the out-of plane stresses grow during milling and form in a similar area as obtained in experiments.

1.2 Overview of the milling model
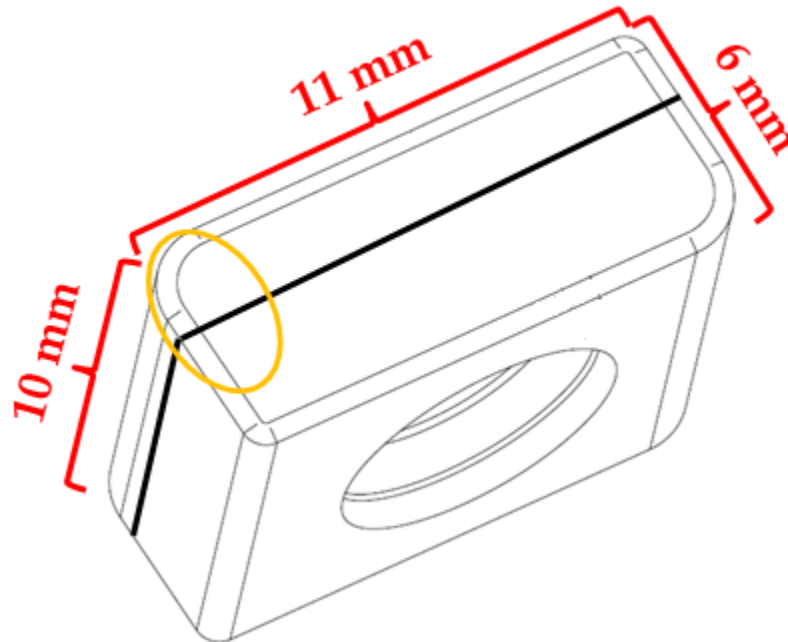
Figure 1: A scheme of the milling insert. The black line indicates the plane which is used in 2D milling simulations. The upper surface of the tool is the rake face and the left surface is the flank face of the tool. The orange ellipse indicates the area of the tool which removes the workpiece material during milling.

The Figure 1 presents the milling tool whose loading is studied. Its dimensions are 10×11×6 mm³. It is attached to the miller's head with a screw through the hole visible at the lower front side. The milling is done only with the corner part of the whole insert and this part is marked with an orange ellipse. Milling simulations done in this work are made in 2D as geometrical representation of a 3D reality. The thick black lines indicate the plane of the 2D model.

At the beginning the milling model consists of two parts, the tool and the workpiece. The milling process produces the third part, the chip. The chip and the workpiece are separated by a shearing line, see Figure 2.

Some important geometrical issues of the model are presented in Figure 2. The flank face is the face of the tool closer to the workpiece surface produced by milling. The flank face and the workpiece surface enclose the flank angle. The rake face is the face of the tool which is in direct contact with the chip. This part of the tool is of special interest due to the fact that most of the loading and also the main tool wear happens on this face.

The rake angle is the angle between a line perpendicular to the surface of the workpiece produced by milling and the rake face. The flank and rake faces are connected at the tool edge. The tool edge can be modeled as a sharp corner or it can have a radius which is more realistic. Above the tool edge there is a chamfered edge which is a specific design part of this particular tool.
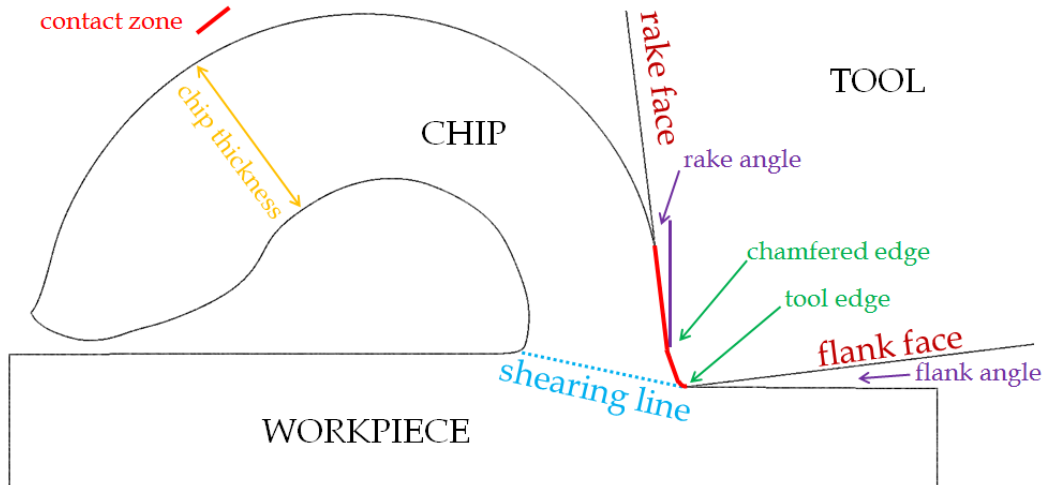
Figure 2: A scheme of a 2D geometrical representation of a cutting model.
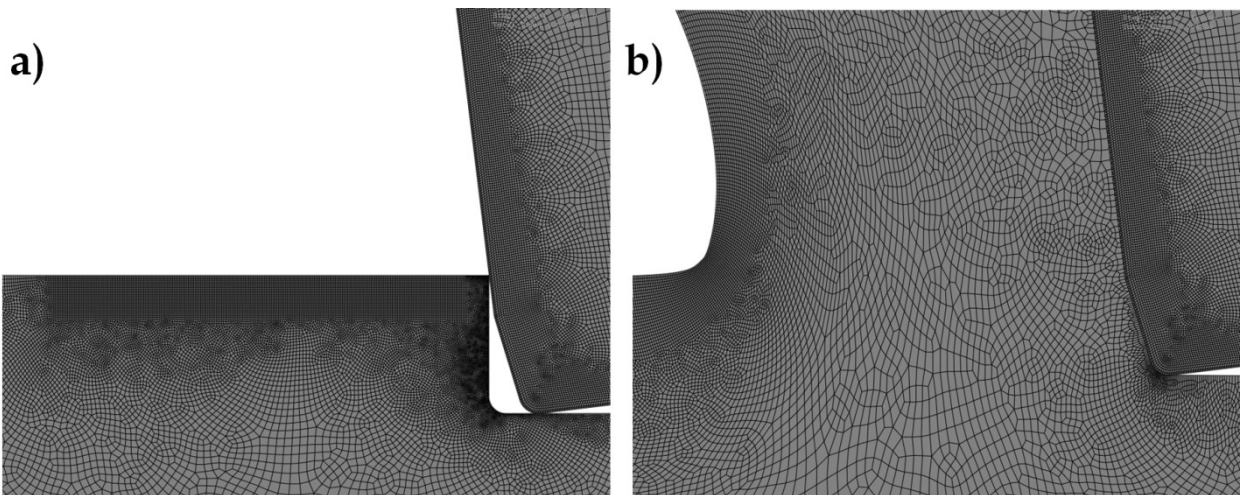
Figure 3: a) Initial mesh at the workpiece and the tool, b) deformed mesh of the workpiece after some cutting time, note the decreasing cutting depth for milling.

The area of the contact between the chip and the tool is called the contact zone and its length the contact length. Through the contact zone a specific part of the heat produced by cutting goes into the tool. The contact zone undergoes the heaviest loading of the whole tool. One important factor is the chip thickness. During a turning process the chip is produced with a constant thickness, while in milling its thickness can

7

decrease towards the end of the chip. The reason for the decrease of the chip thickness is the fact that the cutting depth during milling is decreasing and thus there is less workpiece material flowing into the chip.

Figure 3a presents the meshing of the initial geometry and Figure 3b shows a mesh near the end of the presented calculation. It can be noticed that the initial mesh of the workpiece has changed significantly during the formation of the chip.

1.3 Numerical methods in cutting simulations

Three major methods are used in the simulation of cutting, namely, the Eulerian, Lagrangian and Arbitrary Eulerian-Lagrangian method. There are additional modifications of each method available which are not presented here. The basic problem of cutting simulations is the severe deformation of the workpiece from which the chip is formed. An example of the deformed mesh is shown in Figure 3.

The Eulerian method assumes that the workpiece material flows through a fixed mesh, see Figure 4. This formulation requires the a-priori knowledge of the shape of the chip. Such method can be used for a stationary process which e.g. is the case in turning.

An alternative approach is to use a Lagrangian method in which the mesh is moving together with the material, see Figure 4. The usual problems of this formulation are severe distortions of the mesh. This distortion strongly influences the numerical solution of the problem and usually leads to the termination of the calculation. There are two ways in which this problem can be solved. The first way is to introduce a separation criterion in the mesh. It can be a purely geometrical criterion along a given line between the chip and the workpiece. The separation criterion can also be modeled by a failure law which defines conditions when an element should be deleted. The second way is to use remeshing algorithms. There are two major problems with remeshing algorithms. First, they are extremely expensive in terms of calculation time and resources. Depending on the number of elements which are needed to be remeshed the calculation time can increase drastically. The second problem is that due to remeshing of the workpiece nodes and/or elements in the contact zone have to be disconnected from the contact and after remeshing they have to be put into contact with the tool again. This usually leads to serious errors in the calculation of the contact conditions.

An ALE method combines both Lagrangian and Eulerian formulations and exploits the advantages of both. The finite element mesh in this case is not fixed in space (as in Eulerian formulation) nor is it forced to move with the material (as in Lagrangian formulation). Its equations govern the motion of the mesh in some arbitrarily specified way to allow for a continuous rezoning capability, see Fig. 3. In an ALE formulation, material points are represented by a set of Lagrangian coordinates, a spatial point with a set of Eulerian coordinates and referential mesh points with a set of arbitrary coordinates. This formulation does not require remeshing procedures, because it is avoiding large mesh distortions. Instead of a remeshing procedure, an adaptive mesh procedure is used. A new mesh is created by sweeping iteratively over the adaptive mesh domain and moving nodes to smooth the mesh. A remapping method is used for

transferring the solution variables onto the new mesh. Most importantly it provides the best possible results of the contact zone interactions.
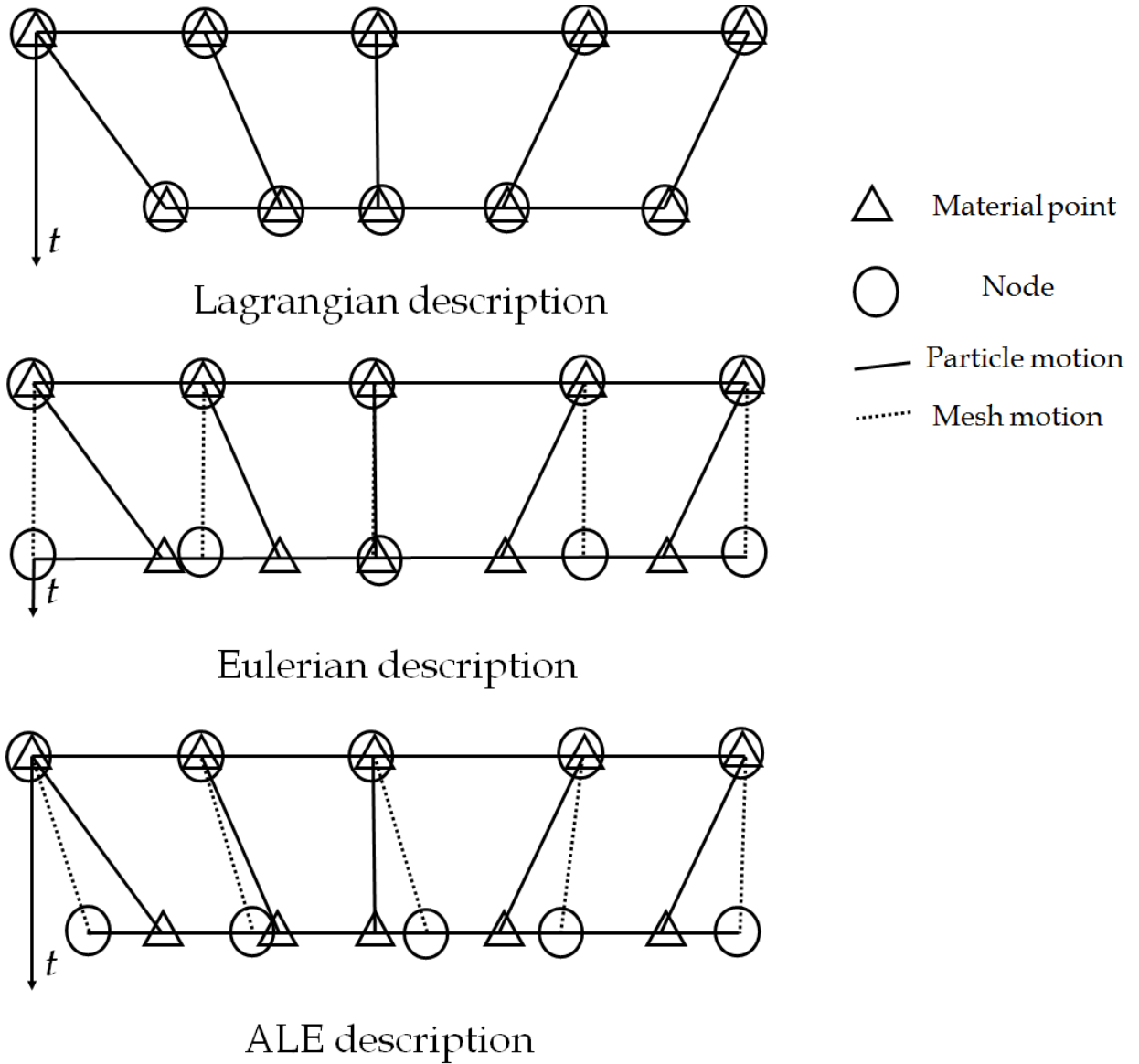
Figure 4: Mesh and particle motion in Lagrangian, Eulerian and ALE 1D models (according to [2]).

1.4 Theoretical formulation of the Arbitrary Lagrangian-Eulerian method

This section is written following Chapter 14 in [2]. To formulate a continuum mechanical set-up two domains are necessary. The first domain is the material domain $R_X \subset \mathbb{R}^n$, where n is the number of spatial dimensions. It consists of material particles of position X. The second domain is the spatial domain R_x with the spatial coordinates x.
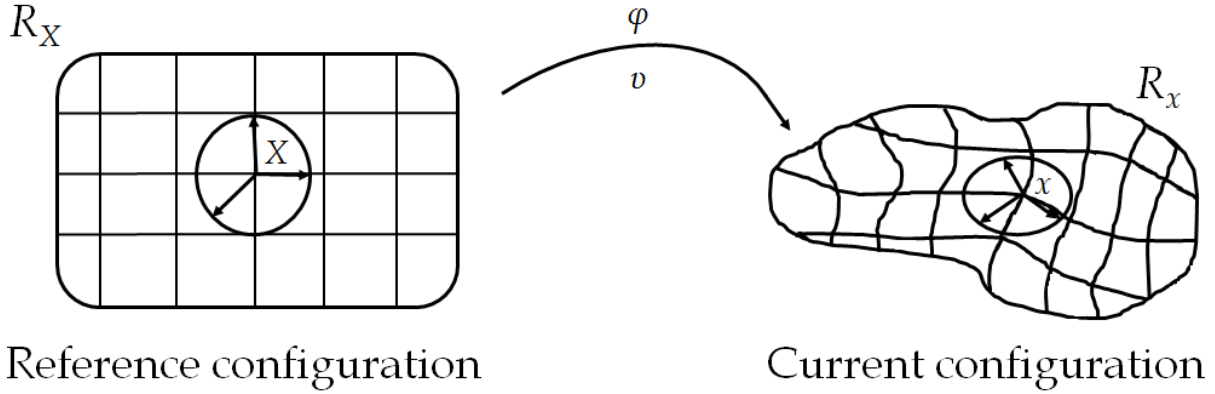
Figure 5: Description of motion in Lagrangian formulation (according to [2]).

As mentioned, in the Lagrangian formulation the material particles move together with the spatial points, see Figure 5. The material points X define the reference configuration R_X. The relation between material and spatial points is defined by application of a function $\boldsymbol{\varphi}$ such that:

$$\boldsymbol{\varphi}: R_X \times [t_0, t_{final}[\rightarrow R_x [t_0, t_{final}[$$
$$(X, t) \mapsto \boldsymbol{\varphi}(X, t) = (x, t) \tag{1}$$

where t_0 represents the starting time and t_{final} represents the time at the end of deformation. The link between X and x can be defined by the law of motion:

$$x = x(X, t) \tag{2}$$

This describes $\boldsymbol{\varphi}$ as the mapping matrix which determines the configuration in the spatial domain for every t. The gradient of $\boldsymbol{\varphi}$ is shown:

$$\frac{\partial \boldsymbol{\varphi}}{\partial (X, t)} = \begin{pmatrix} \dfrac{\partial x}{\partial X} & \boldsymbol{v} \\ \boldsymbol{0}^T & 1 \end{pmatrix} \tag{3}$$

Where $\mathbf{0}^T$ is a null row-vector and the material velocity $\boldsymbol{v}$ is

$$v(X, t) = \frac{\partial x}{\partial t}\Big|_x \tag{4}.$$

The symbol $|_x$ says that $\boldsymbol{X}$ is held constant.

In Eulerian formulation the material particles move and deform through the fixed mesh. The conservation equations are formulated in terms of the spatial coordinates $\boldsymbol{x}$ and the time t. The material velocity $\boldsymbol{v}$ is represented with respect to the fixed mesh and it does not depend on the initial configuration of the continuum and the material coordinates $\boldsymbol{X}$: $\boldsymbol{v} = \boldsymbol{v}(\boldsymbol{x}, t)$.

A generalization of both Lagrangian and Eulerian approaches is synthesized in an ALE formulation. In an ALE formulation a third domain is introduced to serve as referential domain, R_χ with coordinates $\boldsymbol{\chi}$. In Figure 6 these three domains are shown together with mappings between them. The referential domain is mapped into the material and spatial domains by functions $\boldsymbol{\Psi}$ and $\boldsymbol{\Phi}$, respectively. The motion of the particle is defined as $\boldsymbol{\varphi} = \boldsymbol{\Phi} \circ \boldsymbol{\Psi}^{-1}$, where $\circ$ is the composition operator. This shows that all three mappings are mutually dependent, according to Figure 6.

The mapping $\boldsymbol{\Phi}$ should be understood as the motion of the mesh points in the spatial domain. It is represented as:

$$\begin{aligned} \boldsymbol{\Phi}: R_\chi \times [t_0, t_{final}[&\rightarrow R_x [t_0, t_{final}[\\ (\boldsymbol{\chi}, t) &\mapsto \boldsymbol{\Phi}(\boldsymbol{\chi}, t) = (\boldsymbol{x}, t) \end{aligned} \tag{5}.$$

The gradient is

$$\frac{\partial \boldsymbol{\Phi}}{\partial(\boldsymbol{\chi}, t)} = \begin{pmatrix} \dfrac{\partial x}{\partial \chi} & \hat{\boldsymbol{v}} \\ \mathbf{0}^T & 1 \end{pmatrix} \tag{6}.$$

The mesh velocity is

$$\hat{v}(\chi, t) = \frac{\partial x}{\partial t}\Big|_\chi \tag{7}.$$

The mapping $\boldsymbol{\Psi}$ is more conveniently represented by its inverse $\boldsymbol{\Psi}^{-1}$:

$$\begin{aligned} \boldsymbol{\Psi}^{-1}: R_X \times [t_0, t_{final}[&\rightarrow R_\chi [t_0, t_{final}[\\ (\boldsymbol{X}, t) &\mapsto \boldsymbol{\Psi}^{-1}(\boldsymbol{X}, t) = (\boldsymbol{\chi}, t) \end{aligned} \tag{8}.$$

With the gradient and velocity:

$$\frac{\partial \boldsymbol{\Psi}^{-1}}{\partial(\boldsymbol{X}, t)} = \begin{pmatrix} \frac{\partial \boldsymbol{\chi}}{\partial \boldsymbol{X}} & \boldsymbol{w} \\ \boldsymbol{0}^T & 1 \end{pmatrix} \tag{9.}$$

$$\boldsymbol{w}(\boldsymbol{X}, t) = \left. \frac{\partial \boldsymbol{\chi}}{\partial t} \right|_{\boldsymbol{X}} \tag{10.}$$
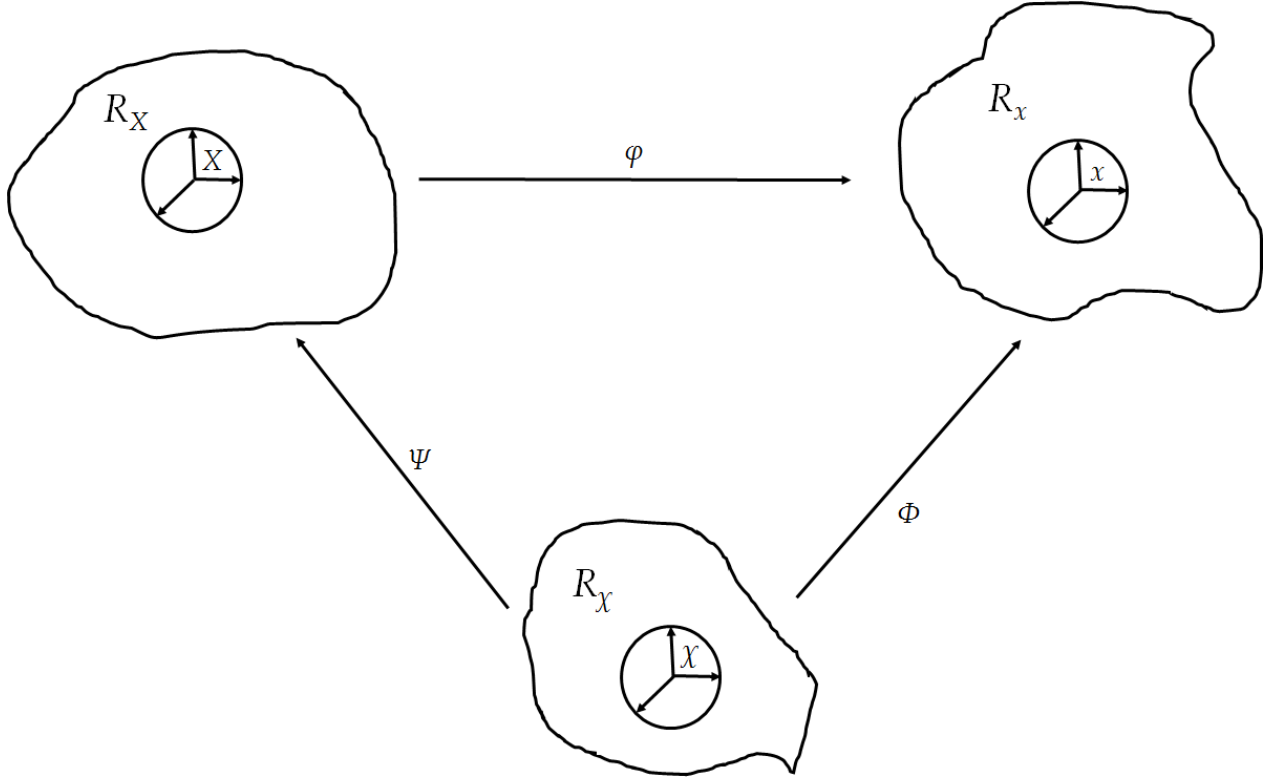
Figure 6: The three domains which are the base of an ALE formulation according to [2]).

The velocity $\boldsymbol{w}$ is the particle velocity in the referential domain. The relation between $\boldsymbol{v}$, $\hat{\boldsymbol{v}}$ and $\boldsymbol{w}$ can be obtained by differentiating $\boldsymbol{\varphi} = \boldsymbol{\Phi} \circ \boldsymbol{\Psi}^{-1}$:

$$\frac{\partial \boldsymbol{\varphi}}{\partial(\boldsymbol{X}, t)}(\boldsymbol{X}, t) = \frac{\partial \boldsymbol{\Phi}}{\partial(\boldsymbol{\chi}, t)}\left(\boldsymbol{\Psi}^{-1}(\boldsymbol{X}, t)\right) \frac{\partial \boldsymbol{\Psi}^{-1}}{\partial(\boldsymbol{X}, t)}(\boldsymbol{X}, t)$$

$$\frac{\partial \boldsymbol{\varphi}}{\partial(\boldsymbol{X}, t)}(\boldsymbol{X}, t) = \frac{\partial \boldsymbol{\Phi}}{\partial(\boldsymbol{\chi}, t)}(\boldsymbol{\chi}, t) \frac{\partial \boldsymbol{\Psi}^{-1}}{\partial(\boldsymbol{X}, t)}(\boldsymbol{X}, t) \tag{11.}$$

In matrix form:

$$\begin{pmatrix} \frac{\partial \boldsymbol{x}}{\partial \boldsymbol{X}} & \boldsymbol{v} \\ \boldsymbol{0}^T & 1 \end{pmatrix} = \begin{pmatrix} \frac{\partial \boldsymbol{x}}{\partial \boldsymbol{\chi}} & \hat{\boldsymbol{v}} \\ \boldsymbol{0}^T & 1 \end{pmatrix}\begin{pmatrix} \frac{\partial \boldsymbol{\chi}}{\partial \boldsymbol{X}} & \boldsymbol{w} \\ \boldsymbol{0}^T & 1 \end{pmatrix} \tag{12.}$$

13

And after matrix multiplication:

$$v = \hat{v} + \frac{\partial x}{\partial \chi} \cdot w \qquad (13).$$

The equation can be rewritten as

$$c = v - \hat{v} = \frac{\partial x}{\partial \chi} \cdot w \qquad (14).$$

Where c is defined as the convective velocity which means the relative velocity between the material and the mesh seen from the spatial domain R_x. If $\partial x / \partial \chi = I$ (where I is the identity tensor), $c = w$, the motion of the mesh is purely translational, without deformations or rotations.

It can be shown that the Lagrangian and Eulerian formulations are boundary cases of the ALE formulation. If $\Psi = I$, equation (3) reduces to $X \equiv \chi$ which leads to a Lagrangian formulation. To obtain an Eulerian formulation $\Phi = I$ and thus from equation (2) $x = \chi$.

For further development of the ALE formulation it is necessary to present conservation laws of mass, momentum and energy. To reach that goal a relation between material time derivative and referential time derivative is needed. The fundamental ALE relation between those two and additionally the spatial gradient is

$$\left.\frac{\partial f}{\partial t}\right|_X = \left.\frac{\partial f}{\partial t}\right|_\chi + \frac{\partial f}{\partial x} \cdot c = \left.\frac{\partial f}{\partial t}\right|_\chi + c \cdot \nabla f \qquad (15),$$

where f is a scalar physical quantity. This relation shows that the time derivative of a physical quantity for a given particle, its material derivative, is its local derivative plus a convective term taking into account the relative velocity c.

The ALE formulation of conservation laws can be obtained from the Eulerian formulation by replacing the material velocity v with the convective velocity c. The result is

Mass:

$$\left.\frac{\partial \rho}{\partial t}\right|_\chi + c \cdot \nabla \rho = -\rho \nabla \cdot v \qquad (16).$$

Momentum:

$$\rho \left(\left.\frac{\partial v}{\partial t}\right|_\chi + (c \cdot \nabla)v \right) = \nabla \cdot \sigma + \rho b \qquad (17).$$

14

Total energy:

$$\rho \left(\frac{\partial \boldsymbol{E}}{\partial t} \bigg|_{\chi} + \boldsymbol{c} \cdot \nabla \boldsymbol{E} \right) = \nabla \cdot (\boldsymbol{\sigma} \cdot \boldsymbol{v}) + \boldsymbol{v} \cdot \rho \boldsymbol{b} \tag{18}.$$

Internal energy:

$$\rho \left(\frac{\partial \boldsymbol{e}}{\partial t} \bigg|_{\chi} + \boldsymbol{c} \cdot \nabla \boldsymbol{e} \right) = \boldsymbol{\sigma} : \nabla^{S} \boldsymbol{v} \tag{19}.$$

In these equations ρ is the mass density, $\boldsymbol{v}$ is the material velocity vector, $\boldsymbol{\sigma}$ is the Cauchy stress tensor, $\boldsymbol{b}$ is the specific body force vector, $\boldsymbol{E}$ is the specific total energy and $\boldsymbol{e}$ is the specific internal energy. The term $\nabla^{S} \boldsymbol{v}$ denotes the stretch (or its rate) tensor. The presented ALE forms of conservation laws are used as basis for the spatial discretization of problems in both fluid dynamics and solid mechanics.

To obtain a successful computer implementation of the ALE formulation a mesh-update procedure is needed. The mesh-update procedure assigns velocities or displacements to each node during a calculation. There are two major mesh-update strategies:

i. The concept of mesh regularization which is of geometrical nature. The idea of this strategy is to keep the mesh as regular as possible and to avoid mesh entanglement during calculation.

ii. Mesh-adaptation techniques: here the finer mesh should be concentrated in the zone of interest. In this work a mesh adaptation strategy is used which will subsequently be presented.

2 2D cutting modeling

2.1 2D finite element model of the milling process

A photography of the real milling process is presented in Figure 7a. The scheme of the process is presented in Figure 7b. The whole milling process consists of the miller tool holder's rotation and translation. The milling tool holder is equipped with one milling insert which removes material at 560 rotations/min. In one rotation the duration of the material removal is 14 ms. During the rest of the rotation (92 ms), the tool cools down. In this work 8.5 ms of the milling time per rotation has been modeled using a 2D FE ALE model. Such a time span is sufficient to see the influence of hard coatings on the loading of the substrate. The full process which includes 14 ms of tool loading and 92 ms of idle time in several cycles, is studied in the 3D tool milling process model. This model is presented in Chapter 3.
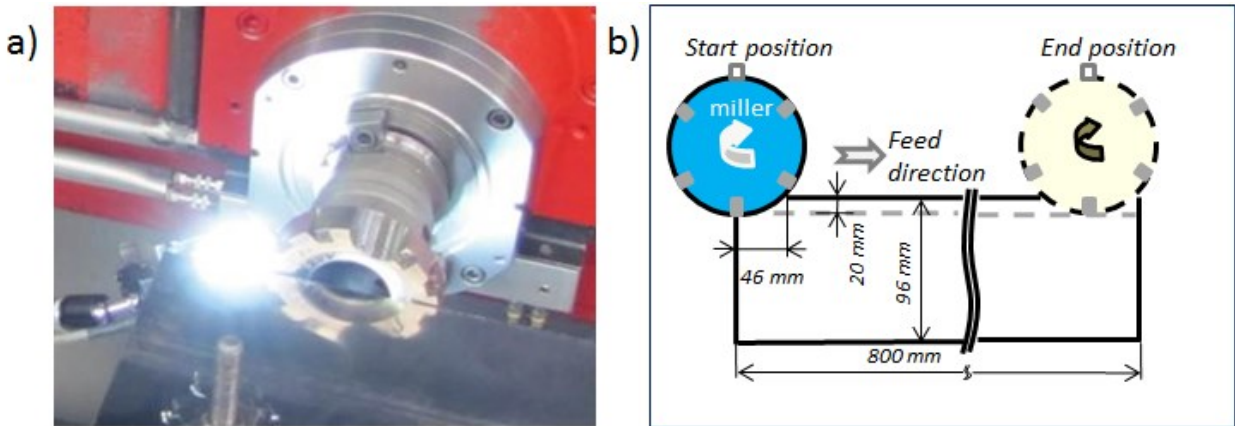
Figure 7: a) industrial milling process, b) scheme of the milling process (according to [3]).

In Figure 8 the temperature development at the rake face of the tool is presented. It demonstrates the cyclic loading and unloading process of the tool during milling. The process consists of several cycles. In this case 10 cycles are simulated. The end time of the loading part of the cycle is marked with a green line. The idle part of the cycle starts with the green and ends with the red line. During the idle part the stresses induced during the loading are relaxed. The heat is conducted from the surface towards the interior of the tool. Hence, the temperature at the surface decreases. The temperature rises from cycle to cycle thereby increasing the average temperature of the tool.
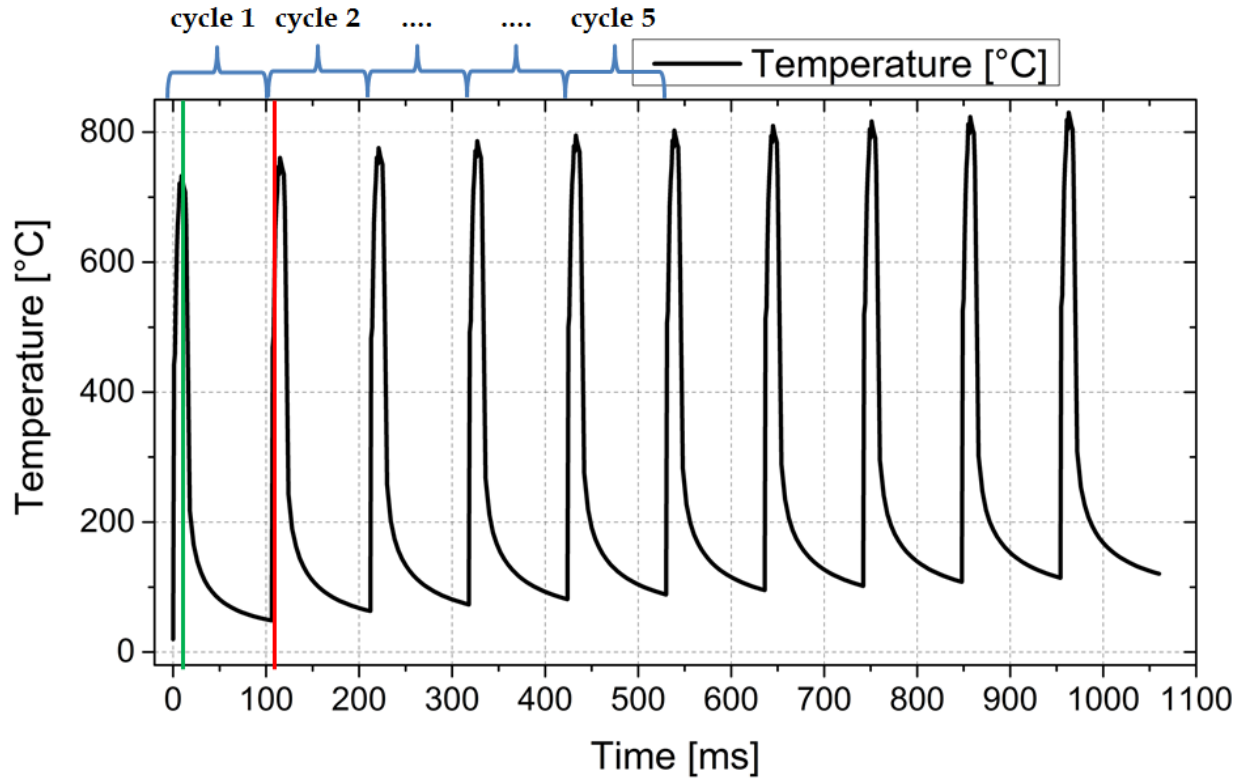
Figure 8: The evolution of the temperature at the surface of the tool. Blue brackets at the top mark the loading and unloading cycles. The green line indicates the end of the loading in the first cycle. The period between the green and red line is the idle cycle part.

In models using an ALE formulation the inflow and outflow surfaces are defined on the workpiece, see Figure 9. They serve to model the flow of the material through the mesh of the workpiece. They are usually constrained in vertical and horizontal directions to ensure that the same amount of material moves in and out from the model. This approach is used to model cutting processes with constant cutting depth, like orthogonal cutting or turning. In milling in contrast to turning, the cutting depth is not constant. It can either increase or decrease depending on the milling setup. In our modeled process, the cutting depth decreases with time which means that in the 2D model the tool has to move upwards. This makes it necessary to remove the constraints in vertical direction at the outflow surface while the inflow surface remains constrained, thus allowing the outflow surface to spread in vertical direction and additional material can flow out so mass conservation is guaranteed. In the present model it is easy and convenient to change these boundary conditions and thus the same model can serve as a toolbox for simulating processes with constant or changing cutting depth.

In Figure 9, a scheme of the FE ALE model is presented. The arrows indicate the inflow and outflow surfaces of the ALE model. A cutting speed of 220 m/min is

assumed. If a different speed is used in this particular model, it will specially be indicated. The speed of the tool in upward direction is calculated in the FE model in such a way that the decrease of the cutting depth in the real milling process is simulated. The milling process starts at a cutting depth of 0.4 mm and reaches almost zero depth at the end of the cut. Therefore, the tool moves with 26 mm/s upwards in the simulations. A cutting depth of 0.4 mm is a standard value, other cutting depths are also specially indicated.

The model creation as well as the post processing is done using *Abaqus/CAE 6.13-3* [4]. The calculations are conducted using *Abaqus/Explicit 6.13-3* [4].
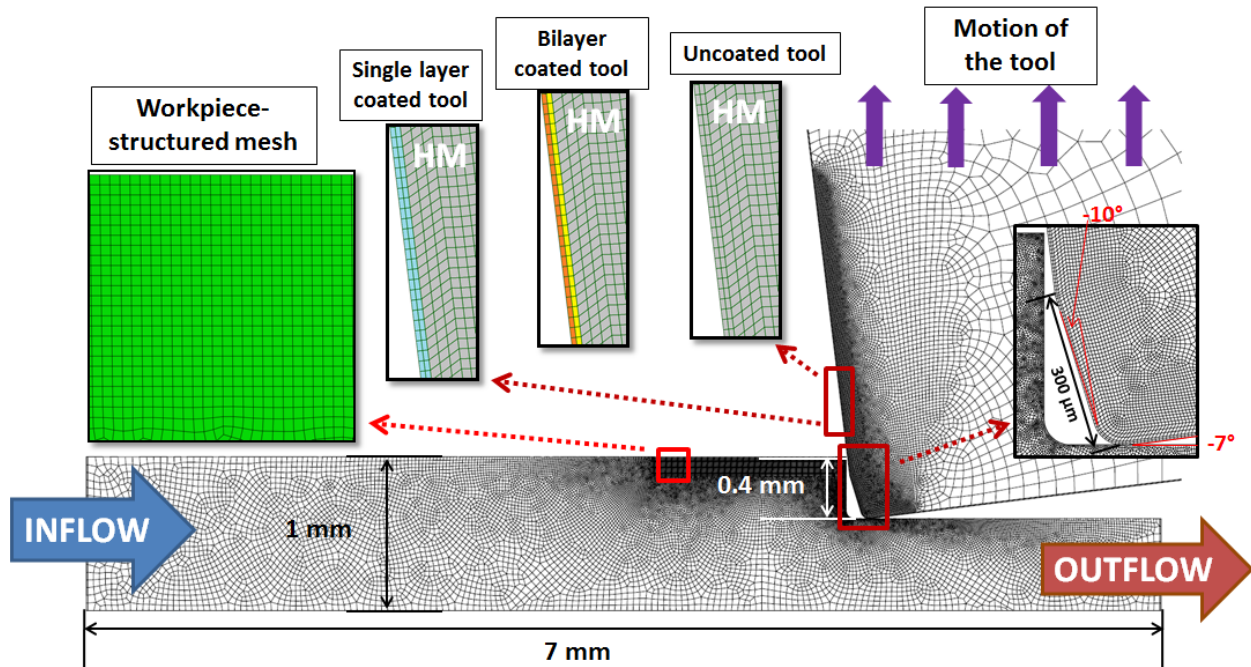
Figure 9: FE ALE model of the milling process. The purple arrows at the top of the tool indicate an upward motion of the tool. The starting cutting depth is 0.4 mm. The structured mesh at the top part of the workpiece is also shown. Single layer, bilayer coated and uncoated tools are shown in the middle of the figure.

The model consists of two parts: workpiece and tool. The workpiece has dimensions of 1×7 mm², while the dimensions of the tool are 7×7 mm². The geometry of the cutting edge of the milling tool is represented in Figure 9 by a 2D cross section of the real milling tool perpendicular to the rake surface of the tool. All angles and edge radii of the real tool are included in the modeled cutting plane. The cutting edge is chamfered, where the chamfered angle is -10° to the rake face and the chamfer exhibits a length of 300 µm. The cutting edge itself is rounded with a radius of 56.5 µm. The cutting angle is -7°. The tool is modeled as one part containing three sections. The first two sections are two thin element rows on the tool surface. Each element row has a

18

thickness of 3.5 µm, starting from the top of the rake face to the end of the flank face. By changing the material definition, these two element rows can serve as different coatings or as substrate, see Figure 9. The third section is the rest of the tool which corresponds to the hard metal (HM) substrate. The entire tool consists of 12018 elements.

Both parts are modeled using a combination of structured and free mesh available in *Abaqus/CAE 6.13-3* to minimize the number of unnecessary elements and to increase the number of elements where they are needed such as in the contact zone. The element type used in both parts is CPE4RT. This is 2D coupled temperature-displacement plane strain element type with reduced integration and hourglass control.

A structured mesh is used at the upper side of the workpiece to enhance and stabilize the formation of the chip, see Figure 9. The workpiece consists of 26697 elements, and for the workpiece material data for a 42CrMo4 steel are used. The number of elements is lower for the models with smaller cutting depth.
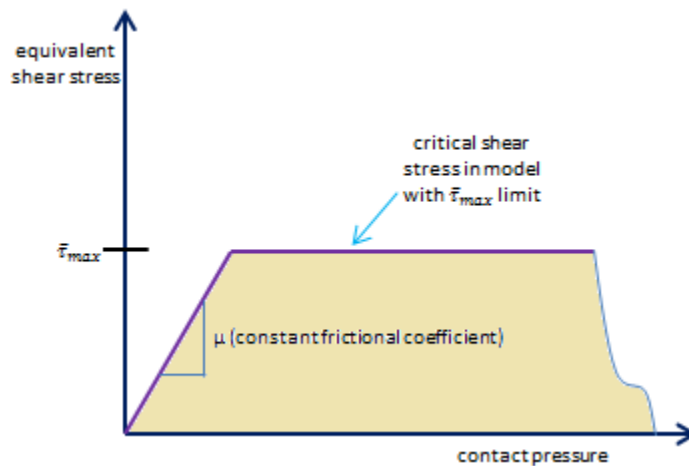
Figure 10: The shear stress limit friction model.

Friction is defined by the interaction of the workpiece and the tool. The Coulomb friction model is used coupled with an artificial shear stress limit $\bar{\tau}_{max}$, see Figure 10. This limit is introduced since the shear stress at the interface, calculated by the Coulomb theory, may exceed the yield stress of the contacting materials. The upper boundary for $\bar{\tau}_{max}$ follows as $\sigma_Y/\sqrt{3}$, where σ_Y is the Mises yield stress of the workpiece material. In this thesis two workpiece material models are used and depending on the model a different constant value of $\bar{\tau}_{max}$ is calculated from the workpiece yield strength. For milling and turning models it amounts to 346 MPa while for orthogonal cutting models it amounts to 290 MPa. The assumed standard friction coefficient value used in most of all calculations is 0.4. It will specially be indicated if a different friction coefficient is used.

Due to the plastic deformation of the workpiece material, energy is dissipated from which 90% is assumed to be converted to heat. Additional heat is produced by friction between the chip and the tool. All the heat produced is equally partitioned to flow into the tool and the chip.

The heat transfer coefficient h_1 allows a thermal exchange between the chip and the tool. For the cutting speed used in these models, a value of 100 kWm^{-2}K^{-1} is used [5]. The model includes the convection of heat from the tool surface and from the workpiece material into air. The convective heat transfer coefficient is calculated using Nusselt´s empirical formulas, applying the procedure of Kagnaya et al. [6]. The value of h_2 derived from this procedure is 100 Wm^{-2}K^{-1}.

2.2 Determination of the material data

This section provides an explanation and description of how material data for the workpiece material, HM and hard coatings were derived.

2.2.1 Workpiece material

The selection of the proper mathematical description of the workpiece material is of greatest importance for the tool loading. It determines the shape, the length and the type of the chip. The formation of the chip in combination with the mesh distortion due to deformation determines the available simulation time of the cutting process.

The chips produced in orthogonal cutting and milling experiments are usually or at least very often serrated. There are different approaches for modeling this kind of chips but they need complex assumptions and sometimes even artificial assumptions are added. Furthermore numerically expensive material laws [7], [8] are needed. The results in [8] show that modeling of serrated chips is much too time consuming for performing a tool load analysis. Also, it turns out that simulations began to diverge after a couple of milliseconds which is not sufficient to obtain tool loading conditions similar to the experimental ones which would require the simulations of 14 ms. The Johnson-Cook (JC) law produces a continuous and stable chip. It was selected following the assumption that regarding the tool loading a more correct process time has more influence on the tool loading as the localization process in the chip. In a subsequent chapter it is shown that the chosen material description can produce the response of the workpiece similar to an experiment. The JC law reads

$$\sigma_{eq} = (A + B\varepsilon^n)\left(1 + C ln\frac{\dot{\varepsilon}}{\dot{\varepsilon}_0}\right)\left(1 - \left(\frac{T - T_{room}}{T_m - T_{room}}\right)^m\right), \tag{20}$$

where ε is the plastic strain, $\dot{\varepsilon}$ is the strain rate (s^{-1}), $\dot{\varepsilon}_0$ is the reference plastic strain rate (0.001 s^{-1}), T and T_m correspond to the temperature of the workpiece material ($°C$) and the melting temperature of the workpiece material (1520 $°C$), respectively. T_{room} is the room temperature (RT) (20 $°C$). The coefficient A represents the yield stress (MPa), B the hardening modulus (MPa), C the strain rate coefficient, n is the hardening coefficient and m the thermal softening coefficient. The Johnson-Cook (JC) parameters are taken from [7] for the orthogonal cutting models and from [9] for the turning and milling models. They are presented together with the thermo-physical data in Table I.

Table I.

Thermo-physical properties and Johnson-Cook parameters of the 42CrMo4 steel.

Thermo-physical properties	Value	Johnson-Cook parameters	Value [7]	Value [9]
Density (ρ) [kgm^{-3}]	7800	A [MPa]	504	600
Young's modulus (E) [GPa]	210	B [MPa]	370	643
Poisson's ratio (ν) [-]	0.3	n [-]	0.17	0.41
conductivity (λ) [Wm^{-1}K^{-1}]	46	m [-]	0.793	0.957
thermal expansion (a) [K^{-1}]	$1.2 \cdot 10^{-5}$	C [-]	0.025	0.0037
specific heat (c) [Jkg^{-1}K^{-1}]	476			
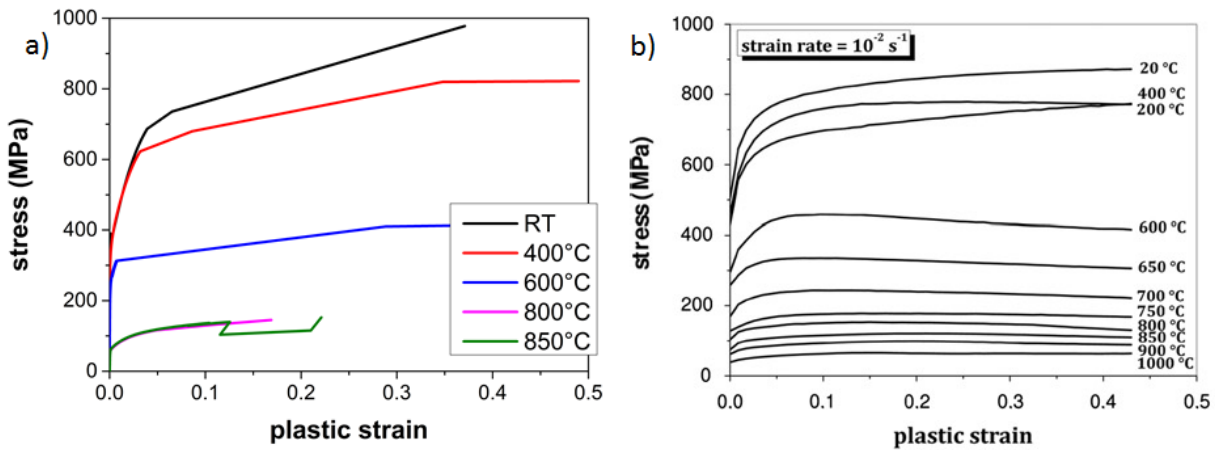
Figure 11: flow curves of the 42CrMo4 steel: a) the uniaxial compressive stress test at Materials Center Leoben Forschung GmbH, b) results presented in [10]. The green line value exhibits measuring artefact after 0.12 of the plastic strain.

Different JC parameters are used for several reasons. First of all, during the process of data collection it was discovered that there are several different sets of JC parameters claiming to represent 42CrMo4, see e.g. [11], [12], [13]. Those sets, of course, produce different results. The question arises, which parameters describe the workpiece material used in the milling experiment. Based on uniaxial compressive stress tests carried out at MCL – the results are presented in Figure 11a- a literature research showed that they coincide best with results presented in [10]. In a subsequent paper [7] JC parameters were presented which describe the measured results of the flow curves. These parameters are used for the validation of the model in comparison to the orthogonal cutting tests. Although they produce acceptable results, the chip produced in the milling simulations is still unstable. The JC parameters presented in [9] produce slightly thicker

and thus more stable chips which allow simulations of more than 8 ms of milling and more than 10 ms of turning. For these reasons this set of parameters has been selected.

2.2.2 Hard metal and hard coatings

The newly measured material properties at hand are measured in the first and second part of the project. The material properties of hard metals and hard coatings are a product of work done by Tamara Teppernegg and Dr. Michael Tkadletz, respectively.

The tool consists of the HM substrate and hard coatings. Their thermo-physical and mechanical material properties have to be accurately determined in order to produce reliable FE simulation results for both. In this section an overview of the necessary experimental characterization techniques is presented together with results.

The substrate of the standard tool is modeled with thermo-physical properties of a HM with 8 wt. % Co and its thermo-physical properties are presented here. Subsection 2.4.4 deals with the influence of the different substrates on the tool loading. Their material properties are listed in the appendix.

The density of the HM grade was determined by weighing a block specimen ($10 \times 10 \times 3.5$ mm^3) in air and in water according to ISO 3369 [14], yielding a value of 14890 kgm^{-3}. The thermal conductivity λ and the thermal diffusivity a were measured ranging from room temperature (RT) to 1000 °C using laser flash equipment (Netzsch LFA 457 MicroFlash). The thermal conductivity values presented in Figure 12a were determined using the introduced energy of the laser pulse, the specimen geometry and the difference in temperature before and after the pulse. The heat capacity c_p was calculated according to [15] using the density ρ, thermal diffusivity a and conductivity λ.

The Young's modulus E and shear modulus G were obtained using a resonant beam technique. The rectangular bar ($45 \times 4 \times 3$ mm^3) was excited to oscillate and the eigen-frequency of the HM was detected. Then E and G were determined according to the method described in [16]. The Poisson's ratio ν was calculated according to [17]. The results for Young's modulus and Poisson's ratio are shown in Figure 12b for temperatures up to 1100 °C.

To determine the compressive flow strength, static uniaxial tests under compression loading conditions were performed using a servo-hydraulic testing machine (Instron 8803). The experiments were carried out under ambient atmosphere from RT to 900 °C. Strain measurements were done contactless via a laser extensometer P- 2S-50/400 Hz (Fiedler Optoelectronic GmbH). Two HM grades with 6 wt. % and 10.5

wt. % Co content were tested. It is expected that the flow strength of the WC with 8 wt. % Co content is approximately a mean value of the two tested grades. The results are presented in Figure 12c.

The thermal expansion coefficient a_{th} was measured using a dilatometer (Netzsch DIL 402 E/7). Cylindrical samples with a diameter of 5 mm and a starting length L_0 of 25 mm were used. The increase of the specimen length with increasing temperature and the length change ΔL were measured and the thermal expansion coefficient a_{th} was calculated according to [18] for temperatures up to 1300 °C (see Figure 12d).
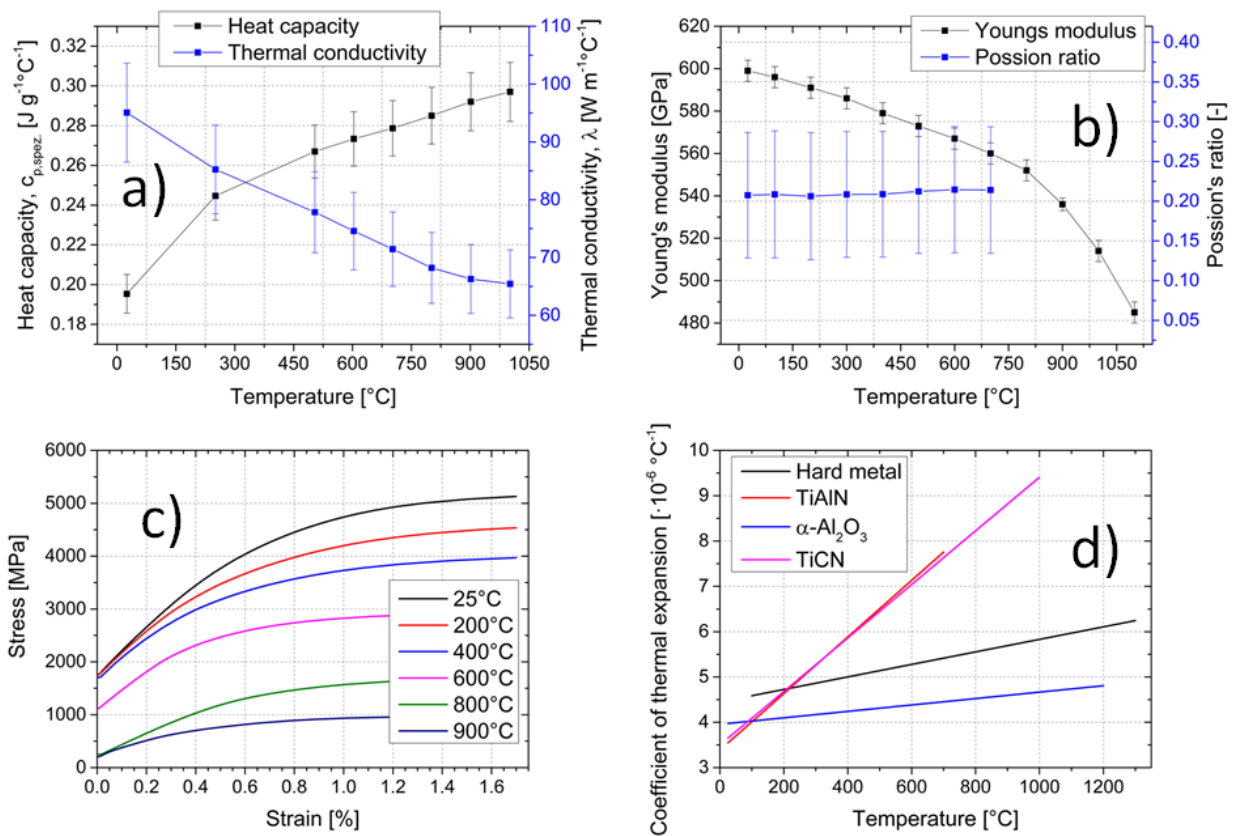
Figure 12: Collection of material data for hard metal and coating samples: a) measured heat capacity and thermal conductivity of HM with 8 wt.% Co, b) measured Young's modulus and Poisson's ratio of HM with 8 wt.% Co, c) estimated flow strength of HM with 8 wt.% Co, d) measured thermal expansion coefficient of HM with 8 wt.% Co and coatings. The reference temperature for the thermal expansion coefficient is 20°C.

In order to determine the mechanical properties of the hard coatings, nanoindentation experiments were performed. The tests were conducted using an UMIS nanoindenter provided by Fischer- Cripps Laboratories equipped with a Berkovich diamond indenter. To minimize influence on the results from the substrate, the

maximum loads were chosen to reach maximum indentation depths of less than 10 % of the coatings thickness [19]. For each coating, at least ten measurements were used to evaluate hardness and Young's modulus according to Oliver and Pharr [20]. The Poisson's ratios for the TiAlN, α-Al$_2$O$_3$ and TiCN coatings were taken from Refs. [21], [22], [23] (see Table II).

Table II.
Measured and literature values for the thermo-physical properties of the hard coatings.

Parameter	TiAlN	α-Al$_2$O$_3$	TiCN
Density (ρ) [kgm^{-3}]	5400	3980	5320
Young's modulus (E) [GPa]	557	340	567
Poisson's ratio (ν) [-]	0.25 [21]	0.231 [22]	0.182 [23]
thermal conductivity (λ) [Wm^{-1}K^{-1}]	5.6	7.5 [24]	30 [24]

The thermal expansion coefficients of the TiAlN, TiCN and α-Al$_2$O$_3$ coatings were investigated using high temperature X-ray powder diffraction (HT-XRD) utilizing a Bruker D8 Advance diffractometer, equipped with an Anton Paar HTK 2000 hot stage, operated under vacuum (base pressure <10^{-4} mbar). For α-Al$_2$O$_3$ a directionally averaged value for the thermal expansion coefficient was calculated from the values determined for the a and c axes according to [22]. In Figure 12d the thermal expansion coefficients for all three coatings derived from the HT-XRD are presented. Time-domain thermoreflectance [23], [25] was applied to determine the thermal conductivity of the TiAlN coating, while for the α-Al$_2$O$_3$ and TiCN literature values were used [24]. The heat capacity of TiAlN was taken from Figure 5 in [26], α-Al$_2$O$_3$ from Table 2 in [27] and TiCN from Figure 4 in [28].

X-ray reflectivity measurements utilizing a Rigaku SmartLab diffractometer were performed to estimate the densities of the coatings from the critical angle of the recorded reflectivity curves, using the software package Leptos provided by Bruker for data post-processing [29]. A summary of the used thermo-physical properties of the hard coatings is shown in Table II.

The tool is either coated with a 7 µm thick arc evaporated TiAlN layer or with two chemically vapor deposited (CVD) layers of TiCN and α-Al$_2$O$_3$, each having a thickness of 3.5 µm. Both types of layers are included in the models. A third coating combination consisting of two 3.5 µm thick layers of TiAlN and α-Al$_2$O$_3$ is investigated for comparison. Additionally, an uncoated HM tool is studied. The substrate of the tool is modeled with the thermo-physical properties of a HM with 8 wt. % Co.

2.3 Validation of the FE ALE model

This chapter is concerned with the validation of the finite element (FE) Arbitrary Lagrangina Eulerian (ALE) cutting model. The validation is done by comparing the numerical results with experimental results of two cutting set-ups.

The first experimental set up was an orthogonal cutting carried out at the Laboratory for Machine Tools and Production Engineering (WZL) of RWTH Aachen University. Three cutting depths were chosen. For each cutting depth two cutting speeds were compared. The standard FE ALE model with constant cutting depth presented in section 2.1 is used to model the orthogonal cutting process. Some model changes were necessary to represent the cuts at different depths and speeds.

The second experimental set up was a milling process performed at CERATIZIT Austria. A FE ALE milling model is used for this comparison. The characteristic thinning of the chip was simulated by moving the tool upwards and thus decreasing the cutting depth.

2.3.1 Comparison to the orthogonal cutting experiments
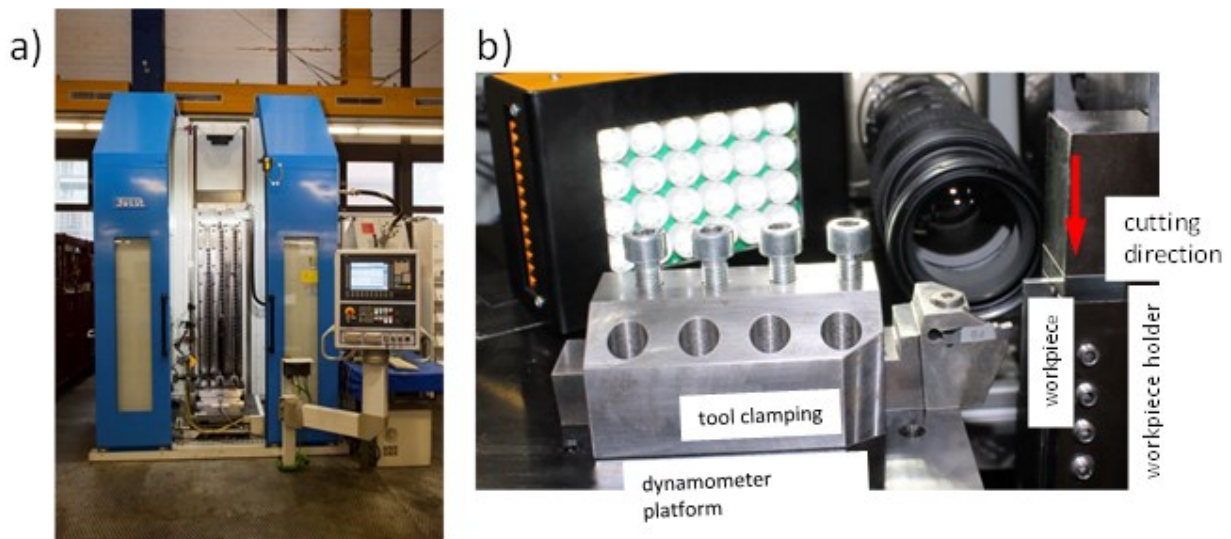
Figure 13: a) Cutting machine Forst RASX 8x2200x600 M/CNC, b) cutting set up, camera and the lights are positioned in the back.

Orthogonal cutting experiments were performed at WZL RWTH Aachen with the help of Dipl.-Ing. Hendrik Puls. The cutting machine used for the experiments was a Forst RASX 8×2200×600 M/CNC, see Figure 13a. The machine is capable of synchronised measurements of the cutting force components, two-colour pyrometer temperature measurements and high-speed video analysis. A closer look at the camera

and cutting set up is presented in Figure 13b. The cutting tool is fixed at the dynamometer platform with the tool holder. The workpiece material is fixed on a large material holder which moves in downward direction. To obtain good photos with the high speed camera the workpiece material has to be softly ground on the sides and must be lit with strong lights.
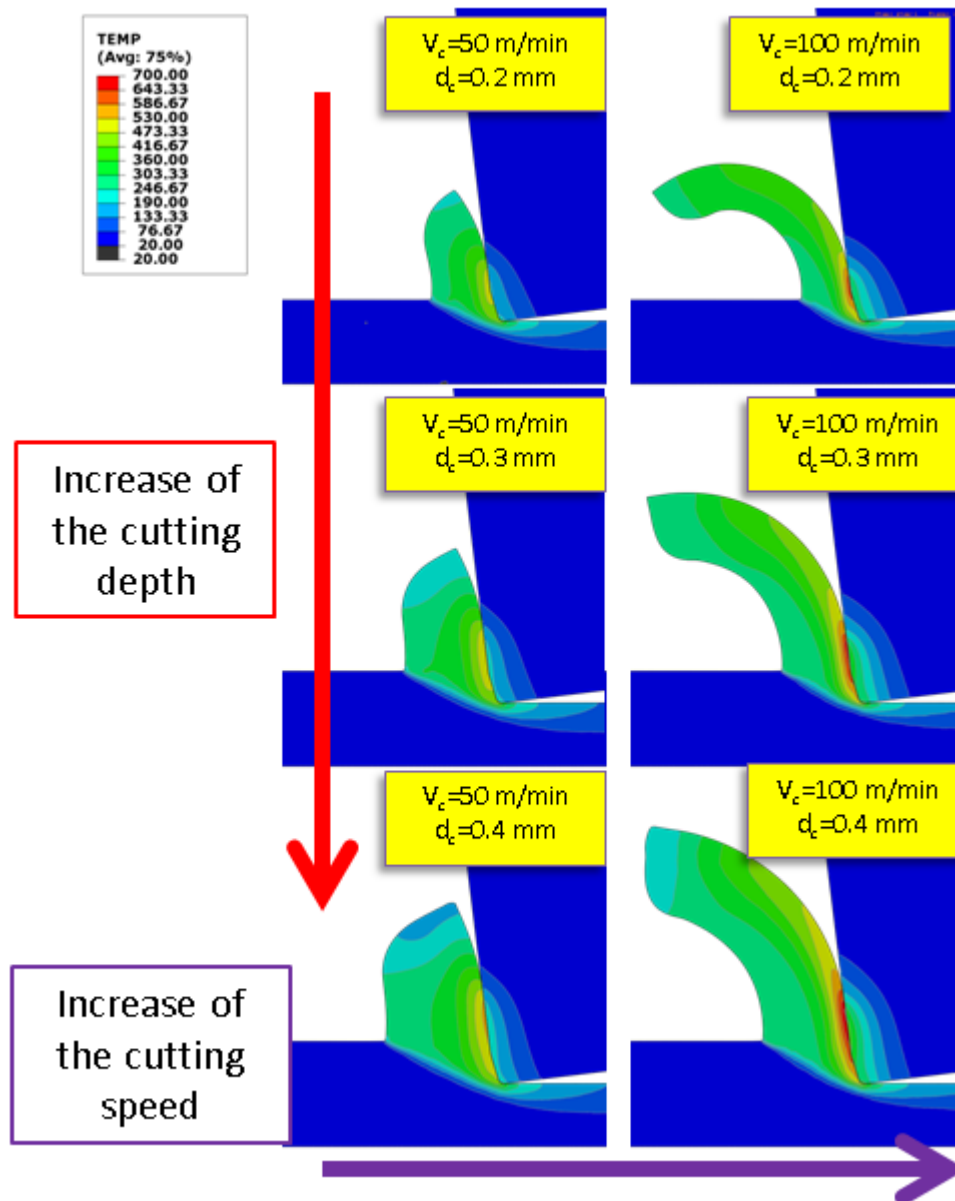
Figure 14: Results of the orthogonal cutting simulations for different cutting depths and speeds.

The cutting experiments were performed at cutting depths of 0.2, 0.3 and 0.4 mm. At each cutting depth, cuts were performed at speeds of 50 m/min and 100 m/min. Higher

speeds produce large vibrations and thus they are not suitable for the experiments. The following measurements were carried out: the cutting force vs. time, temperature measurements using pyrometric fibers. The whole process was filmed by a high-speed camera. The recorded videos were used to measure contact lengths and chip thicknesses.

A series of six FE ALE models was created to represent the experimental set-up, see Figure 14. The results are compared after 3 ms of the chip. The results show that the increase of the cutting depth leads to higher chip thickness, higher cutting temperatures and higher material removal rate. The increase of the cutting speed leads to lower chip thickness, to higher cutting temperatures and higher material removal rate.
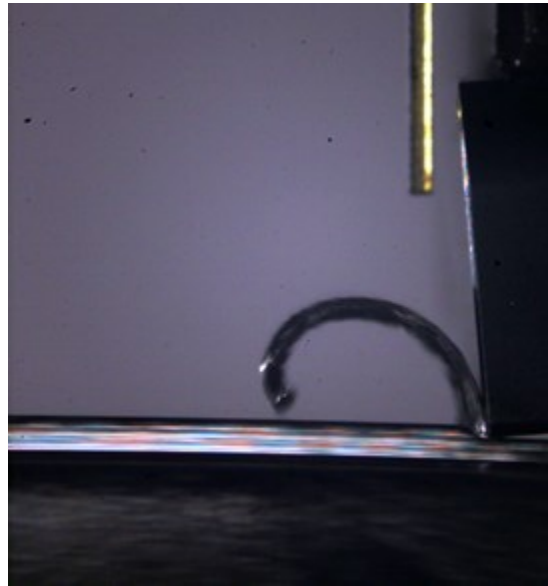
Figure 15: Measurements of the chip temperatures using two-color pyrometer.

The temperatures of the chips are measured using a pyrometer positioned above it, see Figure 15. An average measured temperature is taken as reference. In Table III, a comparison of the experimentally measured and simulated temperatures is shown. The trends in chip temperature are the same between measurement and simulations. The values differ slightly (from 9 to 15 %).

Experimentally measured and simulated average chip thicknesses and contact lengths in dependence on cutting speed and depth are compared in Table IV. Selected simulation results are presented in Figure 16. The deviations in contact length are from 2 to 18 %. The chip thickness is not really comparable because in the model only a flow chip can be created while in reality chips are serrated. Nevertheless, the same trend is

obtained both for measured and simulated chip thicknesses. The validation of the results by comparing the chip formation seems therefore satisfactory.

Table III.
Comparison between experimentally measured and simulated maximum temperatures on the chip surface at different cutting speeds and depths.

50 m/min	0.2 mm			0.3 mm			0.4 mm		
	exp.	sim.	ratio	exp.	sim.	ratio	exp.	sim.	ratio
Temperature [°C]	425	370	1.15	450	400	1.13	470	420	1.12
100 m/min	0.2 mm			0.3 mm			0.4 mm		
	exp.	sim.	ratio	exp.	sim.	ratio	exp.	sim.	ratio
Temperature [°C]	460	400	1.15	480	440	1.09	515	470	1.10
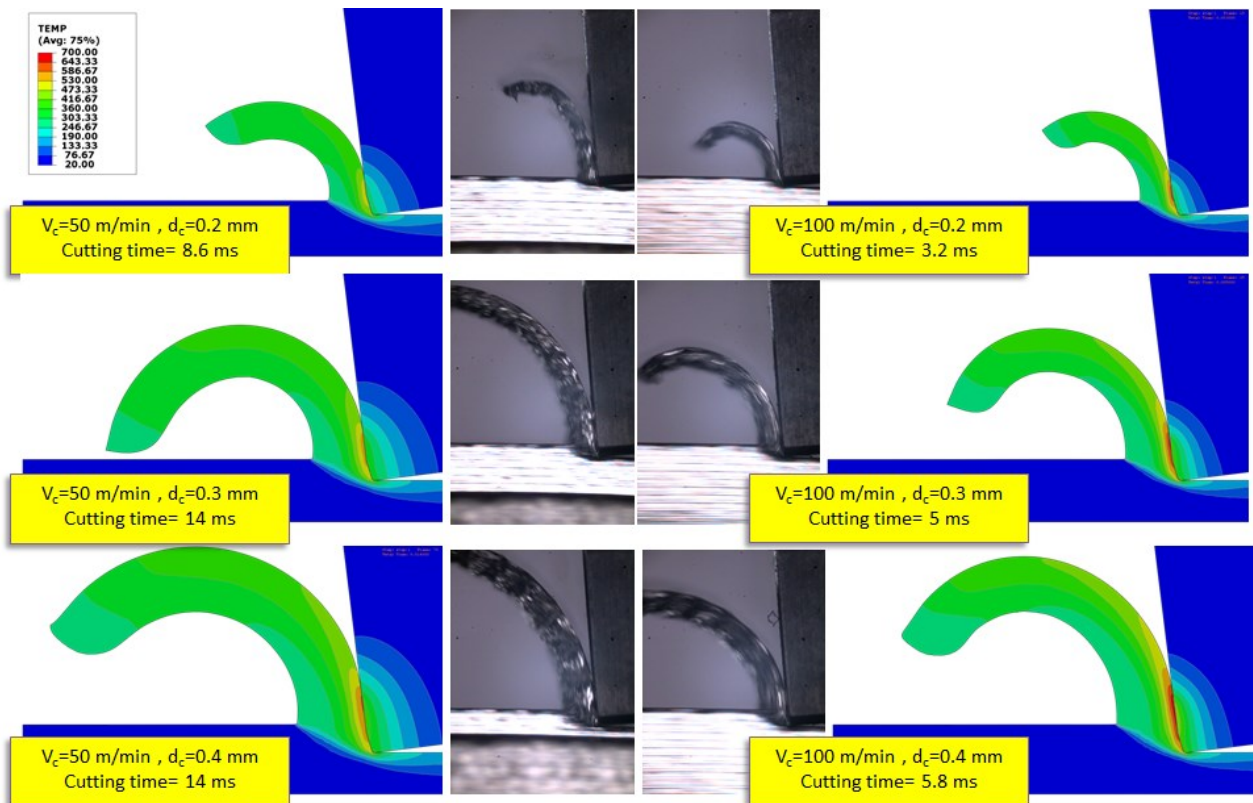
Figure 16: Comparison of the chip shapes between simulations and experiments.

Table IV.

Comparison of the measured and simulated average chip thicknesses and contact lengths.

50 m/min	0.2 mm			0.3 mm			0.4 mm		
	exp.	sim.	ratio	exp.	sim.	ratio	exp.	sim.	ratio
average chip thickness [µm]	294±20	540±12	0.54	521±14	754±14	0.69	600±20	948±29	0.63
contact length [µm]	627	550	1.14	893	760	1.18	922	940	0.98
100 m/min	0.2 mm			0.3 mm			0.4 mm		
	exp.	sim.	ratio	exp.	sim.	ratio	exp.	sim.	ratio
average chip thickness [µm]	290±18	461±23	0.63	428±19	645±21	0.66	534±17	826±30	0.64
contact length [µm]	467	490	0.96	708	680	1.04	752	860	0.87

Table V shows a comparison of the measured and simulated cutting forces depending on cutting speed and depth. A similar trend can be observed for both measured and simulated cutting forces. They increase with cutting depth. The difference between experiments and simulations range from 8 to 18%.

Simulations and experiments show that an increasing cutting depth increases the chip thickness, temperatures and material removal rate. Also, an increasing cutting speed decreases the chip thickness, increases temperatures and increases the material removal rate. Since the chip serration is not simulated, the modeled chips are thicker than experimental ones (31 to 46 %). The simulated contact lengths are a little shorter than measured ones (2% to 18%). For the same cutting depth, the contact length is higher for lower speed. The simulated cutting forces are lower than experimentally measured forces (8% to 18%). The simulations show that for the same cutting depth, a lower speed produces a higher force, the chip is thicker, temperatures are lower and thus the yield stress is higher. An increase of the cutting depth results in higher cutting forces. For contact length and cutting force, which are together with the temperature the most important parameters determining the tool loading, the deviations between experiments and simulations are about 10-15%. As conclusion, although the simulation

results in certain situations slightly differ from the experimental evidence, they show the same trends as the experiments so they can be used to quantify the tool loading.

Table V.

Comparison of the measured and simulated cutting forces.

50 m/min	0.2 mm	0.3 mm	0.4 mm
F_{exp} [N]	500	675	875
F_{sim} [N]	450	625	795
ratio	1.11	1.08	1.10
100 m/min	0.2 mm	0.3 mm	0.4 mm
F_{exp} [N]	500	675	850
F_{sim} [N]	425	590	750
ratio	1.18	1.14	1.13

2.3.2 Comparison to the milling experiments

For the evaluation of the milling process including the complete heating and cooling cycle, a the simulation must be sustained for as long as possible without running into convergence issues. To increase the numerical stability of the simulated chip formation and thus increase the simulated cutting time the workpiece material 42CrMo4-FP steel behavior is modelled using a JC law with parameters suggested by Pujana et al. [9]. These parameters lead to thicker and shorter chips than those observed in milling experiments. Also, the contact length is longer and the temperature at the tool surface is higher than the one obtained from the milling experiments.

In Figure 17a and b, the comparison of the simulated contact length and the experimentally obtained contact length on the rake face of the tool is presented. The experimental measurements were done by Tamara Teppernegg. The simulated contact length changes over time, and for the first 10 ms of the cut it is longer than the experimentally obtained contact length. This contact length influences the spreading of the heated zone on the tool surface (see Figure 18).
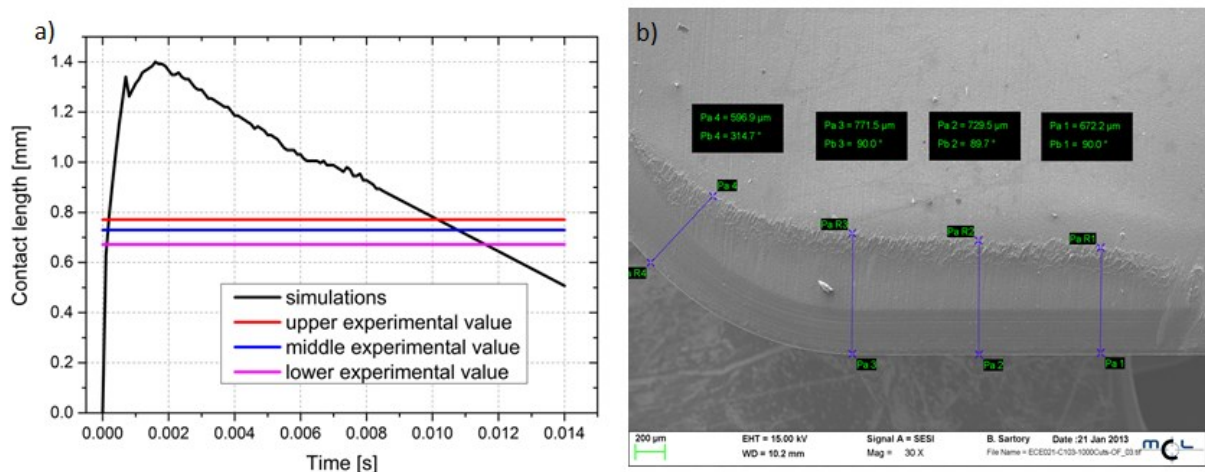
Figure 17: a) Comparison of the simulated and experimental contact lengths, b) rake face surface topography was investigated by scanning electron microscopy.

The simulated and measured tool surface temperatures are presented in Figure 18. The measurements were done by Tamara Teppernegg using thermo-chalks. The tool was painted with the chalk and the milling experiments were performed. The chalk changes its color if a certain temperature is reached. From Figure 18 it can be concluded that on the rake face temperatures of app. 245°C and 335° C were reached at distances of

700 µm and 610 µm from the cutting edge, respectively. At the flank face a temperature of 245°C is reached at a distance of 450 µm from the cutting edge.
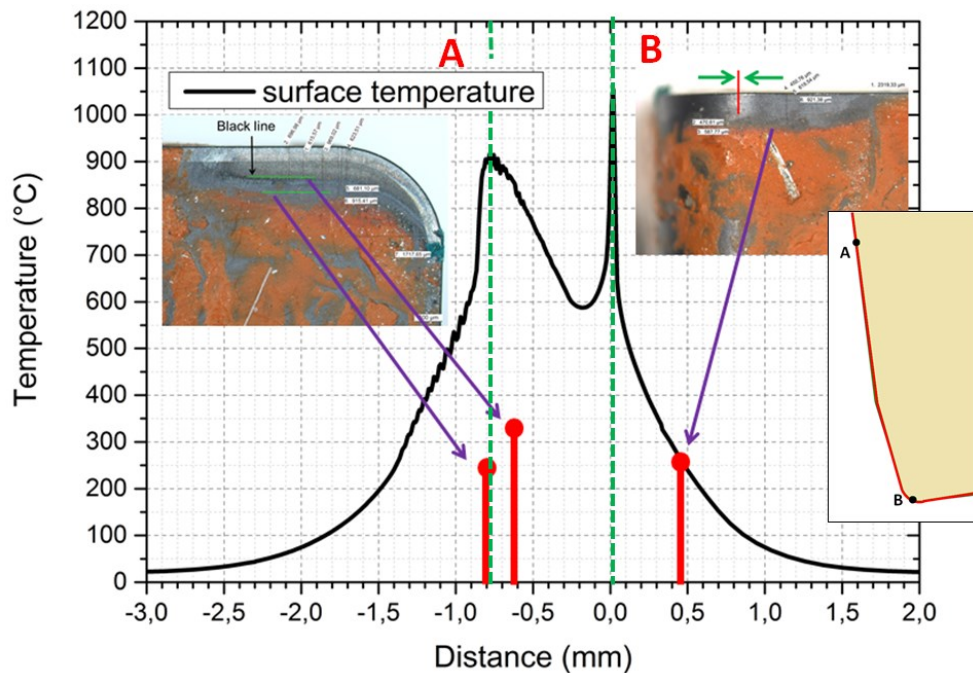
Figure 18: Comparison of the surface temperatures between simulation and thermo-chalk experiments. Zero on the x-axis represents the position of the tool tip.

The temperatures in the contact zone could not be measured in this way because the chalk gets removed during the milling process. It is plausible that in the contact zone temperatures are quite high and close to the simulations but without measurements at this position it can only be a rough estimation. The simulated temperatures are much higher reaching 900°C at the rake face and 1050°C at the tool tip. Temperatures outside of the contact zone (more than 1200 µm away from the tool tip) are similar to the measured ones. The simulated temperature at the flank face fits perfectly to the measured one.

The thickness of the simulated and the experimentally obtained chips is compared in Figure 19. Here, the simulated chip thickness is compared with measurements of three milled chips. The simulation produces a flow chip which is thicker than the measured chips, the latter being longer and serrated.
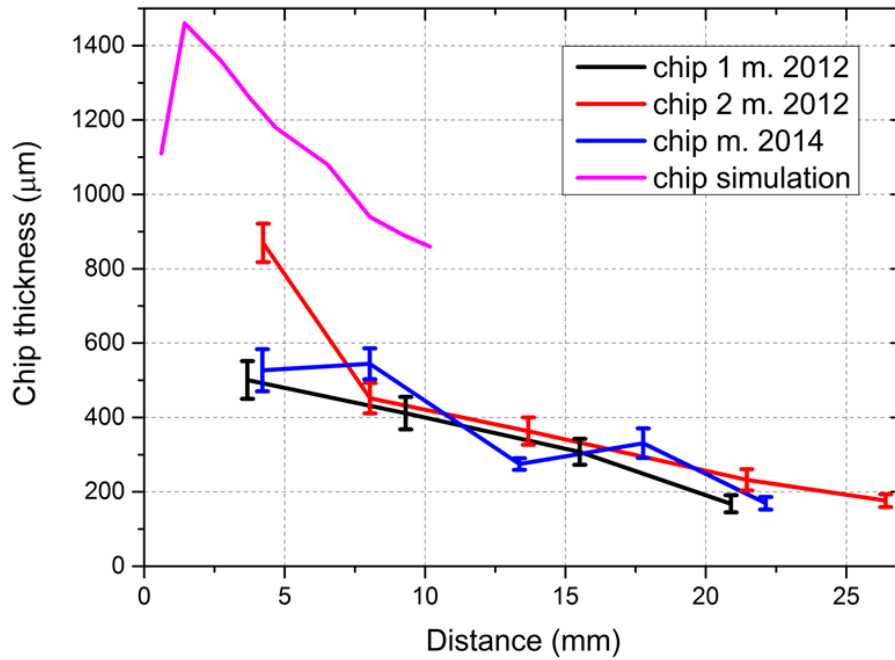
Figure 19: Comparison of the thickness of simulated and experimentally obtained chips at different positions. Experimentally obtained chips were cut perpendicularly to their length. Their thicknesses are measured at the given distances indicated by error bars along the length of the chip. Distance 0 corresponds to the chip tip.

2.3.3 Conclusions of the validation of the FE ALE model

A comparison of the FE ALE orthogonal cutting model with experiments has been performed at the WZL RWTH Aachen. It showed good agreement for most of the compared parameters. Some qualitative differences remain but the same trends are observed both for simulations and experiments.

A FE ALE milling model is able to produce a chip which is thinning with cutting time. Problems of the chip stability in the model were solved by using JC parameters for the workpiece material. This however has the disadvantage of predicting too short and too thick chips as well as too high temperatures in the contact zone. However, the advantage of being able to model longer times of the whole milling process is regarded as more important for the characterization of the tool loading over a whole process cycle.

The validation of the models by the experiments has been partly successful and verifies that the calculated trends of chip formation can be predicted reasonably well. However, absolute measured values of the chip formation are deviating between simulation and experiments. As the aim of the simulations is to obtain reasonable tool loading data for model based design strategies of tools, the produced cutting results can be regarded as a sufficient approximation for this purpose.

2.4 Parametric studies using a FE ALE milling model

Coatings significantly influence the machining performance of tools by acting as thermal barriers [30], [31] and by enhancing the wear resistance [32], [33]. To model how coatings influence the tool loading, analytical and numerical approaches have been proposed to investigate the effect of coatings on the tool temperatures (24), [34], [35], [36].

Grzesik and Nieslony [34] proposed physics based models to obtain average and peak temperatures at the interface between tool and chip for uncoated and multilayer coated HM tools. Their calculations use equivalent thermal conductivities and diffusivities of the deposited coatings and suitable heat partition coefficients. The proposed models predict temperatures which are comparable in values to the temperatures measured via thermocouple during cutting experiments.

An analytical model for one dimensional heat transfer in a monolayer coated tool is presented in [35]. There, a constant temperature at the tool-chip interface is assumed and the temperature development is calculated. The obtained temperature distribution indicates that the thermo-physical properties of the coating and the substrate materials have a significant impact on the temperature distribution in monolayer coated tools.

The thermo-mechanical behavior of coatings under dry cutting conditions is studied using finite element (FE) models in [24]. From their calculated temperature distribution, it is concluded that the heat partition at the tool-chip interface is modified by the presence of the coatings. The study also showed that there is significant influence of the coatings on the temperature values on the surface and inside the tool as well as on the contact pressure and on the cutting- and feed-forces.

Another FE model shows how temperature distributions near the tool-chip contact develop for differently coated tools during turning [36]. The results show a good agreement between predicted and experimentally measured temperatures. The authors demonstrate the existence and the location of a secondary shear zone within the chip. The maximum interface temperature is calculated in the vicinity of the cutting edge. It is shown that the investigated coatings reduce the peak temperatures in the substrate in comparison to an uncoated tool [36], [37].

The aim of this study is to present a new multi-scale FE model of a milling process which can predict in a comprehensive way the temperature fields and stress-strain state

in coated tools. It also serves as a toolbox for parametric studies of different influences on the tool loading.

After 6 ms of simulated milling, the deformed workpiece and the temperatures in tool and workpiece are presented in Figure 20. As expected, the highest temperatures are calculated at the tool-chip interface. The cutting depth decreases with time, reaching 0.25 mm at the presented stage. Therefore, the chip is thicker at the beginning of the milling process and it is thinning as it continues. In the following, the results for the cutting force, the contact length between tool and chip, the temperatures in the tool and the accumulated equivalent plastic strain in the substrate are shown and discussed.
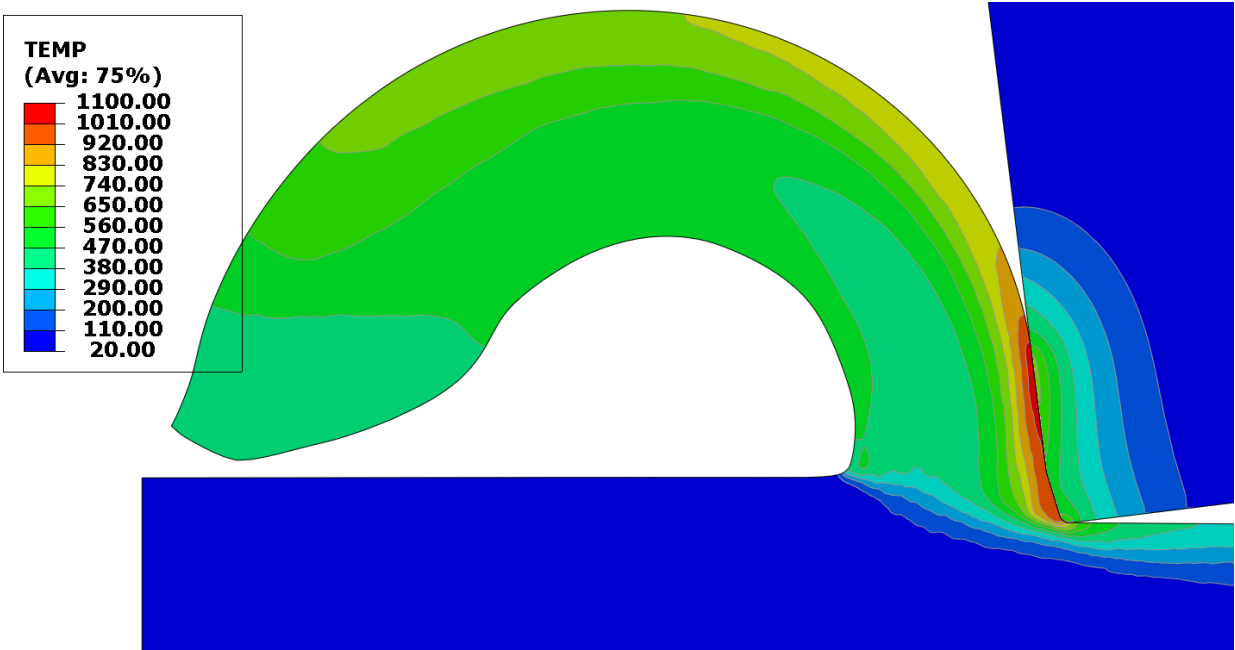
Figure 20: Temperature distribution in the workpiece and the tool after 6 ms of milling time. The tool used in this model is coated with TiAlN. The chip is thinning with progressing milling time as a consequence of the upward movement of the tool. The temperature is measured in °C.

2.4.1 Comparison of the milling and turning models

To obtain a better understanding of the FE milling process model, the calculated cutting force and cutting depth are compared to a model with constant cutting depth, which corresponds to a turning process. The evolution of the force over time is shown for both models in Figure 21a. The model with constant cutting depth shows a slight slope of force over time due to thermal softening of the workpiece material. In the case of milling, the cutting force reduces with decreasing cutting depth and also by the thermal softening of the workpiece material.
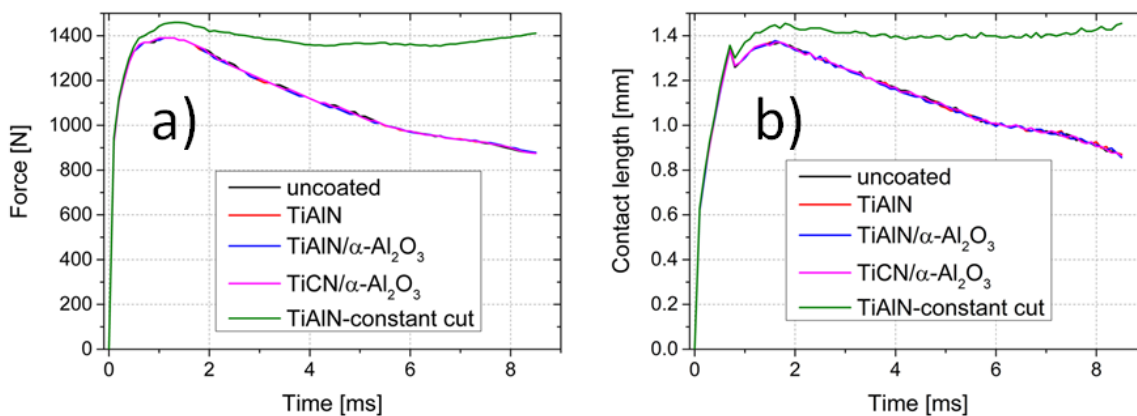
Figure 21: a) Evolution of cutting force versus time for uncoated and coated tools. b) Evolution of contact length versus time for uncoated and coated tools. In both graphs the comparison of the values obtained for the model with constant cutting depth versus models with decreasing cutting depth is shown.

Similar cutting force values are calculated for coated or uncoated tools. This finding differs from results shown in [24], where a lower cutting force is calculated for coated tools due to a hotter and thus softer workpiece material caused by the thermal shielding of the coating. Because the heat transfer coefficient used in [24] is higher than in the model presented in this thesis, the heat exchange between the tool and the chip is faster, leading to enhanced softening of their workpiece material. Additionally, the dependence of their workpiece material properties on temperature is more pronounced.

The evolution of the contact length between the chip and the tool during milling, i.e. the area of contact between them, versus time is presented in Figure 21b. For models with decreasing cutting depth, the contact length decreases steadily after 1.5 ms while for the model with constant cutting depth it remains almost constant with a value of 1.4 mm. As there are no significant differences in cutting forces and contact lengths values

among differently coated and uncoated tools under the assumption of the same friction conditions, there is no difference in contact pressure, similar as in [24].

2.4.2 Influence of hard coating on the tool temperature

The temperature fields in the tool after 8.5 ms of simulated milling are presented in Figure 22 for all investigated models. At points A and B the peak temperatures are obtained. Von Mises stress, temperature and accumulated equivalent plastic strain are plotted as a function of time in point A. The black lines in Figure 22a represent paths *a* and *b*, along which the temperature distributions inside the tool are plotted in Figure 23. Regarding the heat flow into the tool, the highest temperatures are calculated in the first and second element row. The temperatures are decreasing towards the interior of the tool. A comparison of the uncoated and the three differently coated tools shows that the calculated temperatures at the contact surface are lowest for the uncoated tool, similar to findings of [24], [34], [35], [36]. The reason is that the HM substrate exhibits a higher thermal conductivity than the coatings. As a consequence, the zone of higher temperatures inside the tool is larger for the uncoated tool than for the coated tools. Comparing the coated tools, the largest zone of high temperature close to the tool surface is obtained for TiCN/ α-Al$_2$O$_3$, see Figure 22d. This is expected, since TiCN exhibits the highest thermal conductivity value of the investigated coatings. TiAlN and the bilayer TiAlN/α-Al$_2$O$_3$ yield the lowest calculated temperatures in the substrate for the coated tools and do not differ significantly in the calculated temperature fields. Both coating materials are characterized by similar thermal conductivity values, see Figure 22b-c.

Figure 23a and b present temperatures in the interior of the tool, starting at points A and B following the paths *a* and *b*, respectively, see Figure 22a. The temperature in general decreases towards the interior of the tool. The surface temperature of the rake face (see Figure 23a) is highest for the tool coated with TiAlN/α-Al$_2$O$_3$, while it is lowest for the uncoated tool with a difference of almost 100 °C. In the second element row the temperature drops significantly for all three coated tools. The temperature decreases after two element rows (i.e. 7 µm) by more than 150 °C for TiAlN and TiAlN/α-Al$_2$O$_3$, while for the TiCN/α-Al$_2$O$_3$ coating it is reduced by 80 °C. The temperature in the uncoated tool at a depth of 7 µm decreases by 30 °C. At the tool edge (Figure 23b), the temperature distribution is similar to the rake face, with the difference that the highest surface temperature is calculated for TiAlN. Due to higher temperatures at the surface, the temperature differences after two element rows are bigger, reaching a maximum of 370 °C for TiAlN and 340 °C for TiAlN/α-Al$_2$O$_3$. In both Figure 23a and b, it can be seen that the highest temperatures in the substrate are calculated for the uncoated tool and

the tool coated with TiCN/ α-Al$_2$O$_3$, which can be related to their high thermal conductivities. It is evident that coatings with low thermal conductivity serve as a good thermal shield lowering the temperature in the substrate, which is in good agreement with literature (24), [34], [35], [36].
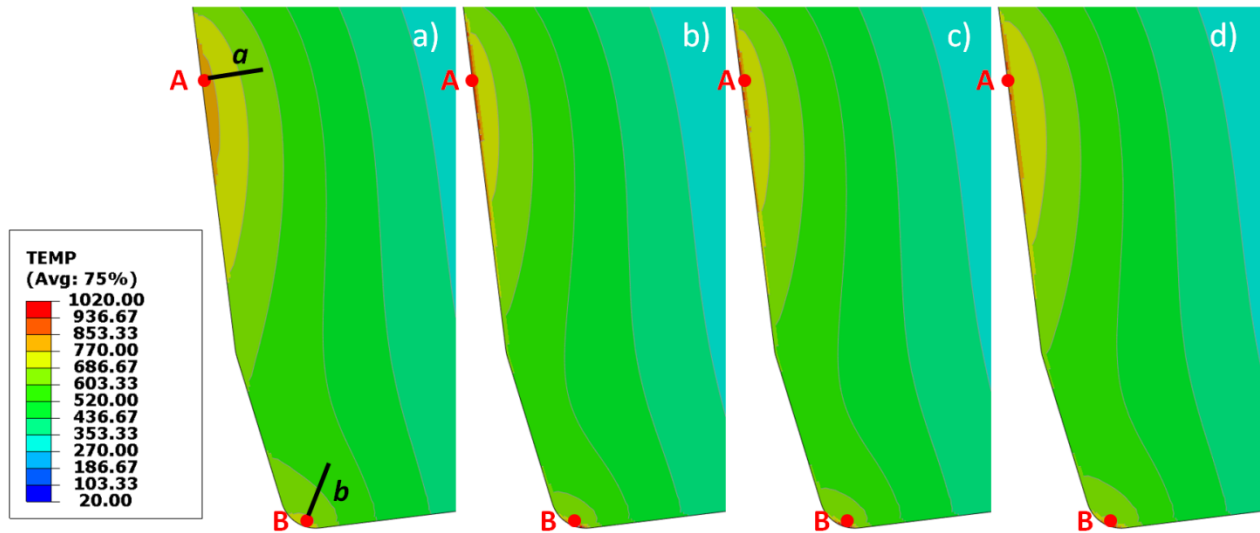
Figure 22: Temperature field in the uncoated and coated tools after 8.5 ms of milling time: a) uncoated, b) TiAlN-, c) TiAlN/α-Al$_2$O$_3$- and d) TiCN/α-Al$_2$O$_3$-coated HM. A and B mark the points of highest load. The evolution of temperatures, von Mises stresses and accumulated equivalent plastic strain as a function of the milling time is plotted at point A (see Figure 24). The temperature field distribution along the depth of the tool is plotted along the paths *a* and *b* indicated by black lines in Figure 23.
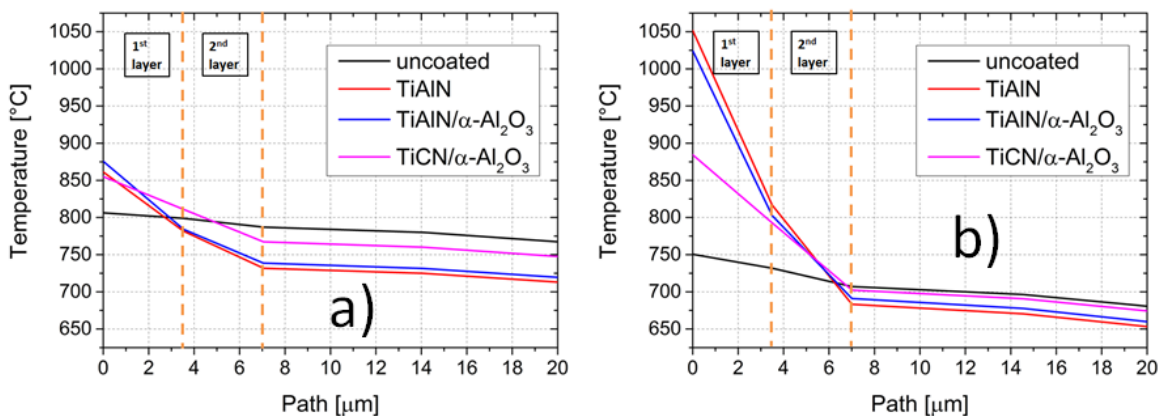
Figure 23: Temperature distribution after 8.5 ms of milling time in the interior of the tool along: a) path *a* and b) path *b*. Dashed lines indicate the thickness of the 1st and 2nd coating layer.

2.4.3 Influence of hard coating on plastic deformation in the substrate

The development of the accumulated equivalent plastic strain, von Mises stress and temperature in the substrate is depicted at 7 µm in depth from point A, see Figure 24a-d. Here, the highest plastic deformation occurs in the substrate, see Figure 26 and Figure 27. A peak of the von Mises stresses is calculated in all investigated tools just at the start of the calculation during the beginning of the chip formation. This peak is calculated just before the chip contacts the tool for the first time. After that, the cutting continues and the von Mises stresses are reduced till they rise again and a second continuous plastic deformation of the substrate starts. During longer cutting times (>0.4 ms), the tool is heated up untill the substrate material weakens and the yield stress and von Mises stress decrease. As a consequence the substrate material plastifies further.
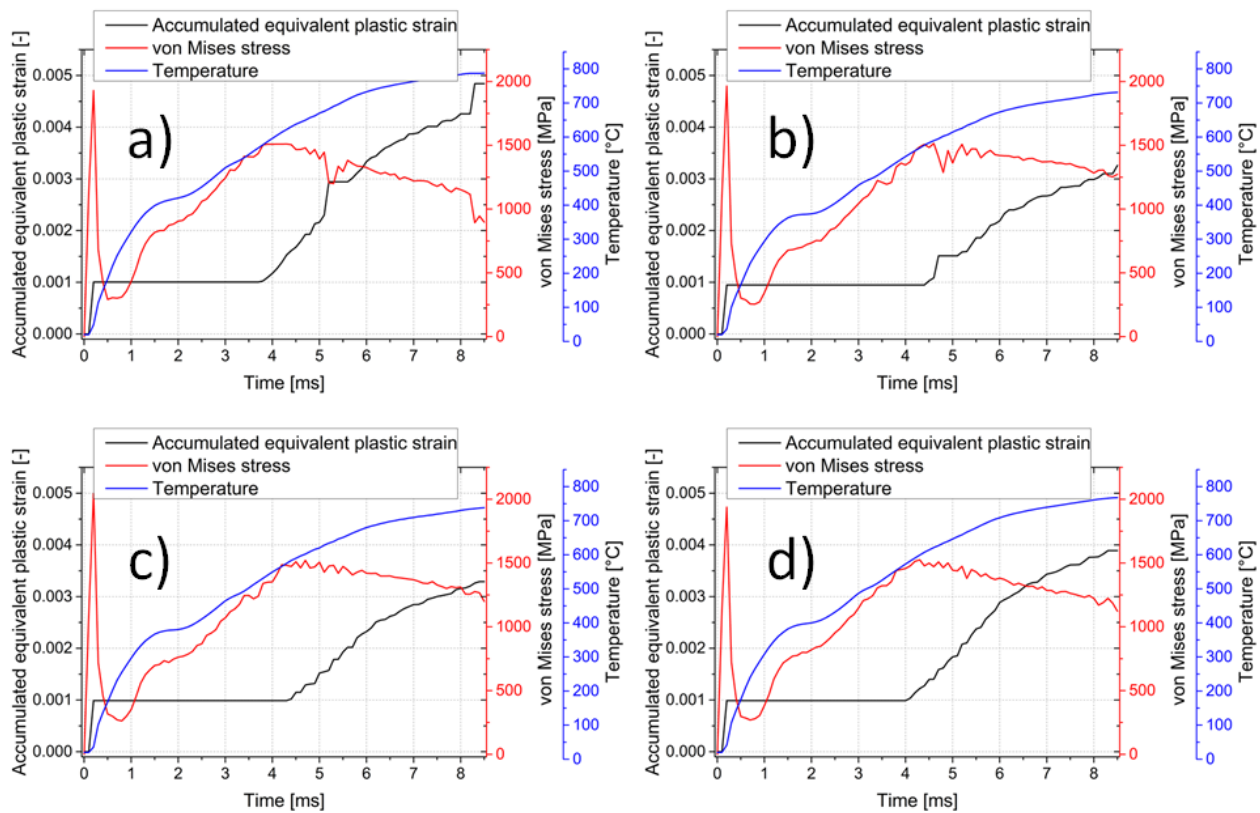
Figure 24: Evolution of accumulated equivalent plastic strain, von Mises stress and temperature versus time in the substrate for: a) uncoated HM tool; and HM coated with b) TiAlN, c) TiAlN/α-Al₂O₃, d) TiCN/α-Al₂O₃. Data are extracted in the substrate at 7 µm in depth from point A, see Figure 25.

The accumulated equivalent plastic strain (PEEQ) field in uncoated and coated tools is presented in Figure 26a-d. The coatings are defined as elastic materials which

41

thus cannot exhibit any plastic strain as indicated by the black stripes in Figure 26b-d. Some differences can be observed in the amount and location of plastic deformation in the substrate. The temperatures near the tool surface in a depth of 7 µm are higher for the uncoated tool than for coated tools as can be seen in Figure 22 and Figure 23. The HM is softer at higher temperatures and thus it plastifies to a greater extent. Figure 22d shows that the TiCN/α-Al$_2$O$_3$ coated tool exhibits the highest temperatures in the substrate among the coated tools. Thus, the substrate softens and shows the highest PEEQ among the coated tools, see Figure 23d. The TiAlN and TiAlN/α-Al$_2$O$_3$ coated tools reduce the plastic deformation in the tool substrate more effectively than TiCN/ α-Al$_2$O$_3$.

The PEEQ in the substrate at a depth of 7 µm along the coating-substrate interface are shown in Figure 27, following the red curve indicated in the insert at the top left corner. The highest absolute plastic strain (PEEQ) values are obtained at the rake face (point A). The plastic strains are highest for the uncoated tool and are decreased in the coated tools, especially the coatings containing TiAlN due to its low thermal conductivity.
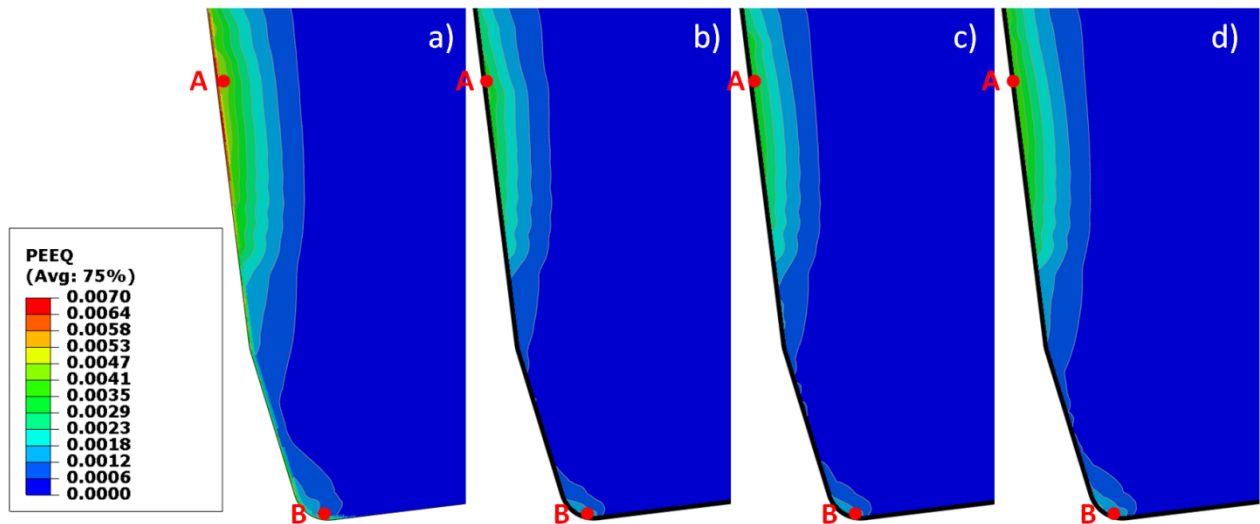
Figure 26: Accumulated equivalent plastic strain field in the uncoated and coated tools after 8.5 ms of milling: a) uncoated HM tool; HM coated tool with b) TiAlN, c) TiAlN/α-Al$_2$O$_3$, d) TiCN/α- Al$_2$O$_3$.

The question arises to what extent the thermal expansion coefficient of the coatings influences the plastic deformation of the substrate. To tackle that issue two artificial thermal expansion coefficients are defined based on the values for TiAlN. The first coefficient has 50% and the other one has 150% of the original value of the thermal expansion coefficient of TiAlN, see Figure 28. All other parameters remain the same. The

tool models are then given coatings with one of these three sets of parameters each. The results are presented in Figure 29.

The results in Figure 29 show that different values of the thermal expansion coefficient have no major effect on the plastic deformation of the substrate on the rake face of the tool. There is a peak at point A for the tool coated with α_{TiAlN} 50%, but the rest of the plastic deformation on the rake face of the tool is similar for all three coefficients. The thermal expansion coefficient has an influence at the tool edge, at point B. There the tool coated with α_{TiAlN} 50% has the lowest plastic deformation, while the tool coated with α_{TiAlN} 150% shows the highest plastic deformation. It is even higher than the plastic deformation of the uncoated tool and the tool coated with TiCN/α-Al$_2$O$_3$, see Figure 27. From these results it can be concluded that high values for the thermal expansion coefficient influence the plastic deformation of the tool substrate in the small extremely hot zone at the tool edge, i.e. at position B.
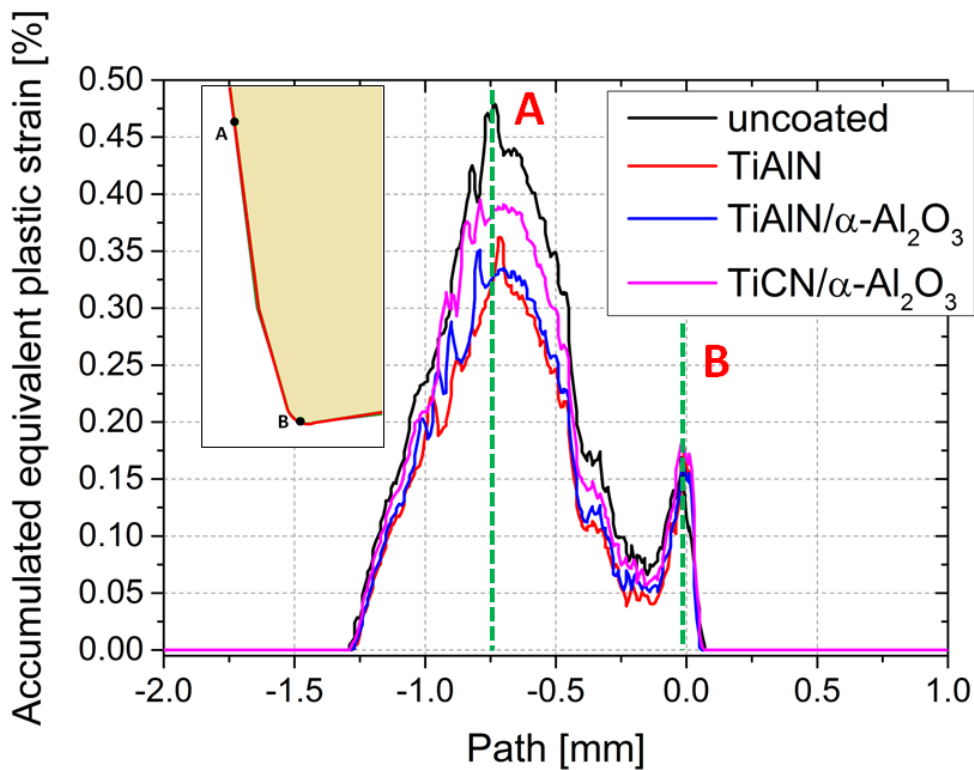
Figure 27: Accumulated equivalent plastic strain along the tool surface in a depth of 7 μm for uncoated and coated tools after 8.5 ms of milling time.
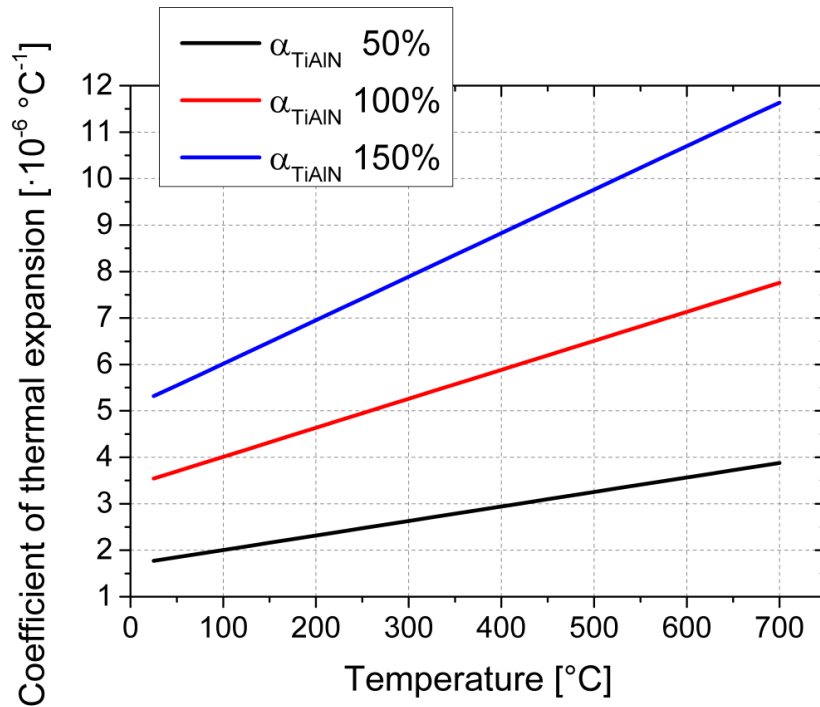
Figure 28: The 50%, 100% and 150% lines of the measured thermal expansion coefficient. The reference temperature for the thermal expansion coefficient is 20°C.
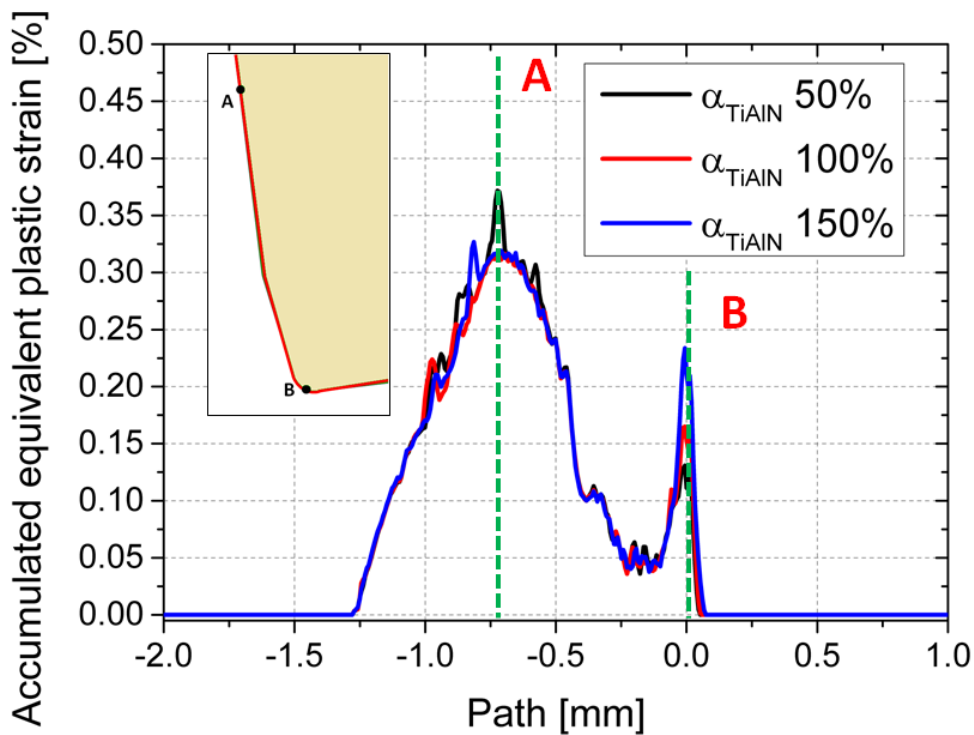
Figure 29: Accumulated equivalent plastic strain in the substrate along the tool surface in a depth of 7 μm for tools coated with TiAlN whose thermal expansion coefficient varies from 50-100% after 8.5 ms of milling time.

The model includes thermal stresses due to different expansion of the coatings relative to each other and to the substrate but does not consider residual stresses originating from tool production. A further development of the tool model has to take into consideration the development of stresses in the coatings regarding the whole heating and cooling process during milling as this will be in the 3D milling process model presented in chapter 3.

2.4.4 Influence of the substrate material properties on the plastic deformation of the substrate

The effect of the hardness of the coatings on plastic deformation of the substrate is also studied for three different hard metals: WC with 6 wt. % Co, WC with 8 wt. % Co and WC with 10.5 wt. % Co. The tools are coated with the TiCN/α-Al$_2$O$_3$. The flow curves of the three hard metals are presented in Figure 30. It can be seen that the HM grade WC with 6 wt. % Co is the hardest material, HM grade WC with 10.5 wt. % Co is the softest material and WC with 8 wt. % Co is in between.
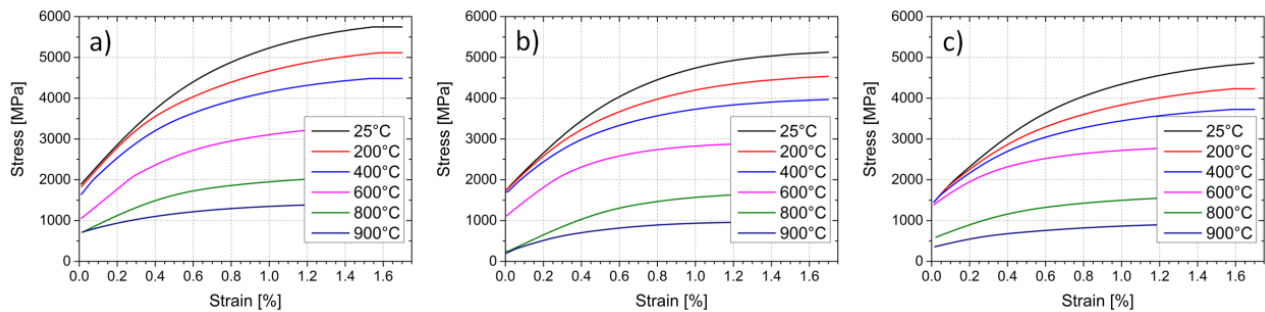
Figure 30: HM flow curves: a) WC with 6 wt. % Co, b) WC with 8 wt. % Co and c) WC with 10.5 wt. % Co.

Table VI provides a ranking of the thermo-physical properties of the HM and compares them to the simulation results of temperature and plastic strain. The detailed thermo-physical properties of the HM grades are presented in Appendix A. This table is used as a scheme to understand how different parameters influence the substrate's plastic deformation.

Figure 31 shows the accumulated plastic strain in the individual substrates. The distance follows the red line indicated in the upper left corner. The highest level of plastic deformation is calculated for the softest HM grade, namely WC 10.5 wt. % Co, while the hardest HM grade WC 6 wt. % Co exhibits the smallest amount of plastic deformation.

Table VI.

A ranking of the thermo-physical properties of the HM and of the calculated temperature and plastic strain results for different HM grades.

	Thermal conductivity	Heat capacity	Thermal expansion	Flow stress	Substrate surface temperature	Accumulated plastic strain
MORE	WC 6wt.%Co	WC 10.5wt.%Co	WC 10.5wt.%Co	WC 6wt.%Co	WC 10.5wt.%Co	WC 10.5wt.%Co
	WC 8wt.%Co	WC 6wt.%Co	WC 6wt.%Co	WC 8wt.%Co	WC 8wt.%Co	WC 8wt.%Co
LESS	WC 10.5wt.%Co	WC 8wt.%Co	WC 8wt.%Co	WC 10.5wt.%Co	WC 6wt.%Co	WC 6wt.%Co
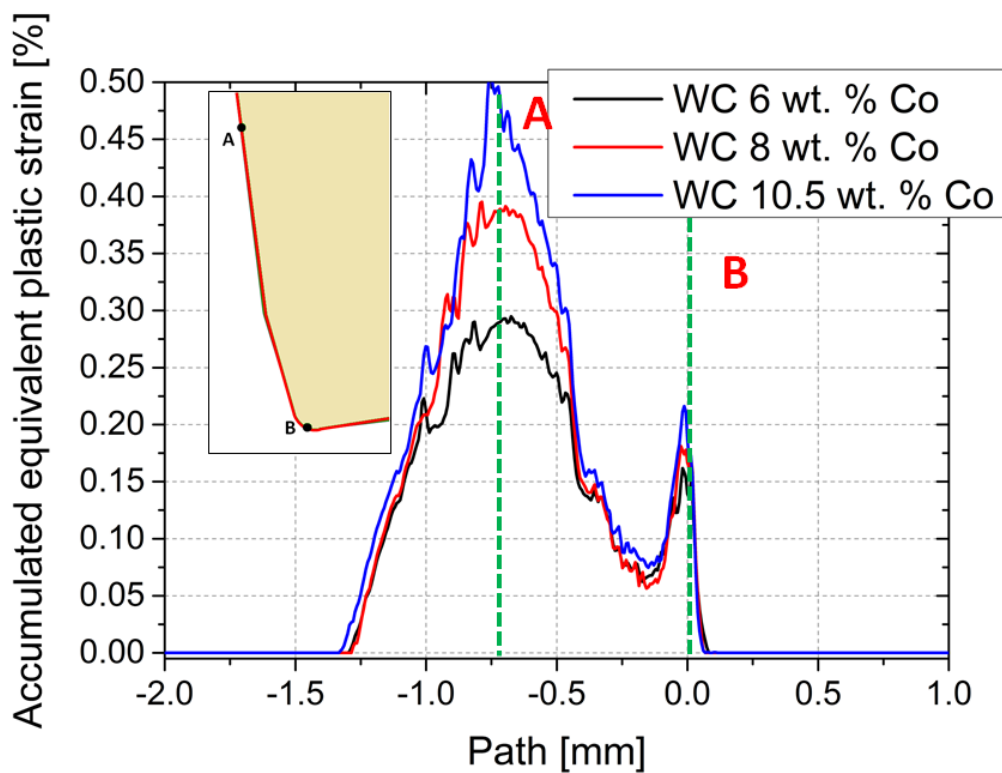
Figure 31: Accumulated equivalent plastic strain in three different HM grades along the tool surface in a depth of 7 μm coated with TiCN/α-Al$_2$O$_3$ after 8.5 ms of cutting.

HM WC 6 wt. % Co has a high thermal conductivity which allows heat to move faster away from the coating/substrate interface and to distribute in the interior of the substrate. That reduces the temperature at the coating/substrate interface. The heat capacity has the middle value among the studied HM grades. This means that a

46

moderate value of heat can be stored and is necessary to increase the temperature in the material. With high thermal conductivity and intermediate values of heat capacity, temperatures remain lower compared to other grades. Lower temperatures produce lower thermal expansion. In combination with a low thermal expansion coefficient, as it is the case for WC 6 wt. % Co, the stresses produced due to thermal expansion are low. The flow stress values of WC 6 wt. % Co are highest among the investigated HM grades even at high temperatures. A combination of lowest temperatures, lowest thermal stresses and high flow stresses results in the lowest plastic deformation of the investigated HM grades. The opposite applies to the HM grade WC 10.5 wt. % Co. It has a low thermal conductivity which doesn´t allow fast heat flow. The high heat capacity adds in a beneficial way because more heat can be stored than in the other investigated HM grades. The thermal expansion coefficient is the highest one and with high temperatures near the substrate surface, this grade will generate high thermal stresses. Since the flow stress values are the lowest the combination with high thermal stresses and high temperature, results in high accumulated plastic strain.

2.4.5 Conclusions of influences of the hard coatings and substrate material properties on the plastic deformation of the substrate

It can be stated that for the reduction of plastic deformation in the substrate, a deposition of a hard coating with low thermal conductivity acting as a thermal shield is needed. An example of a coating which positively influences and reduces plasticity is TiAlN. Low thermal conductivity coatings should be used together with a HM substrate exhibiting a high thermal conductivity. The substrate should also have high heat capacity, low thermal expansion and a high flow stress especially at higher temperatures. A very good example for such a substrate is the HM grade WC 6 wt. % Co which exhibits all of these characteristics excluding a high heat capacity. The FE milling model predicts for this kind of material properties a low plastic deformation of the tool. Thus a longer service life will be the consequence.

2.4.6 The influence of friction on the mechanical tool wear

The friction between the chip and the tool causes tool wear and produces heat. These effects can again be studied with the 2D FE milling model. The tool is coated with a 7 µm thick TiAlN layer and the substrate used is the HM grade with 8 wt:% Co. A Coulomb friction model with a shear stress limit is used. The principle of this model states that if the shear stress between the chip and the tool exceeds a certain limit, the traction stress is cut-off and the model will use a shear dependent sliding between the surfaces in contact. In this chapter the shear stress limit model is used in comparison to a model of Coulomb friction without shear stress limit. The models are tested for three friction coefficients, μ: 0.2, 0.4 and 0.6. The heat produced due to friction is equally distributed into the chip and the tool.

Frictional heat is produced by the specific frictional work in the surface over time. The specific frictional work and the specific frictional power in one time-increment produced in the contact surface are calculated from contact pressure, slip and slip rate. From the contact pressure $p_c(t)$, the slip rate $v_s(t)$ and the coefficient of friction μ, the specific frictional power $P_f(t)$ can be calculated as [38]:

$$P_f(t) = \mu p_c(t) v_s(t) \tag{21}$$

The unit of the specific frictional power is W/mm². It is closely related to the maximum arising temperature in the contacting surfaces, since this temperature will be highest where the highest input rate of frictional heat occurs. In the literature [39], however, it is stated that the specific frictional power also indicates a shift in the wear phenomena. The integral of the frictional power over time gives the frictional work per unit area [38]:

$$W_f = \int_t P_f(t) dt \tag{22}$$

In our calculations, a discrete form of equation (22) is used:

$$W_f = \mu \sum_i p_{c,i} \Delta s_i \tag{23}$$

where i goes from first output frame until the end of the calculation time, $p_{c,i}$ is the contact pressure and Δs_i is the slip distance at a particular time increment. This specific frictional work is widely associated with wear. Its unit is J/mm². In Archard's wear law [40], for example, the wear depth equals the frictional work times an empirical wear constant divided by the hardness of the material.

Figure 32a and Figure 32b show the specific frictional work exhibited at the tool surface. The results in Figure 32a are obtained for the model without shear stress limit whereas Figure 32b shows the results of the model with shear stress limit. The existence of the shear stress limit increases the specific frictional work as the sliding increases. It does not have an effect on the model with a friction coefficient of 0.2 because in that model the shear stress does not reach the shear stress limit.
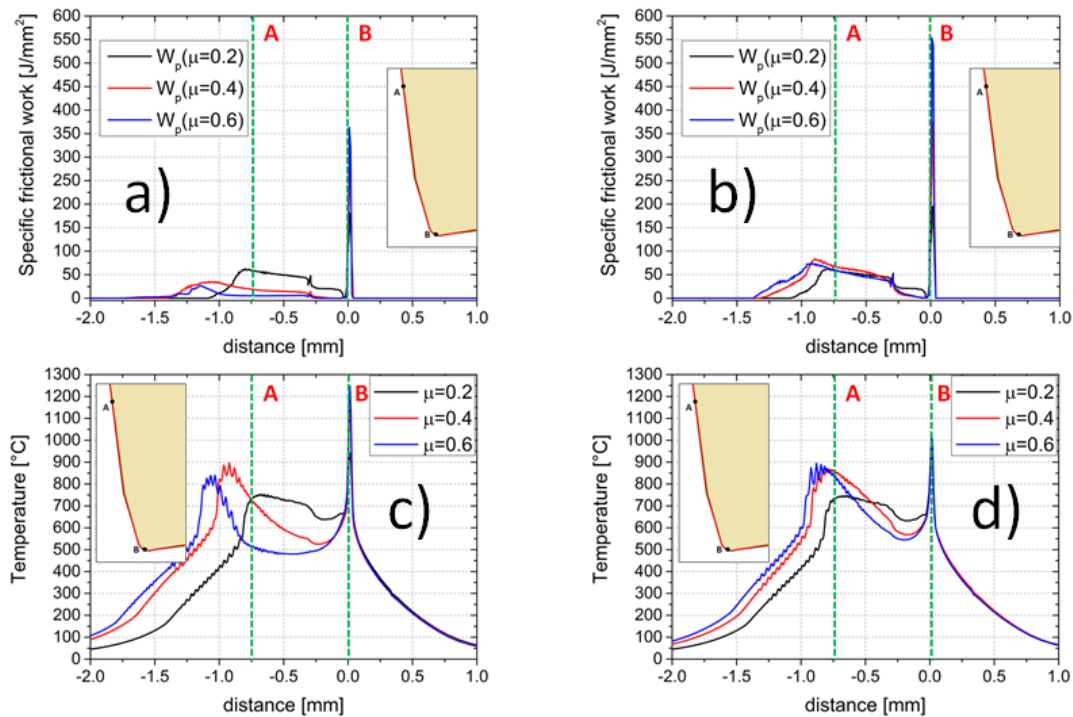
Figure 32: Specific frictional work for three different friction coefficients along the tool surface for a model a) without shear stress limit and b) with shear stress limit. Surface temperature for three different friction coefficients c) without shear stress limit and d) with shear stress limit. Values are plotted after 7.5 ms of simulated cutting time.

In Figure 32c and Figure 32d the tool surface temperatures are shown. The temperature peaks correspond to the peaks in the specific frictional work. With increasing friction coefficient for the model without shear stress limit the temperature peaks at the rake face (around point A) increase. Also the peak temperatures are shifted to the left from point A, further away from the tool edge, if the contact zone expands.

In Figure 33 the specific frictional power is shown at points A and B. The values are higher at point B (Figure 33c and Figure 33d). Also the values for the models with shear stress limit (Figure 33b and Figure 33d) have higher values than those without shear stress limit (Figure 33a and Figure 33c). At point A and B the values are fluctuating with

time for both frictional model types. At point B a frictional coefficient of 0.6 on average generates the highest values for the specific frictional power.
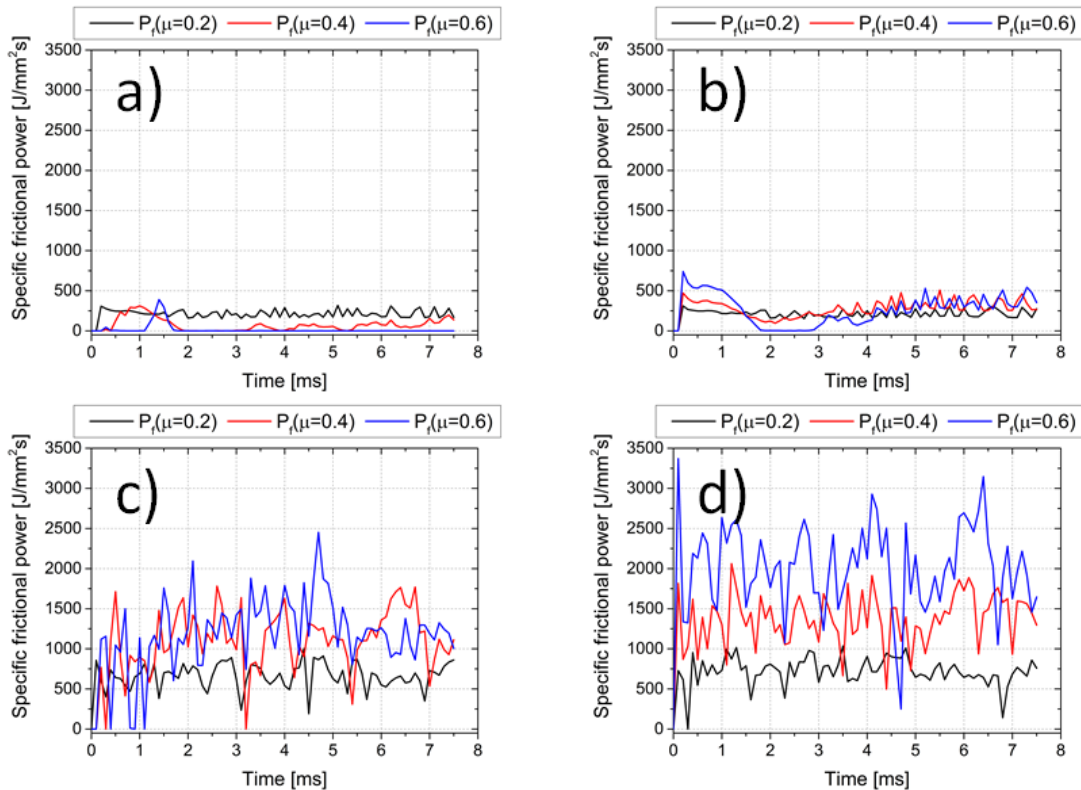
Figure 33: Specific frictional power for three different friction coefficients at points: a) A without shear stress limit, b) A with shear stress limit, c) B without shear stress limit and d) B with shear stress limit. Values are plotted up to 7.5 ms of cutting time.

To reduce the surface temperature and consequently the substrate temperature, the hard coating (HC) should have a low friction coefficient. This will reduce the specific frictional work, the temperatures at the tool surface and the specific frictional power. It is important to reduce the specific frictional power because the position of biggest mechanical wear is correlated to positions of the peaks of the specific frictional power [38], [41]. The geometry of the tool will influence the location and the height of the maximum frictional power. An optimized geometrical tool design may reduce the peaks. If all these parameters, i.e. frictional coefficient and tool geometry, are reduced the mechanical tool wear will decrease, too.

2.4.7 Behaviour of a worn-out tool

In this chapter a model of a worn-out tool is presented. It is intended to represent the damage of the coating due to mechanical wear which is assumed to have removed a part of the coating on the tool edge, see Figure 34. In Figure 17b one example of a worn-out tool is presented.

As a base for modeling of the worn-out tool the standard 2D representation of the milling tool is used. To keep things simple the tool is coated with a single layer TiAlN indicated with light blue color in Figure 34. The geometry of the tool is modified in a way that the coating is removed from the tool edge. The transition from uncoated to coated parts is modeled with a thickening of the coating. Two different contact laws are defined as indicated with green and red lines in Figure 34. The green lines are indicating the standard contact law with a friction coefficient of 0.4. The contact of the worn-out part of the tool with the workpiece is indicated with a red line where a friction coefficient of 0.6 is used. For both contact laws the standard shear stress limit is used.
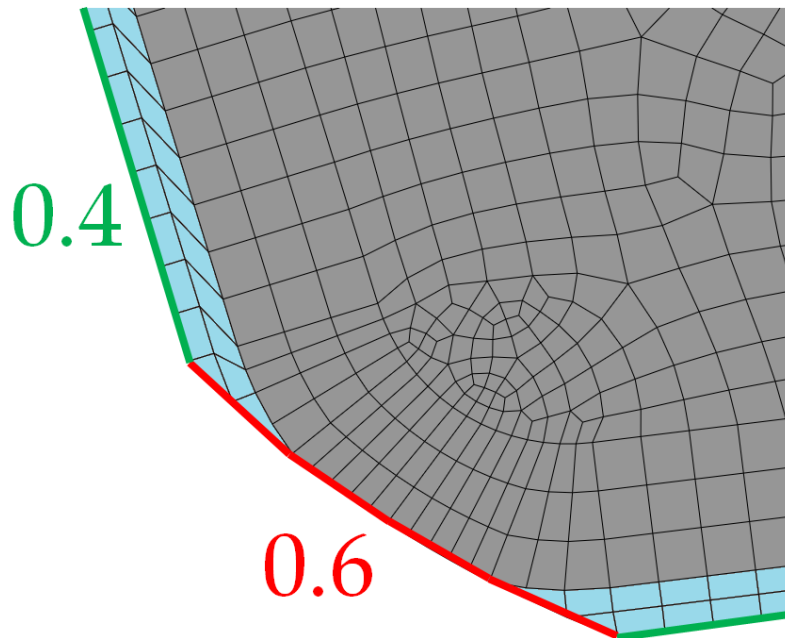
Figure 34: Geometry of the worn-out tool. The coating is represented with light blue color and the substrate with gray color. The green and red lines are indicating where the friction coefficients of 0.4 and 0.6 are used.

A comparison of the plastic strains of the standard and the worn-out tool is shown in Figure 35. The plastic deformation of the unworn tool is more severe close to the tool surface and it decays towards the interior. The worn-out tool does not show such a

gradual plastic deformation. As in the unworn tool the highest plastic deformation is close to the surface, but it is more localized at several small islands. The highest plastic deformation is observed at the lower part of the tool edge near the interface of the substrate and coatings. In general the worn-out tool exhibits higher plastic deformation.
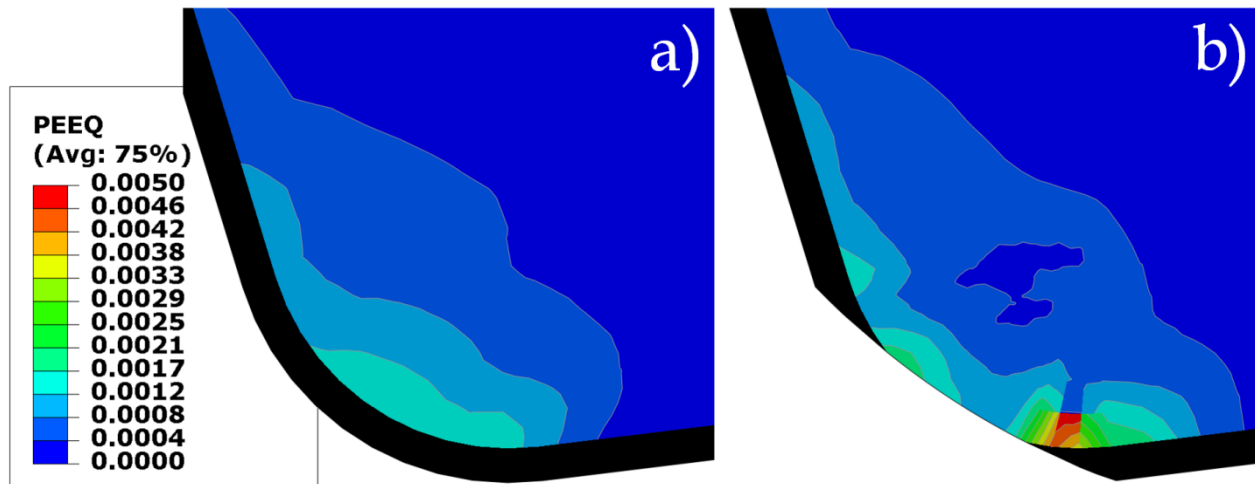
Figure 35: Plastic deformation of the substrate in: a) unworn tool, b) worn-out tool.

In Figure 36a, the cutting forces of the unworn and worn-out tools are compared. The compared forces are almost equal. The worn-out tool requires slightly higher force to cut the workpiece material. The reasons are the less sharp edge of the tool and the higher friction coefficient in the area of the uncoated part of the tool edge.

In Figure 36b, the temperatures of the substrates of the unworn and worn-out tool are compared. The temperature in the worn-out tool substrate is slightly higher at the whole rake face and also at the tool edge. Obviously, the heat-influx is larger through the uncoated part which heats up the whole tool.

To estimate the differences in the mechanical wear the values of the heat influx and the values of the specific frictional work are compared, see Figure 36c. There is no difference in the specific frictional work at the rake face of the tool. A difference appears at position B, the position of the worn-out edge, with a two times higher influx of the heat caused by the higher specific frictional work due to the higher friction coefficient and the blunter edge.

The plastic deformation of the substrate is presented in Figure 36d. As expected, the plastic deformation at position B is much higher for the worn-out tool due to the higher influx of heat. The plastic deformation is also higher at the rake face of the tool. To explain this behavior the evolution of PEEQ, von Mises stress and temperature versus time is presented at point A in Figure 37.

52
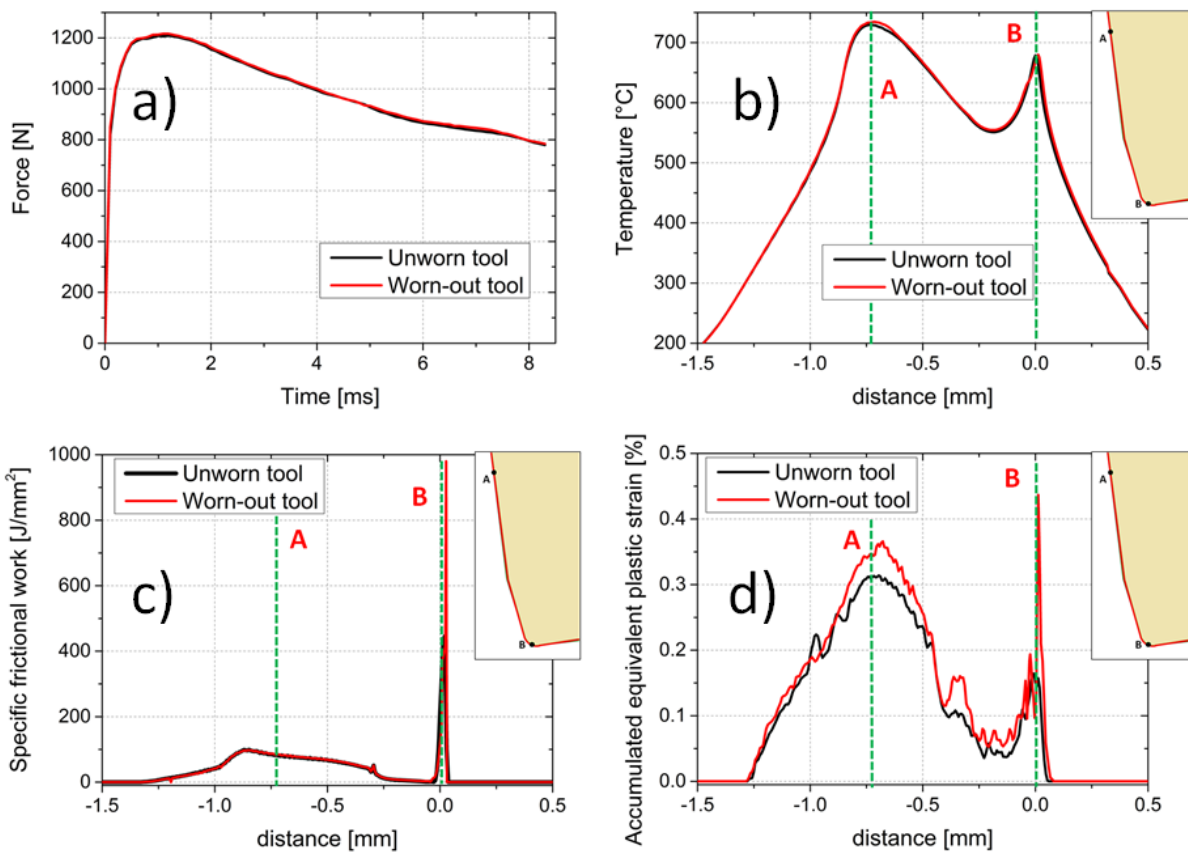
Figure 36: Comparison of calculated variables for the unworn and worn-out tool: a) cutting forces, b) substrate surface temperature, c) von Mises stresses at the substrate surface and d) substrate surface plastic deformation.
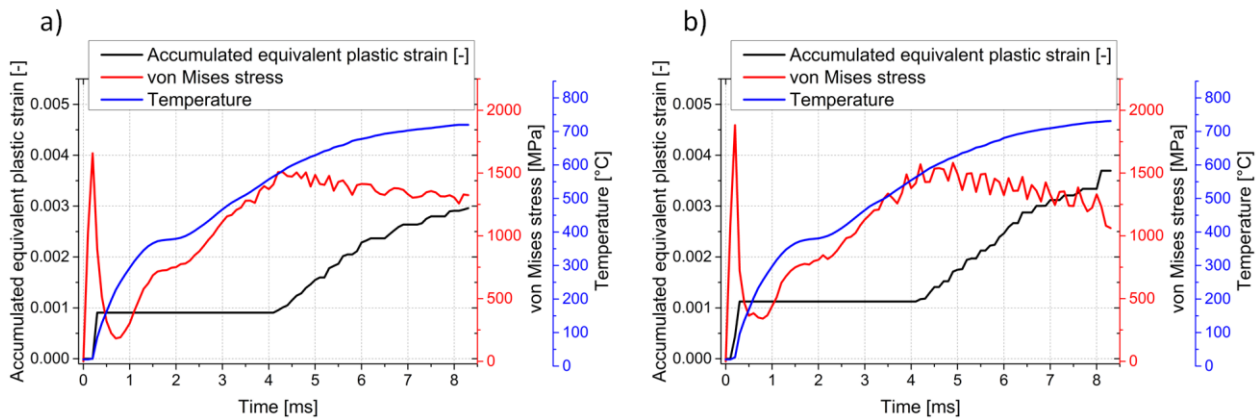
Figure 37: Comparison of three variables calculated for the a) unworn and b) worn-out tool: evolution of PEEQ, von Mises stress and temperature.

The results in Figure 37 show that the temperature at the surface for both tools is almost the same during the whole cut. A first difference in plastic deformation between

the tools occurs at around 0.25 ms. It coincides with the peak of the von Mises stress. The von Mises stress is around 250 MPa higher in the worn-out tool which causes a higher plastic deformation of the substrate. As the cutting continues, the von Mises stress keeps steadily increasing resulting in a higher plastic deformation at the end of the cut. The same process occurs at the rest of the rake face causing high values of the plastic deformation.

3 3D milling process model

3.1.1 Introduction

A 3D tool model is created to study the out-of-plane stresses during a cutting or milling process in the substrate. They are of particular interest because they are assumed to be the cause for combcrack formation [3]. In [3], the evolution of residual stress is investigated by X-ray diffraction and damage mechanisms are identified for the tool over its lifetime. Their findings are compared to results produced by the 3D model.

In [3], the formation of combcracks is described. At the rake face of the tool, the substrate is plastically deformed under elevated temperatures and the mechanical load during milling. During the cooling stage of the process these conditions in the substrate cause a build-up of out-of-plane tensile stresses. A sudden decrease in the tool temperature close to the surface during cooling produces a thermo-shock which causes higher tensile stresses and initiates additional plastic deformation. It is assumed that this thermo-shock thus leads to nucleation and growth of combcracks.

Out-of-plane stresses can no longer be captured using 2D models since none of the available options provided by the FE programs apply. In plane stress elements for instance all out-of-plane stresses are by definition zero due to the fact that elements can freely expand in out-of-plane direction. The very localized nature of the contact problem also prevents the use of the plane strain model or even generalized plane strain elements since the stress and strain peaks will decay rapidly in out-of-plane direction. So, the contact problem at hand corresponds by no means with the ideal case of a plane strain state where the situation in one cross-section keeps repeating itself in out-of-plane direction. The only way for evaluating the out-of-plane stresses is to set-up a full 3D model. However, the cutting process itself cannot be performed using a 3D model since the small-size of the coatings requires a mesh-size which can be provided in 2D models only.

3.1.2 Modelling approach

The simplified 3D tool milling process model is created in combination with the 2D milling model. It uses the load and temperature input of the 2D milling model. The geometry, elements and sections of the 2D tool are automatically imported into a 3D model using a Python script. The geometry of the 3D model is built from the 2D tool geometry. The 2D tool plane is used as base for the 3D tool. The additional parallel 2D planes are added and connected which creates the thickness in the z-direction. The thickness of the 3D model can be varied. Also, the width of the loading zone can be varied. The loading zone is the area of the tool on which mechanical and thermal loading is applied. The model consists of 468702 elements. The element type used for the thermal analysis is DC3D8. It is 3D element with 8 nodes used for heat transfer analysis. The element type used for the mechanical analysis C3D8R, 3D element with 8 nodes and reduced integration. The dimensions, the loading zone and the boundary conditions are indicated in Figure 38.
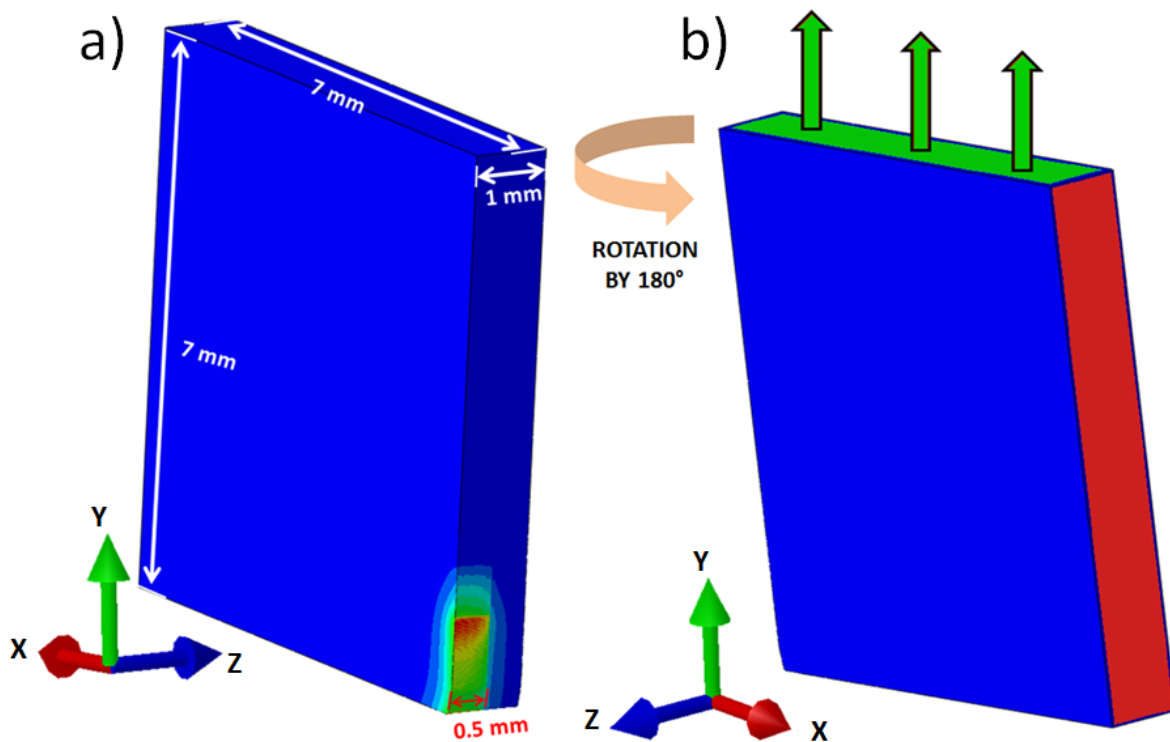
Figure 38: a) Dimensions of the 3D tool model are indicated with white arrows and the width of the loading zone is indicated with a red arrow. b) Boundary conditions applied on the 3D tool. The green arrows indicate the motion of the tool in upward direction. The red and blue surface indicate boundary conditions which restrict motion in x- and z-directions, respectively.

The applied loading on the 3D tool has to represent the cyclic loading of the tool during milling operations. The investigated milling process consists of 14 ms of loading and 92 ms of idle time. The loading is extracted from the 2D milling simulations. Figure 39 presents a scheme of this process. First, the FE milling simulations are performed using the 2D model. Second, the Python script extracts the temperatures at the surface of the tool and applies them at the surface of the 2D FE tool model preparing them for a third step which is the calculation of the temperature fields in *Abaqus/Standard*. This calculation produces the same temperature fields as in the standard FE milling model, but due to the inherent *Abaqus* structure, the heat fluxes calculated with *Abaqus/Explicit* cannot directly be used as a loading in *Abaqus/Standard*. Fourth, from the calculated results in *Abaqus/Standard* another Pyhton script creates a file called "HEAT FLUX FILE". In this file the heat flux history is stored as an *Amplitude input file* which can in a next step be applied as thermal load on the 3D tool. The fifth step transfers the normal and shear forces using a Python script into "FORCES FILE" which is again an *Amplitude input file* for appling the mechanical loading on the 3D tool. The tool is tilted by 7° when positioned at the miller head during milling experiments. The script takes that into account and recalculates the 2D forces using this tilt.
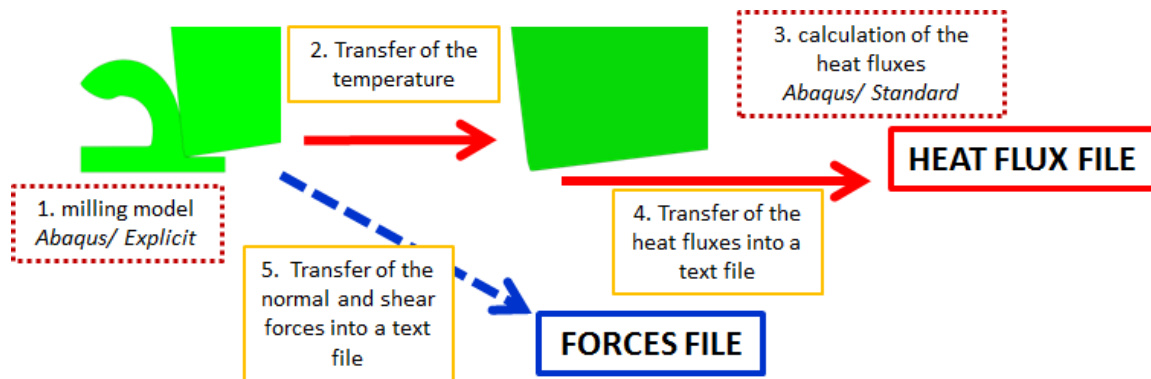
Figure 39: Scheme of the process modeling approach: extraction of the heat fluxes and forces from the 2D milling model for application as a tool load in the 3D combcrack model.

The 3D tool loading calculations are divided into two parts: thermal analysis and mechanical analysis. The scheme of the thermal analysis is presented in Figure 40. The calculations are done by applying the heat flux via the HEAT FLUX FILE as thermal loading. During the idle part the heat fluxes are removed and the heat redistributes in the interior of the tool. In the second cycle the heat fluxes are applied again and removed at the beginning of the idle part. Using this approach, the desired number of process cycles can be produced. After the selected number of cycles has been calculated, the produced *Abaqus output database* (*.odb*) is used as a TEMPERATURE PROCESS FILE containing the temperature fields of the 3D tool as they evolve with time. The

TEMPERATURE PROCESS FILE is then used for the mechanical calculations as an input file.
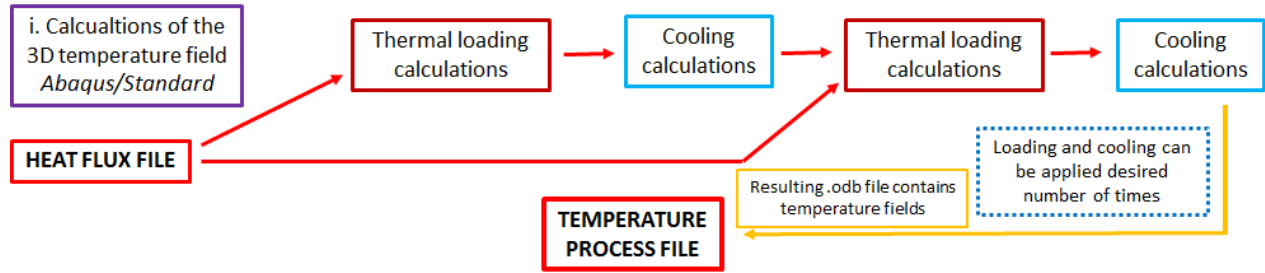
Figure 40: Scheme of the process modeling approach: modeling of the cyclic thermal loading by a cyclically applied heat flux and a temperature redistribution step in the cooling phase.
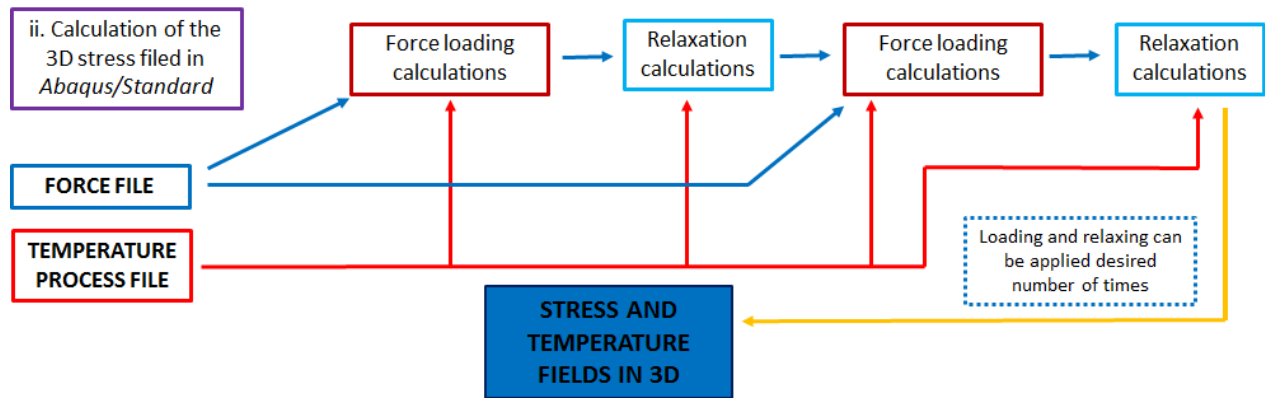
Figure 41: Scheme of the process modeling approach: modeling of the cyclic mechanical loading by a cyclically applied force. The temperature load is applied in the correct time schedule simultaneously.

The mechanical calculations are structured in a similar way as the thermal calculations. The forces are applied using the FORCE FILE in the loading part of the cycle and they are removed at the beginning of the idle part. They can be applied as many times as necessary. Parallel to this procedure the temperature fields are used from the TEMPERATURE PROCESS FILE because all mechanical data also depend on the temperature. The final results of the calculations are written to an .odb file which contains stress, strain and temperature fields in the 3D tool model. The scheme of the model is presented in Figure 41.

3.1.3 Analysis of the milling process over multiple milling cycles

The results of the 3D simulations of the milling process are evaluated after 10 cycles and subsequent relaxation to room temperature (RT). Each cycle consists of a

loading/cutting period of 14 ms and an idle/cooling time of 92 ms. In the eleventh part, i.e. the relaxation to RT, the tool temperatures are set to RT (20 °C). The relaxation to RT allows calculation of the residual stresses.
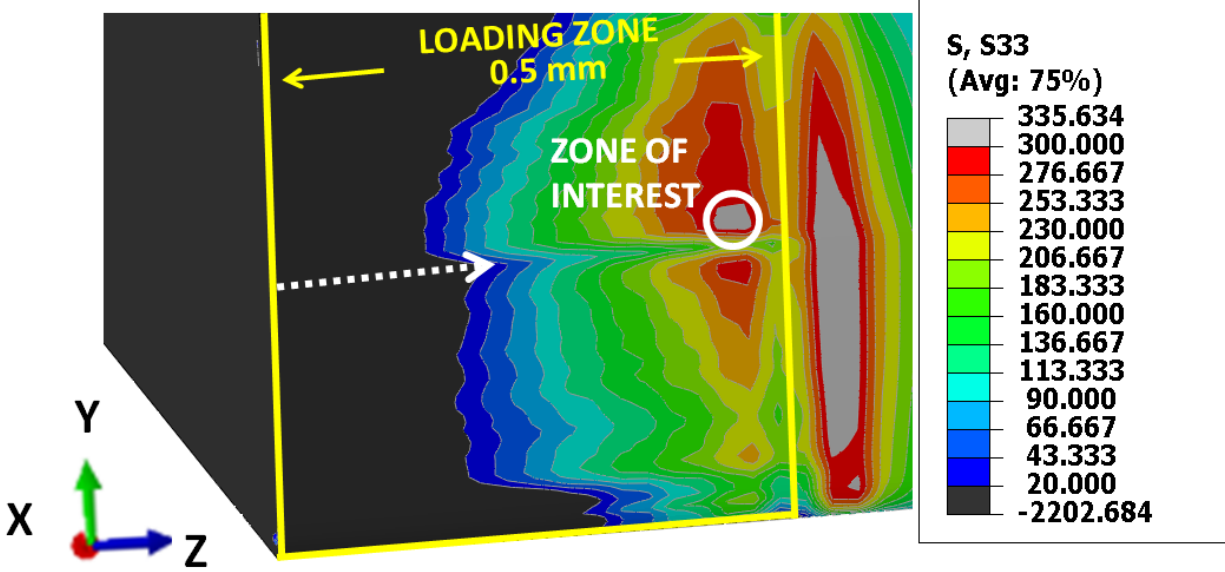
Figure 42: The distribution of the out-of-plane stress in the tool. The compressive out-of-plane stress is represented by the dark area, while tensile out-of-plane stresses are represented by colors. A white dotted arrow indicates the line of the chamfered edge. The *zone of interest* **is indicated by a white circle and shows the area of the highest out-of-plane stresses.**

In Figure 42 the 3D tool is presented at the end of the calculation showing the results for the out-of-plane stress in the substrate. The loading zone is indicated by yellow lines. The dark area of the tool represents compressive out-of-plane stresses. Tensile out-of-plane stresses are represented by colours. The maximum values of tensile out-of-plane stresses are found in the proximity of the chamfered edge of the tool and on the right hand side of the loading zone. They are indicated with a white circle and named *zone of interest*. The maximum of tensile out-of-plane stresses are experimentally found at the same position as reported in [3]. The X-ray diffraction measurements were taken from the surface of the substrate to a depth of 5 µm. The thickness of the elements in the *zone of interest* is 7.5 µm and the results are extracted at the center of the element. This means that data acquired in simulations and experiments are taken from the same depth.
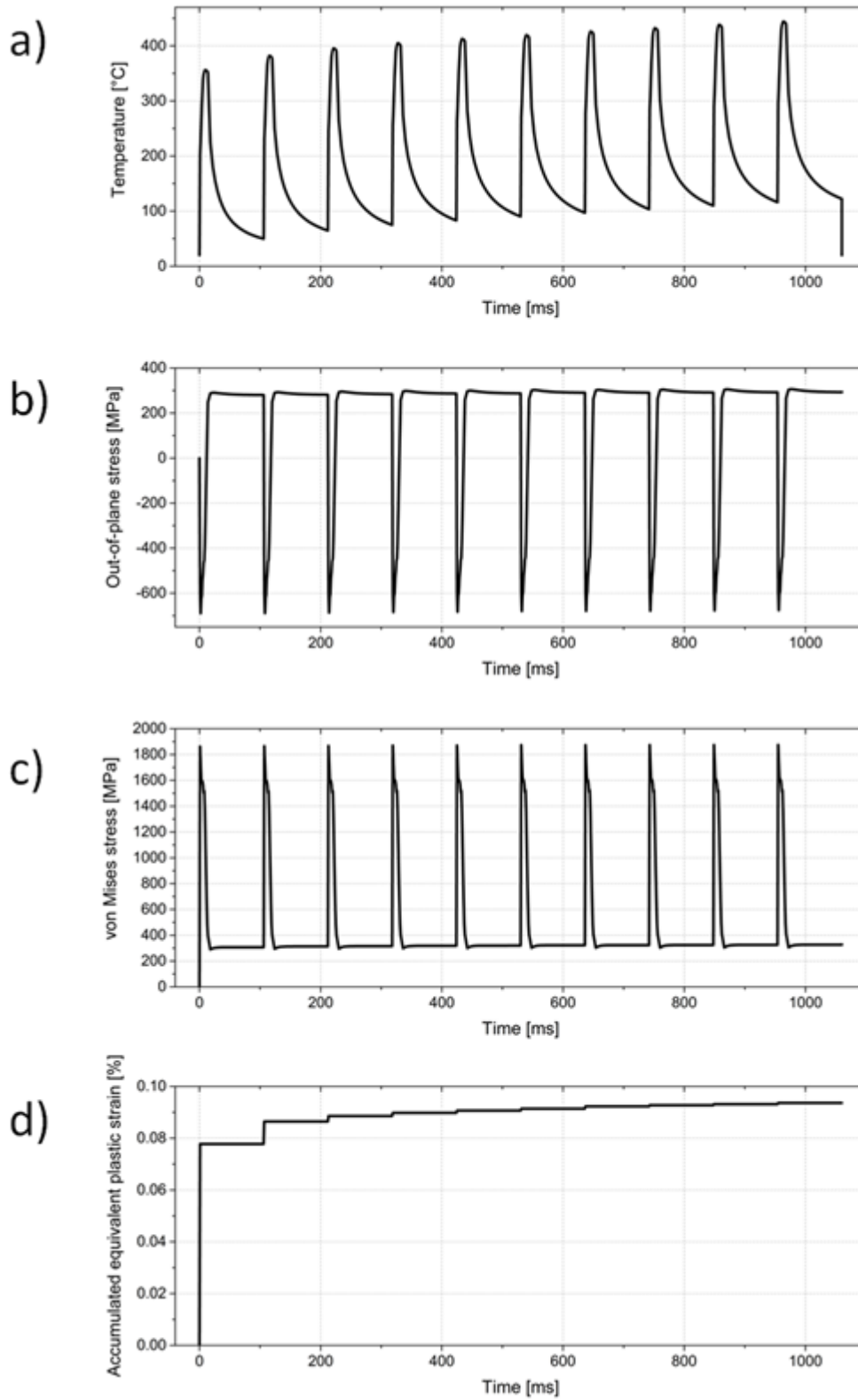
Figure 43: Evolution of : a) temperature, b) out-of-plane stress, c) von Mises stress and d) PEEQ in the *zone of interest* over 10 cycles.

The *zone of interest* is selected to study the values of the out-of-plane stress, temperature, PEEQ and von Mises stress as time dependent variables. The *zone of interest* consists of 21 elements divided in 3 rows with 7 elements each. The values of the mentioned variables presented in graphs are averaged over that zone.

In Figure 43a the evolution of the temperature in the *zone of interest* is shown. The temperature rises at the beginning of each cycle. The peak temperatures are observed at the end of each loading part of the cycle. After the first loading the temperature peak reaches 350°C and after the tenth loading the peak is at 445 °C. During the idle part of the cycle the heat redistributes and the highest temperature gradient is found at the beginning of the cooling within the first 5 ms. During the rest of the cooling the temperature gradient decreases.

After each cycle the total temperature increases. In the first cycle it increases by 30 °C, after the second cycle by 15 °C and after the third by 10 °C. In the following cycles it increases by around 7 °C. After the tenth cycle the temperature in the tool is lowered to RT in order to determine the residual stresses after tool operation. The temperature peaks are not related to the peaks of the von Mises or out-of-plane stresses.

The development of the out-of-plane stress is presented in Figure 43b. The out-of-plane stress decreases and becomes compressive at the beginning of each loading part of the cycle. The peak is reached at 2 ms of loading. The minimum value of the out-of-plane stress calculated during the first cycle is -689 MPa. After 10 cycles there is a slight change in the minimum value to -676 MPa.

The maximum tensile out-of-plane stress occurs after the beginning of the idle part of the cycle. The high temperature gradient which causes the thermo-shock increases the tensile out-of-plane stresses. They reach their maximum at 8 ms of the cooling part of the cycle. In the rest of the cooling part they slightly decrease. The maximum tensile out-of-plane stress increases steadily from 290 MPa in the first cycle to 306 MPa in the tenth cycle. The difference is 16 MPa which yields an average increase of 1.6 MPa per cycle. A very rough extrapolation gives an increase of 1600 MPa after 1000 cycles. It is still under debate whether the stresses reach saturation after many cycles.

The residual out-of-plane stress after each cycle increases from 280 MPa after the first cycle to 293 MPa after the tenth cycle. The relaxation to RT produces a further increase by 1 MPa, i.e. to 294 MPa, hence an effect of the thermo-shock is not observed. The average increase is 1.4 MPa per cycle. The linear extrapolation yields after 1000 cycles 1400 MPa of residual out-of-plane stress. In [3] it is reported that the compressive

out-of-plane stresses in a virgin tool are measured around -850 ± 270 MPa. After 1000 cycles the measured stress is 930 ± 230 MPa. The average difference is 1780 MPa which is in good agreement with the extrapolated results of the simulations. The residual out-of- plane stress develops mainly in the first cycle and increases steadily in later cycles.

The Von Mises stress reaches its peaks at the beginning of each loading part of the cycle, after 1 ms, as direct consequence of the mechanical load. It increases from 1862 MPa in the first cycle to 1875 MPa in the tenth cycle. After reaching the peak the von Mises stress starts to decrease quickly even during the further loading part of the cycle.

The plastic deformation of the tool occurs at the beginning of each cycle in the first ms of loading and it coincides with the peak of the von Mises stress. At the beginning of the cycle the temperature of the tool is still low, from 200 °C in the first cycle to 295 °C in the tenth cycle, which means that plastic deformation occurs in a relatively cold tool with high von Mises stress. As the von Mises stress is caused by the mechanical load, so is the plastic deformation of the tool. The majority of the plastic deformation happens in the first cycle where the PEEQ reaches 0.078%. In the tenth cycle the PEEQ value is 0.094%. In Figure 12c the flow curves of HM with 8 wt. % Co are presented and these curves are used for the material model of the substrate. From there it can be concluded that the substrate during the first ten cycles is in a state where for a given temperature the yield stress is quite high and thus no significant amount of plastic deformation is to be expected. As the temperature increases during multiple cycles the plastic deformation in the substrate will increase. The PEEQ reaches 83% of its maximum already in the first cycle. In the second cycle it reaches 92% and in the third 95% of the maximum value.

The out-of-plane stresses are not high enough to cause plastic deformation of the substrate during the first 10 cycles. With more cycles the stresses will increase and together with an increase of the temperature will decrease the yield stress value of the substrate, see Figure 12c. Under these conditions the out-of-plane stresses may well be able to plastically deform the substrate.

As conclusion, the temperature rises steadily from cycle to cycle and, together with the increase of the von Mises and tensile out-of-plane stresses, a bigger plastic deformation seems possible after a high number of cycles (>100). The largest fraction of residual out-of-plane stresses and plastic deformation occur in the first three cycles. This makes shorter 3 cycle calculations suitable for basic parametric studies. One such study is presented in the next section.

3.1.4 Influence of loading and cooling time

During milling experiments it is not always ensured that even under equal conditions all the cuts have the same length and time duration. In the first milling cycles as well as in the last ones, the produced chip is usually shorter. If the milling time is shorter than the idle part of the cycle where the tool cools down, the idle part has to be longer due to constant rotation speed of the miller head. The question is to what extent this kind of process influences the build-up of tensile out-of-plane stresses or plastic deformation of the tool.

In this work this problem is approached in the following way. Three models are created and three cycles are simulated. The first model, Model 1, has a standard duration of the loading part of 14 ms and an idle part of 92 ms. The second, Model 2, has a duration of the loading part of 6 ms and an idle part of 100 ms. Model 3 is a combination of the first two models. The first cycle has a duration of the loading part of 6 ms and an idle part of 100 ms. The second cycle has a duration of the loading part of 14 ms and an idle part of 92 ms. The third cycle repeats the first cycle.
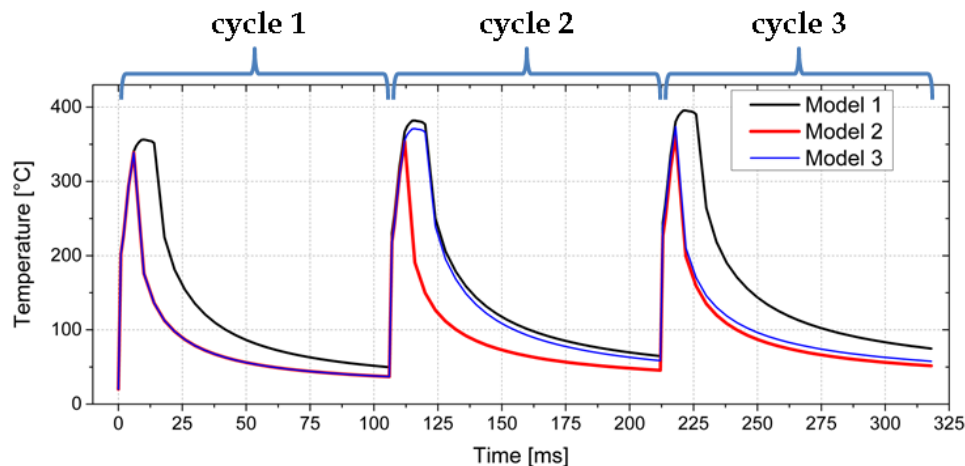
Figure 44: Evolution of temperature in the *zone of interest* over 3 cycles for models with different length of loading and cooling cycle durations.

In Figure 44, the temperature development in the *zone of interest* is presented. The temperature rises from cycle to cycle for each model. After the first cycle the temperature is highest for Model 1 due to a longer period of applied thermal load on the tool, whereas Model 2 and Model 3 exhibit the same temperatures. In the second cycle again Model 1 yields the highest and Model 2 the lowest temperatures. The same is true for the third cycle. In the second cycle Model 3 results in the second highest temperature peak almost reaching the temperature of Model 1, but in the third cycle it is again very similar to Model 2 due to the heat redistribution during the idle part of cycle 3.
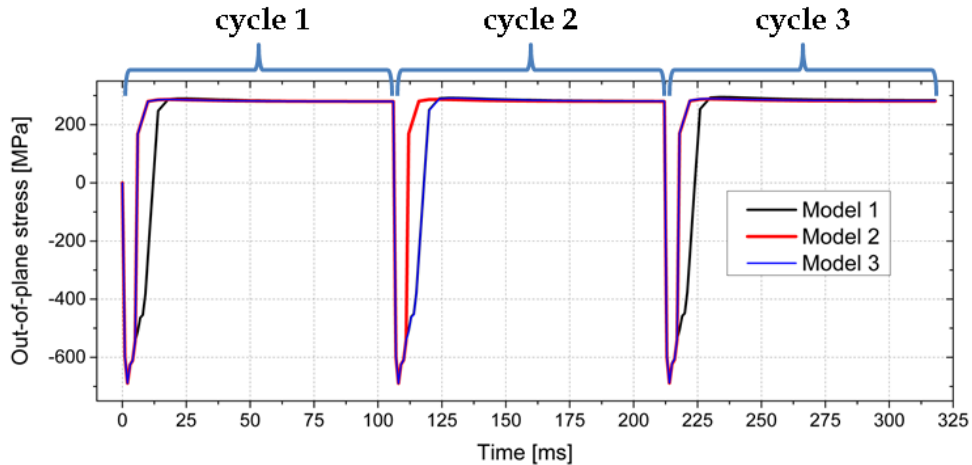
Figure 45: Evolution of out-of-plane stress in the *zone of interest* over 3 cycles for models with different length of loading and cooling cycle durations.

The evolution of the out-of-plane stress is shown in Figure 45. The bands of compressive stresses coincide with the length of the loading part of the cycle. As soon as the loading is removed, the out-of-plane stresses revert to be tensile. They reach their maximum values in Model 1 in all three cycles. Model 2 and 3 have the same peak values in the first cycle but in cycle 2 and 3 Model 3 exhibits higher values. The residual out-of-plane stresses after each cycle follow the same pattern like the maximum values. A correlation can be noticed between higher out-of-plane stresses with higher temperatures and longer loading parts of the cycle.

The von Mises stress in the *zone of interest* is plotted in Figure 46. The maximum values do not differ between the three models. In the first cycle they reach 1862 MPa and in the third cycle they remain at 1864 MPa. Again like for the out-of-plane stress the bands of elevated stress can be correlated to the length of the loading part of the cycle. At higher temperatures, when the substrate is more easily plastically deformed, the width of the bands could have more importance. If the stress remains longer at a higher value while the temperature increases, additional plastic deformation can occur.

The plastic deformation of the substrate model occurs immediately at the beginning of the loading. Surprisingly it differs for all three models even though the von Mises stress has the same value in all three models. The reason lies in the different temperatures in the substrate. The plastic deformation in the first cycle occurs for all three models at the same temperature of 20 °C. In cycle 2 Model 1 has a higher temperature of 231 °C while for Model 2 and 3 it is 219 °C. The substrate undergoes a higher plastic deformation at higher temperatures and thus Model 1 exhibits a higher value of PEEQ under the same mechanical load. The situation from cycle 2 repeats itself

in cycle 3 and Model 1 shows again a higher PEEQ due to higher temperatures of the substrate. The temperature at the beginning of cycle 3 for Model 2 is 227 °C and for Model 3 239 °C. Thus, Model 3 results in a slightly higher PEEQ value.
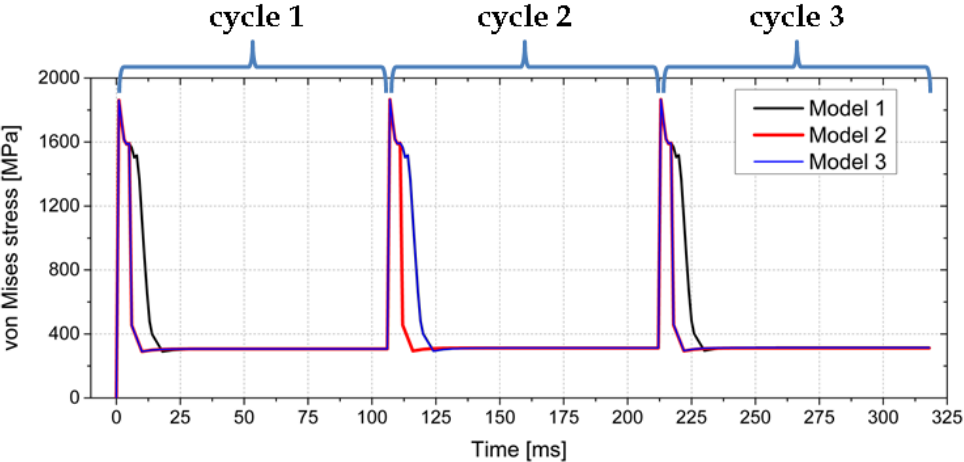
Figure 46: Evolution of von Mises stress in the *zone of interest* over 3 cycles for models with different length of loading and cooling cycle durations.
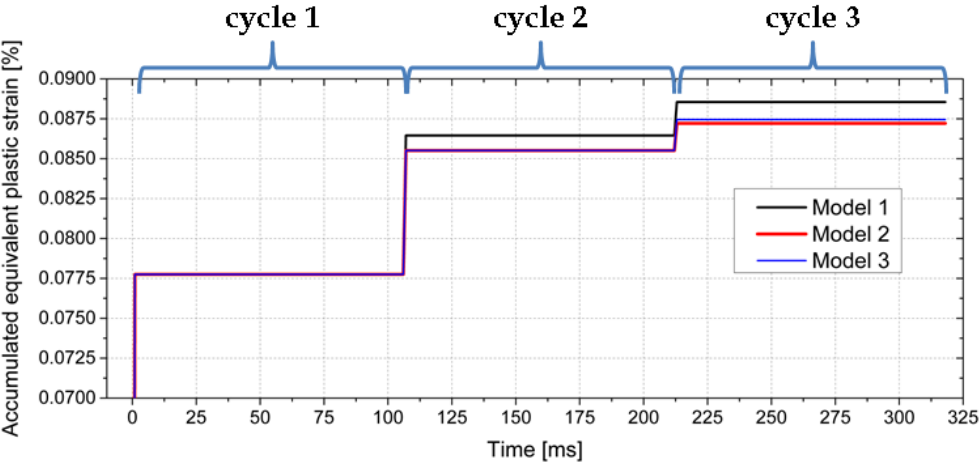
Figure 47: Evolution of PEEQ in the *zone of interest* over 3 cycles for models with different length of loading and cooling cycle durations.

3.1.5 Conclusions of 3D milling process model results

A 3D tool milling process model has been developed based on the 2D ALE milling model. It is fully automated using Pyhton scripts. It enables calculations of stress, strains and temperature fields in 3D during cyclic loading and unloading of the tool. The number of cycles which can be simulated is only limited by the available computational resources.

The model provides reasonable results which are in accordance with experimental results presented in [3]. The *zone of interest*, at which high tensile out-of-plane stresses are observed, is at the same position where experimentally combcracks and residual tensile stresses are observed. The process of plastic deformation of the substrate during the first cycles at lower temperatures is well understood and described. The results of the first cycles can be extrapolated to forecast further possible plastic deformation at higher temperature both under the influence of loading and tensile out-of-plane stresses. During the cooling part with high temperature gradients tensile out-of-plane stresses are calculated but did not reach values high enough to cause plastic deformation of the substrate.

Three models are presented with different loadings and cooling times during one cycle. All three models undergo the same stresses, but after three cycles they exhibit different amounts of plastic deformation. The different plastic deformation can be explained by different periods of thermal exposure and thus temperatures in the substrate thus giving rise to differing plastic deformation.

4 General conclusions

In this work the behaviour of a tool during milling has been studied using a FE modelling approach. An ALE formulation has successfully been applied and state-of-the-art 2D orthogonal cutting and milling process models have been developed. FE modelling is also used to develop a 3D tool milling process model. New experimentally measured data for coatings and HM have been presented and used in the simulations. The numerical results have been compared to the experiments, yielding reasonable agreement.

The 2D FE ALE orthogonal cutting simulations have been validated using orthogonal cutting tests at various speeds and cutting depths. The numerical results of the most important parameters for the tool loading, namely cutting forces, contact length and temperatures are comparable but in most cases are 10 to 15 % higher than the experimental results. This difference is in the acceptable range and shows that numerical simulations can be used to determine the tool loading.

The parametric studies using the 2D FE ALE milling model provide the following guidelines for the tool design as summarized here:

- The results of the 2D milling model show that the plastic deformation of the substrate can be reduced in two ways:

    i. The hard coating has to have a low thermal conductivity which keeps the heat outside of the substrate lowering its temperature.

        - At lower temperatures the substrate has the higher yield stress value and it will be more resistant to plastic deformation.

        - An example of a low thermal conductivity coating is TiAlN.

    ii. The substrate should have these characteristics:

        - High thermal conductivity which allows faster redistribution of the heat in the substrate, thus reducing the temperature in the loading zone of the tool.

        - High heat capacity to increase the amount of heat necessary for an increase in temperature.

- Low coefficient of thermal expansion which reduces the thermal stress of the substrate.

- High values of the flow stress.

- An example of a substrate with positive characteristics is HM grade WC 6 wt. % Co.

- The 2D milling model shows that a lower friction coefficient between the tool and the workpiece will lead to lower temperatures in the loading zone, which is a consequence of less produced specific frictional work and power.

  - If the specific frictional power is lower, than there will be less mechanical wear.

- The 2D milling model of the worn-out tool indicates the importance of coatings as thermal shield and shows that damaged worn-out tools induce higher cutting forces.

The results of the 3D tool process model show:

- The development of the tool temperature and its gradual increase over ten cycles can be quantified.

- The formation of tensile out-of-plane stresses is obtained in the same region around the chamfered edge of the tool as shown by experiments.

- The effect of the thermo-shock during the first milliseconds of the cooling part of the milling cycle on the build-up of tensile out-of-plane stresses is shown.

- The development of the substrate's plastic deformation is described for the first ten cycles. This plastic deformation takes place under conditions of relatively low temperatures and high von Mises stresses.

- The study of the influence of the loading and cooling time on the plastic deformation of the substrate shows that a longer thermal loading will produce higher temperatures and thus a

higher plastic deformation is obtained under the same mechanical loading conditions.

The thesis at hand has proven the potential of numerical methods to realistically model complex production processes such as machining. It can thus be seen as another important step in the direction towards a virtual factory.

5 Literature

[1] Astakhov V.P., Tribology of Metal Cutting Oxford Elsevier 2006.

[2] Stein E., de Bors R., Hughes T.J.R., Encyclopedia of Computational Mechanics John Wiley & Sons 2004.

[3] Teppernegg T., Klünsner T., Angerer P., Tritremmel C., Czettl C., Keckes J., Ebner R., Pippan R., 2014. Evolution of residual stress and damage in coated hard metal milling inserts over the complete tool life, Int. J. Refract. Met. H. 47, p. 80.

[4] "http://www.3ds.com/products-services/simulia/products/abaqus/," Dassult system, Simulia. [Online]. [Accessed 22 2 2016].

[5] Iqbal S.A., Mativenga P.T., Sheikh M.A., 2009. An investigative study of the interface heat transfer coefficient for FE modelling of high speed machining, NED Univ. J. Res. 6, p. 44.

[6] Kagnaya T., Lazard M., Lambert L., Boher C., Cutard T., 2011. Temperature evolution in WC-6% Co cutting tool during turning machining: experiment and finite element simulations, Wseas Trans. Heat Mass Transf. 6, p. 71.

[7] Hor A., Morel F., Lebrun J.L., Germain G., 2013. Modelling identification and application of phe Mech. Mater. 64, p. 91.

[8] Docobu F., Riviere-Lorphevre E nomenological constitutive laws over a large strain rate and temperature range,., Filippi F.,2014. Numerical contribution to the comprehension of saw-toothed Ti6Al4V chip formation in orthogonal cutting, Int. J. Mech. Sci. 81, p. 77.

[9] Pujana J., Arrazola P.J., M'Saoubi R., Chandrasekaran H., 2007. Analysis of the inverse identification of constitutive equations applied in orthogonal cutting process, Int. J. Mach. Tool. Manu 47, p. 2153.

[10] Hor A., Morel F., Lebrun J.L., Germain G., 2013. An experimental investigation of the behavior of steels over large temperature and strain rate ranges, Int. J. Mech. Sci. 67, p. 108.

[11] Pantale O., Bacaria J.-L., Dalverny O., Rakotomalala R., Caperaa S., 2004. 2D and 3D numerical models of metal cutting with damage effects, Comput. method. appl. m., p. 4383.

[12] Molinari A., Cheriguene R., Miguelez H., 2012. Contact variables and thermal effects at the tool–chip interface in orthogonal cutting, Int. J. Solids Struct. 49, p. 3774.

[13] Fontaine M., Devillez A., Moufki A., Dudzinski D., 2006., Predictive force model for ball-end milling and experimental, Int. J. Mach. Tool. Manu. 46, p. 367.

[14] DIN ISO 3369, Impermeable sintered metal materials and hard metals - Determination of density Berlin Beuth 2010.

[15] Kurzweil P., Frenzel B., Gebhard F., Physik Formelsammlung-Für Ingenieure und Naturwissenschaftler Berlin 2008.

[16] Lins W., Kaindl G., Peterlik H., Kromp K., 1999. A novel resonant beam technique to determine the elastic moduli in dependence on orientation and temperature up to 2000°C, Rev. Sci. Instrum. 70, p. 3052.

[17] Meschede D., Gerthsen Physik Berlin 2015.

[18] Erdmann M., Experimentalphysik 4 Berlin 2011.

[19] Saha R., Nix. W.D., 2002.Effects of the substrate on the determination of thin film mechanical properties by nanoindentation, Acta Mater. 50, p. 23.

[20] Oliver W., Pharr G., 1992. An improved technique for determining hardness and elastic modulus using load and displacement sensing indentation experiments, J. Mater. Res. 7, p. 1564.

[21] Chang Y.-Y., We C.-J., 2013. Mechanical properties and impact resistance of multilayered TiAlN/ZrN coatings, Surf. Coat. Tech. 231, p. 62.

[22] Munro R.G., 1997. Evaluated material properties for a sintered alpha- alumina, J. Am. Ceram. Soc. 80, p. 1919.

[23] Pollini I., Mosser A., Parlebas J.C. 2001. Electronic, spectroscopic and elastic properties of early transition metal compounds, Phys. Rep. 355, p. 1.

[24] Kone F., Czarnota C., Haddag B., Nouari M., 2010. Finite element modeling of thermo-mechanical behavior of coatings under extreme contact loading in dry machining, Surf. Coat. Tech. 205, p. 3559.

[25] Slack G.A., Bartram S.F., 1975. Thermal expansion of some diamondlike crystals, J. Appl. Phys., 46, p. 89.

[26] Cahill D.G., Goodson K., Majumdar A., 2002. Thermometry and thermal transport in micro/nanoscale solid-state devices and structures, J. Heat Transfer 124, p. 223 .

[27] Cahill D.G., Ford W.K., Goodson K.E., Mahan G.D., Majumdar A., 2003. Nanoscale thermal transport, J. Appl. Phys. 93, p. 793.

[28] Martan J., Benes P., 2012. Thermal properties of cutting tool coatings at high temperatures, Thermochim. Acta 539, p. 51.

[29] Archer D.G., 1992. Thermodynamic properties of synthetic sapphire (α-Al_2O_3), standard reference material 720 and the effect of temperature scale differences on thermodynamic properties, J. Phys. Chem. Ref. Data 22, p. 1441.

[30] M'Saoubi R., Ruppi S., 2009. Wear and thermal behavior of CVD α-Al_2O_3 and MTCVD Ti(C,N) coatings during machining, CIRP Ann.-Manf. Techn. 58, p. 57.

[31] Grzesik W., 1999. Experimental investigation of the cutting temperature when turning with coated indexable inserts, Int. J. Mach. Tool. Manu. 39, p. 355.

[32] Ruppi S., 2001. Advances in chemically vapor deposited wear resistance coatings, J. Phys. IV France 11, p. 847.

[33] PalDey S., Deevi S.C., 2002. Single layer and multilayer wear resistant coatings of (Ti,Al)N: a review, Mater. Sci. Eng. A-Struct 342, p. 58.

[34] Grzesik W., Nieslony P., 2004. Physics based modelling of interface temperatures in machining with multilayer coated tools at moderate cutting speeds, Int. J. Mach. Tool. Manu. 44, p. 889 .

[35] Shijun Z., Zhangiang L., 2008. An analytical model for transient temperature distribution in coated carbide cutting tools, Int. Commun. Heat. Mass 35, p. 1311.

[36] Grzesik W., Bartoszuk M., Nieslony P., 2005. Finite element modelling of temperature distribution in the cutting zone in turning process with differently

coated tools, J. Mater. Process. Tech. 164-165, p. 1204.

[37] Grzesik W., Bartoszuk M., Nieslony P., 2004. Finite difference analysis of the thermal behavior of coated tools in orthogonal cutting of steels, Int. J. Mach. Tool. Manu. 44, p. 1451.

[38] Pletz M., Daves W., Ossberger H., 2012. A wheel set/crossing model regarding impact, sliding and deformation- Explicit finite element approach, Wear 294-295, p. 446.

[39] Carter F.W., 1926. On the action of a locomotive driving wheel, Proc. R. Soc. A112, p. 151.

[40] Archard J.F., 1953. Contact and Rubbing of Flat Surfaces, J. Appl. Phys. 24, p. 981.

[41] Dante R.C., Vannuci F., Durando P., Galetto E., Kajdas C.K., 2009. Relationship between wear of friction materials and dissipated power density, Tribol. Int., p. 958.

[42] Kim J., Kang S., 2012. Elastic and thermo-physical properties of TiC, TiN, and their intermediate composition alloys using ab initio calculations, J. Alloys Compd. 528, p. 20.

[43] Windover D., Barnat E., Kim J.Y., Nielsen M., Lu T., Kumar A., Bakhru H., 2000. Thin film density determination by multiple radiation energy dispersive X-ray reflectivity, Adv. X-Ray Anal. 42, p. 539 .

[44] Tepernegg T., Angerer P., Klünsner T., Tritremmel C., Czettl C., 2015. Evolution of residual stress in Ti-Al-Ta-N coatings on hard metal milling inserts, Int. J. Refract. Met. H 52, p. 171 .

[45] Teppernegg T., Klünsner T., Tritremmel C., Czettl C., Keckes J., Wroblewski T., Ebner R., Pippan R., 2013. Spatial correlation of tensile residual stress and thermal fatigue damage in coated cemented carbide milling inserts, 18th Plansee Seminar.

[46] Barge M., Hamdi H., Rech J., Bergheau J.-M., 2005. Numerical modeling of orthogonal cutting: influence of numerical parameters, J. Mater. Process. Tech., p. 164 .

Appendix

The material properties of the HM grades in *Abaqus input file* form are presented. The unit system is millimeter, tons, second.

WC 6 wt. % Co:

```
**mm, t, s
************            Material
"Experimental Table"
** Waermeleitfaehigkeit
*Conductivity
 105.97 , 25.2
 91.67 , 250.9
 82.57 , 504.0
 78.83 , 603.4
 75.20 , 702.4
 71.37 , 801.8
 68.33 , 901.5
 67.8 , 1001.4
***********************************
***********************************
***
** Massendichte
*Density
 14.95e-9,
** E-Modul, Poisson-Zahl
*Elastic
 617e3 , 0.2005 , 25
 615.5e3 , 0.2020 , 100
 611.5e3 , 0.2025 , 200
 606e3 , 0.2100 , 300
 600.5e3 , 0.2053 , 400
 592e3 , 0.2093 , 500
 589e3 , 0.2090 , 600
 582e3 , 0.2075 , 700
 573e3 , 0.2075 , 800
 556e3 , 0.2075 , 900
 535.5e3 , 0.2075 , 1000
 499e3 , 0.2075 , 1100
** Waermeausdehnungskoeffizient
*Expansion, zero=20
4.92e-6       ,       100
5.04e-6       ,       197
5.16e-6       ,       294
5.28e-6       ,       391
5.4e-6        ,       488
5.51e-6       ,       585
```

```
5.63e-6       ,       682
5.75e-6       ,       779
5.87e-6       ,       876
5.98e-6       ,       973
6.1e-6        ,       1070
6.22e-6       ,       1167
6.31e-6       ,       1239
6.38e-6       ,       1300
** fraction of inelastic dissipation
rate that appears as a heat flux per
unit volume.
** The default value is 0.9.
*Inelastic Heat Fraction
 0.9,
***********************************
***********************************
***
*plastic
1850.00000, 0,    25
1894.07673, 1.1076E-4   , 25
1957.21097, 2.2941E-4   , 25
2020.34671, 3.4901E-4   , 25
2083.48279, 4.6926E-4   , 25
2146.61872, 5.9013E-4   , 25
2209.75464, 7.1165E-4   , 25
2272.89051, 8.3384E-4   , 25
2336.02637, 9.5676E-4   , 25
2399.16221, 0.00108     , 25
2462.29808, 0.0012      , 25
2525.43392, 0.00133     , 25
2588.56973, 0.00146     , 25
2651.70563, 0.00158     , 25
2714.84147, 0.00171     , 25
2777.97732, 0.00184     , 25
2841.11318, 0.00197     , 25
2904.24900, 0.0021      , 25
2967.38484, 0.00224     , 25
3030.52071, 0.00237     , 25
3093.65655, 0.00251     , 25
3156.79240, 0.00265     , 25
3219.92827, 0.00279     , 25
```

3283.06406, 0.00293   , 25
3346.19992, 0.00307   , 25
3409.33579, 0.00322   , 25
3472.47161, 0.00337   , 25
3535.60744, 0.00352   , 25
3598.74328, 0.00367   , 25
3661.87908, 0.00383   , 25
3725.01494, 0.00399   , 25
3788.15074, 0.00415   , 25
3851.28657, 0.00432   , 25
3914.42240, 0.00449   , 25
3977.55820, 0.00467   , 25
4040.69398, 0.00485   , 25
4103.82980, 0.00504   , 25
4166.96554, 0.00523   , 25
4230.10132, 0.00543   , 25
4293.23714, 0.00563   , 25
4356.37294, 0.00585   , 25
4419.50872, 0.00607   , 25
4482.64457, 0.0063   , 25
4545.78034, 0.00654   , 25
4608.91617, 0.00679   , 25
4672.05195, 0.00705   , 25
4735.18778, 0.00732   , 25
4798.32356, 0.00761   , 25
4861.45933, 0.00791   , 25
4924.59496, 0.00822   , 25
4987.73058, 0.00855   , 25
5050.86607, 0.0089   , 25
5114.00144, 0.00926   , 25
5177.13643, 0.00965   , 25
5240.27110, 0.01007   , 25
5303.40519, 0.01051   , 25
5366.53829, 0.011 , 25
5429.66986, 0.01152   , 25
5492.79881, 0.01211   , 25
5555.92324, 0.01276   , 25
5619.03954, 0.01351   , 25
5682.14064, 0.01438   , 25
5745.21300, 0.01544   , 25
1800.00000, 0.00000,   200
1830.93922, 1.1854E-4   , 200
1894.07528, 2.3471E-4   , 200
1957.21120, 3.5161E-4   , 200
2020.34709, 4.6928E-4   , 200
2083.48297, 5.8781E-4   , 200
2146.61882, 7.0725E-4   , 200
2209.75465, 8.2768E-4   , 200
2272.89049, 9.4921E-4   , 200
2336.02636 , 0.00107   , 200

2399.16219 , 0.0012   , 200
2462.29804 , 0.00132   , 200
2525.43387 , 0.00145   , 200
2588.56972 , 0.00158   , 200
2651.70555 , 0.00171   , 200
2714.84137 , 0.00184   , 200
2777.97721 , 0.00198   , 200
2841.113   , 0.00211   , 200
2904.24875 , 0.00225   , 200
2967.38449 , 0.0024   , 200
3030.52025 , 0.00255   , 200
3093.65595 , 0.0027   , 200
3156.79153 , 0.00286   , 200
3219.92711 , 0.00302   , 200
3283.06257 , 0.00319   , 200
3346.19806 , 0.00336   , 200
3409.33347 , 0.00355   , 200
3472.46892 , 0.00374   , 200
3535.60451 , 0.00395   , 200
3598.74033 , 0.00416   , 200
3661.87637 , 0.00439   , 200
3725.01259 , 0.00463   , 200
3788.14898 , 0.00488   , 200
3851.28534 , 0.00515   , 200
3914.42161 , 0.00543   , 200
3977.55775 , 0.00572   , 200
4040.69375 , 0.00603   , 200
4103.82973 , 0.00635   , 200
4166.96558 , 0.00668   , 200
4230.10139 , 0.00703   , 200
4293.23713 , 0.0074   , 200
4356.3728 , 0.00778   , 200
4419.50829 , 0.00818   , 200
4482.64363 , 0.00861   , 200
4545.77878 , 0.00906   , 200
4608.91344 , 0.00954   , 200
4672.04769 , 0.01005   , 200
4735.18097 , 0.01061   , 200
4798.31281 , 0.01122   , 200
4861.44251 , 0.0119   , 200
4924.56821 , 0.01265   , 200
4987.68705 , 0.01352   , 200
5050.79349 , 0.01453   , 200
5113.87722 , 0.01576   , 200
1600.00000, 0.00000,   400
1641.532,   1.0758E-4 , 400
1704.66784, 2.1735E-4 , 400
1767.80368, 3.2711E-4 , 400
1830.93953, 4.3686E-4 , 400
1894.07537, 5.4661E-4 , 400

```
1957.21059, 6.5819E-4  , 400          1388.98861, 9.9738E-4  , 600
2020.33898, 7.8473E-4  , 400          1431.07919 , 0.00111   , 600
2083.48477, 9.2463E-4  , 400          1473.16975 , 0.00122   , 600
2146.61793 , 0.00107   , 400          1515.26032 , 0.00133   , 600
2209.75407 , 0.00121   , 400          1557.35088 , 0.00144   , 600
2272.89028 , 0.00136   , 400          1599.44143 , 0.00155   , 600
2336.02625 , 0.00151   , 400          1641.53201 , 0.00166   , 600
2399.16212 , 0.00167   , 400          1683.62256 , 0.00178   , 600
2462.29799 , 0.00182   , 400          1725.71314 , 0.00189   , 600
2525.43379 , 0.00198   , 400          1767.8037  , 0.002     , 600
2588.56963 , 0.00214   , 400          1809.89427 , 0.00211   , 600
2651.70544 , 0.00231   , 400          1851.98483 , 0.00222   , 600
2714.84116 , 0.00248   , 400          1894.0754  , 0.00233   , 600
2777.97689 , 0.00265   , 400          1936.16594 , 0.00244   , 600
2841.11252 , 0.00283   , 400          1978.25653 , 0.00255   , 600
2904.24813 , 0.00301   , 400          2020.34708 , 0.00266   , 600
2967.38365 , 0.00321   , 400          2062.38997 , 0.00279   , 600
3030.51911 , 0.00341   , 400          2104.51409 , 0.00293   , 600
3093.65445 , 0.00361   , 400          2146.6222  , 0.0031    , 600
3156.78973 , 0.00383   , 400          2188.70858 , 0.00326   , 600
3219.92494 , 0.00406   , 400          2230.79909 , 0.00344   , 600
3283.06019 , 0.00431   , 400          2272.88993 , 0.00362   , 600
3346.19558 , 0.00457   , 400          2314.98061 , 0.0038    , 600
3409.33115 , 0.00484   , 400          2357.07121 , 0.00399   , 600
3472.467   , 0.00514   , 400          2399.16171 , 0.00418   , 600
3535.60305 , 0.00545   , 400          2441.25213 , 0.00438   , 600
3598.73927 , 0.00579   , 400          2483.34252 , 0.00459   , 600
3661.8755  , 0.00615   , 400          2525.43277 , 0.00481   , 600
3725.01165 , 0.00653   , 400          2567.52292 , 0.00504   , 600
3788.14751 , 0.00694   , 400          2609.61292 , 0.00528   , 600
3851.28309 , 0.00737   , 400          2651.70283 , 0.00553   , 600
3914.41825 , 0.00784   , 400          2693.79256 , 0.0058    , 600
3977.55286 , 0.00834   , 400          2735.88216 , 0.00609   , 600
4040.68655 , 0.00888   , 400          2777.9718  , 0.0064    , 600
4103.81889 , 0.00947   , 400          2820.06157 , 0.00674   , 600
4166.94892 , 0.01013   , 400          2862.15154 , 0.0071    , 600
4230.07506 , 0.01086   , 400          2904.24183 , 0.0075    , 600
4293.19396 , 0.01169   , 400          2946.33241 , 0.00794   , 600
4356.29945 , 0.01266   , 400          2988.42307 , 0.00842   , 600
4419.37805 , 0.01384   , 400          3030.51351 , 0.00894   , 600
4482.40335 , 0.01533   , 400          3072.6035  , 0.00952   , 600
1000.00000, 0.00000,    600          3114.69259 , 0.01016   , 600
1052.26411, 1.0712E-4  , 600          3156.78025 , 0.01087   , 600
1094.35466, 2.1845E-4  , 600          3198.86556 , 0.01166   , 600
1136.44524, 3.2976E-4  , 600          3240.94687 , 0.01257   , 600
1178.5358,  4.4106E-4  , 600          3283.02099 , 0.01364   , 600
1220.62636, 5.5235E-4  , 600          3325.08229 , 0.01492   , 600
1262.71693, 6.6363E-4  , 600          3367.1217  , 0.01652   , 600
1304.80749, 7.7489E-4  , 600          700.000000, 0.00000,    800
1346.89807, 8.8614E-4  , 600          715.53966,  1.802E-4   , 800
```

```
757.63023,  3.5962E-4  , 800
799.72079,  5.4067E-4  , 800
841.81141,  7.235E-4   , 800
883.90198,  9.0827E-4  , 800
925.99249  , 0.0011    , 800
968.08306  , 0.00128   , 800
1010.17362 , 0.00148   , 800
1052.26419 , 0.00167   , 800
1094.35474 , 0.00187   , 800
1136.44529 , 0.00207   , 800
1178.53583 , 0.00228   , 800
1220.62635 , 0.00249   , 800
1262.71681 , 0.0027    , 800
1304.80727 , 0.00293   , 800
1346.89764 , 0.00316   , 800
1388.9879  , 0.00339   , 800
1431.07791 , 0.00364   , 800
1473.16763 , 0.0039    , 800
1515.2568  , 0.00418   , 800
1557.34509 , 0.00448   , 800
1599.43196 , 0.0048    , 800
1641.51682 , 0.00516   , 800
1683.59913 , 0.00555   , 800
1725.67949 , 0.006     , 800
1767.76093 , 0.00653   , 800
1809.84853 , 0.00714   , 800
1851.94437 , 0.00787   , 800
1894.04332 , 0.00871   , 800
1936.13856 , 0.0097    , 800
1978.2267  , 0.01084   , 800
2020.30532 , 0.01218   , 800
2062.36853 , 0.01381   , 800
2104.40368 , 0.01586   , 800
700.00,    0,    900
715.53957, 1.4563E-4  , 900
736.58481, 2.9792E-4  , 900
757.63014, 4.5468E-4  , 900
778.67542, 6.1614E-4  , 900
799.7207,  7.8261E-4  , 900
820.76591, 9.5438E-4  , 900
```

```
841.81127  , 0.00113  , 900
862.85655  , 0.00132  , 900
883.90183  , 0.00151  , 900
904.9471   , 0.0017   , 900
925.99224  , 0.00191  , 900
947.0375   , 0.00212  , 900
968.08296  , 0.00234  , 900
989.12824  , 0.00257  , 900
1010.17353 , 0.00281  , 900
1031.2188  , 0.00306  , 900
1052.2641  , 0.00332  , 900
1073.30889 , 0.0036   , 900
1094.35406 , 0.00389  , 900
1115.39993 , 0.0042   , 900
1136.4443  , 0.00453  , 900
1157.48932 , 0.00488  , 900
1178.53578 , 0.00526  , 900
1199.57915 , 0.00566  , 900
1220.62379 , 0.0061   , 900
1241.66824 , 0.00657  , 900
1262.71227 , 0.0071   , 900
1283.75573 , 0.00769  , 900
1304.80747 , 0.00835  , 900
1325.85274 , 0.00911  , 900
1346.898   , 0.01001  , 900
1367.94323 , 0.01109  , 900
1388.98836 , 0.01246  , 900
1410.03389 , 0.01432  , 900
1431.20148 , 0.01702  , 900
** Waermekapazitaet
*Specific Heat
 0.204e9 , 25.2
 0.256e9 , 250.9
 0.278e9 , 504.0
 0.285e9 , 603.4
 0.293e9 , 702.4
 0.301e9 , 801.8
 0.309e9 , 901.5
 0.311e9 , 1001.4
**
```

WC 8 wt. % Co:

```
**mm, t, s
************      Material
"Experimental Table"
** Waermeleitfaehigkeit
*Conductivity
 95.1 , 25.2
 85.2 , 250.9
```

```
77.8 , 504.0
74.6 , 603.4
71.4 , 702.4
68.2 , 801.8
66.3 , 901.5
65.4 , 1001.4
```

```
********************************         1963.94694, 4.8E-4,     25
********************************         2027.57405, 6.1E-4,     25
***                                     2091.21931, 7.5E-4,     25
** Massendichte                         2154.88459, 8.8E-4,     25
*Density                                2218.56932, 0.00102,    25
 14.98e-9,                              2282.27367, 0.00116,    25
** E-Modul, Poisson-Zahl                2345.99840, 0.00130,    25
*Elastic                                2409.74326, 0.00144,    25
 599e3 , 0.20750 , 25                   2473.50919, 0.00158,    25
 596e3 , 0.20850 , 100                  2537.29643, 0.00173,    25
 591e3 , 0.20625 , 200                  2601.10571, 0.00187,    25
 586e3 , 0.20850 , 300                  2664.93740, 0.00202,    25
 579e3 , 0.20875 , 400                  2728.79252, 0.00217,    25
 573e3 , 0.21225 , 500                  2792.67174, 0.00232,    25
 567e3 , 0.21450 , 600                  2856.57538, 0.00247,    25
 560e3 , 0.21400 , 700                  2920.50438, 0.00262,    25
 552e3 , 0.21400 , 800                  2984.46067, 0.00278,    25
 536e3 , 0.21400 , 900                  3048.44440, 0.00294,    25
 514e3 , 0.21400 , 1000                 3112.45727, 0.00310,    25
 485e3 , 0.21400 , 1100                 3176.50080, 0.00326,    25
** Waermeausdehnungskoeffizient         3240.57657, 0.00343,    25
*Expansion, zero=20                     3304.68616, 0.00360,    25
4.58e-6      ,      100                 3368.83205, 0.00378,    25
4.72e-6      ,      197                 3433.01669, 0.00396,    25
4.85e-6      ,      294                 3497.24242, 0.00415,    25
4.99e-6      ,      391                 3561.51232, 0.00434,    25
5.12e-6      ,      488                 3625.83000, 0.00454,    25
5.26e-6      ,      585                 3690.19932, 0.00474,    25
5.39e-6      ,      682                 3754.62383, 0.00496,    25
5.52e-6      ,      779                 3819.10882, 0.00518,    25
5.66e-6      ,      876                 3883.65867, 0.00541,    25
5.79e-6      ,      973                 3948.27947, 0.00565,    25
5.93e-6      ,      1070                4012.97560, 0.00591,    25
6.06e-6      ,      1167                4077.75484, 0.00617,    25
6.16e-6      ,      1239                4142.62411, 0.00645,    25
6.24e-6      ,      1300                4207.59085, 0.00674,    25
** fraction of inelastic dissipation    4272.66516, 0.00705,    25
rate that appears as a heat flux per    4337.85779, 0.00738,    25
unit volume.                            4403.18347, 0.00773,    25
** The default value is 0.9.            4468.66007, 0.00810,    25
*Inelastic Heat Fraction                4534.31175, 0.00850,    25
 0.9,                                   4600.16965, 0.00894,    25
********************************         4666.27864, 0.00941,    25
********************************         4732.70324, 0.00994,    25
***                                     4799.54116, 0.01055,    25
*plastic                                4866.95402, 0.01126,    25
1750.00000, 0,    25                    4935.23105, 0.01213,    25
1773.24093, 1.1E-4,    25               5004.97637, 0.01328,    25
1836.76950, 2.2E-4,    25               5078.36180, 0.01505,    25
1900.34203, 3.5E-4,    25               5158.35553, 0.01809,    25
```

78

1740.00000,	0.00000,	200	1964.46998,	7.1E-4,	400
1773.20402,	1.2E-4,	200	2028.15062,	8.7E-4,	400
1836.76386,	2.5E-4,	200	2091.87835,	0.00103,	400
1900.37184,	3.9E-4,	200	2155.62996,	0.00120,	400
1963.99261,	5.3E-4,	200	2219.41302,	0.00137,	400
2027.63645,	6.7E-4,	200	2283.22743,	0.00155,	400
2091.30177,	8.2E-4,	200	2347.07482,	0.00173,	400
2154.98909,	9.6E-4,	200	2410.95821,	0.00191,	400
2218.69929,	0.00111,	200	2474.87996,	0.00211,	400
2282.43344,	0.00126,	200	2538.84368,	0.00231,	400
2346.19226,	0.00141,	200	2602.85380,	0.00251,	400
2409.97709,	0.00157,	200	2666.91530,	0.00273,	400
2473.78926,	0.00173,	200	2731.03345,	0.00296,	400
2537.62984,	0.00189,	200	2795.21573,	0.00320,	400
2601.50074,	0.00205,	200	2859.47071,	0.00345,	400
2665.40402,	0.00222,	200	2923.80696,	0.00372,	400
2729.34155,	0.00240,	200	2988.23572,	0.00401,	400
2793.31590,	0.00258,	200	3052.76805,	0.00433,	400
2857.32978,	0.00276,	200	3117.41759,	0.00466,	400
2921.38691,	0.00295,	200	3182.19685,	0.00503,	400
2985.49095,	0.00315,	200	3247.12240,	0.00542,	400
3049.64554,	0.00336,	200	3312.21237,	0.00585,	400
3113.85618,	0.00358,	200	3377.49119,	0.00632,	400
3178.12759,	0.00381,	200	3442.99093,	0.00684,	400
3242.46566,	0.00405,	200	3508.75588,	0.00741,	400
3306.87619,	0.00430,	200	3574.85010,	0.00806,	400
3371.36566,	0.00456,	200	3641.37116,	0.00880,	400
3435.94138,	0.00484,	200	3708.47862,	0.00967,	400
3500.61049,	0.00514,	200	3776.46108,	0.01076,	400
3565.38257,	0.00546,	200	3845.92650,	0.01221,	400
3630.26501,	0.00579,	200	3919.03862,	0.01445,	400
3695.27062,	0.00615,	200	3999.30964,	0.01845,	400
3760.41058,	0.00653,	200	1100.00000,	0.00000,	600
3825.70029,	0.00693,	200	1139.35281,	1.2E-4,	600
3891.15844,	0.00737,	200	1181.68279,	2.3E-4,	600
3956.81048,	0.00784,	200	1224.02350,	3.4E-4,	600
4022.68844,	0.00835,	200	1266.37474,	4.5E-4,	600
4088.83946,	0.00892,	200	1308.73626,	5.7E-4,	600
4155.33166,	0.00955,	200	1351.10833,	6.8E-4,	600
4222.26798,	0.01026,	200	1393.49158,	8.0E-4,	600
4289.81987,	0.01110,	200	1435.88590,	9.1E-4,	600
4358.29273,	0.01214,	200	1478.29150,	0.00103,	600
4428.31936,	0.01350,	200	1520.70888,	0.00115,	600
4501.98801,	0.01556,	200	1563.13828,	0.00127,	600
4582.33870,	0.01906,	200	1605.57974,	0.00139,	600
1700.00000,	0.00000,	400	1648.03423,	0.00151,	600
1710.01439,	1.4E-4,	400	1690.50177,	0.00164,	600
1773.59637,	2.8E-4,	400	1732.98294,	0.00176,	600
1837.19944,	4.2E-4,	400	1775.47848,	0.00189,	600
1900.82332,	5.7E-4,	400	1817.98900,	0.00202,	600

1860.51517, 0.00216,   600
1903.05789, 0.00229,   600
1945.61843, 0.00243,   600
1988.19824, 0.00257,   600
2030.79834, 0.00272,   600
2073.41180, 0.00288,   600
2116.11082, 0.00305,   600
2158.84859, 0.00324,   600
2201.61622, 0.00344,   600
2244.42793, 0.00365,   600
2287.28705, 0.00388,   600
2330.19895, 0.00411,   600
2373.17281, 0.00437,   600
2416.21780, 0.00465,   600
2459.34658, 0.00495,   600
2502.57412, 0.00528,   600
2545.91954, 0.00564,   600
2589.40786, 0.00605,   600
2633.07353, 0.00652,   600
2676.96679, 0.00705,   600
2721.16756, 0.00769,   600
2765.81752, 0.00847,   600
2811.20674, 0.00951,   600
2858.46611, 0.01109,   600
2909.48266, 0.01395,   600
2968.36451, 0.01937,   600
250.000000, 0.00000,   800
252.788950, 1.86835E-4, 800
294.977340, 3.70012E-4, 800
337.180850, 5.60012E-4, 800
379.400670, 7.50012E-4, 800
421.637200, 9.50012E-4, 800
463.890600, 0.00114,   800
506.161160, 0.00133,   800
548.449210, 0.00153,   800
590.755120, 0.00173,   800
633.079190, 0.00193,   800
675.422040, 0.00214,   800
717.784030, 0.00234,   800
760.166010, 0.00255,   800
802.568640, 0.00276,   800
844.992840, 0.00298,   800
887.439700, 0.00320,   800
929.910720, 0.00343,   800
972.407450, 0.00367,   800
1014.93228, 0.00391,   800
1057.48793, 0.00416,   800
1100.07802, 0.00443,   800
1142.70741, 0.00471,   800
1185.38281, 0.00501,   800

1228.11347, 0.00533,   800
1270.91206, 0.00569,   800
1313.79571, 0.00609,   800
1356.78584, 0.00654,   800
1399.90504, 0.00705,   800
1443.17813, 0.00765,   800
1486.63974, 0.00833,   800
1530.34888, 0.00915,   800
1574.41580, 0.01017,   800
1619.30451, 0.01156,   800
1665.62997, 0.01379,   800
1717.12703, 0.01892,   800
200.00,   0,   900
210.65697, 9.6911E-5, 900
231.74512, 1.97381E-4, 900
252.83733, 2.87381E-4, 900
273.93360, 3.87381E-4, 900
295.03430, 4.87381E-4, 900
316.14740, 6.07381E-4, 900
337.26822, 7.37381E-4, 900
358.39469, 8.77381E-4, 900
379.53243, 0.00102,   900
400.67760, 0.00117,   900
421.82972, 0.00132,   900
442.98942, 0.00148,   900
464.15707, 0.00163,   900
485.33310, 0.00179,   900
506.51813, 0.00196,   900
527.71284, 0.00213,   900
548.91817, 0.00231,   900
570.13542, 0.00249,   900
591.36633, 0.00269,   900
612.61344, 0.00290,   900
633.88063, 0.00313,   900
655.17299, 0.00337,   900
676.49414, 0.00365,   900
697.84389, 0.00394,   900
719.22127, 0.00426,   900
740.62725, 0.00460,   900
762.06473, 0.00497,   900
783.53759, 0.00536,   900
805.05208, 0.00578,   900
826.61674, 0.00624,   900
848.24452, 0.00675,   900
869.95474, 0.00734,   900
891.77953, 0.00803,   900
913.77706, 0.00890,   900
936.21775, 0.01011,   900
959.47359, 0.01218,   900
985.83891, 0.01730,   900

```
** Waermekapazitaet
*Specific Heat
 0.19533e9 , 25.2
 0.24467e9 , 250.9
 0.267e9 , 504.0
 0.27333e9 , 603.4
```

 0.27867e9 , 702.4
 0.285e9 , 801.8
 0.292e9 , 901.5
 0.297e9 , 1001.4
**

WC 10.5 wt. % Co:

```
**mm, t, s
************    Material
"Experimental Table"
** Waermeleitfaehigkeit
*Conductivity
 89.97 , 25.2
 80.90 , 250.9
 74.83 , 504.0
 72.27 , 603.4
 69.57 , 702.4
 66.83 , 801.8
 63.77 , 901.5
 65.57 , 1001.4
**********************************
**********************************
***
** Massendichte
*Density
 14.4e-9,
** E-Modul, Poisson-Zahl
*Elastic
 566.25e3 , 0.22775 , 25
 562.25e3 , 0.23400 , 100
 561e3 , 0.22975 , 200
 551.5e3 , 0.22975 , 300
 545e3 , 0.22875 , 400
 540e3 , 0.23550 , 500
 533.25e3 , 0.23400 , 600
 525.75e3 , 0.23300 , 700
 515.33e3 , 0.23300 , 800
 493.33e3 , 0.23300 , 900
 471.5e3 , 0.23300 , 1000
 436e3 , 0.23300 , 1100
** Waermeausdehnungskoeffizient
*Expansion, zero=20
4.9e-6       ,      100
5.05e-6      ,      197
5.19e-6      ,      294
5.34e-6      ,      391
5.49e-6      ,      488
```

```
5.63e-6      ,      585
5.78e-6      ,      682
5.93e-6      ,      779
6.07e-6      ,      876
6.22e-6      ,      973
6.37e-6      ,      1070
6.51e-6      ,      1167
6.62e-6      ,      1239
6.71e-6      ,      1300
** fraction of inelastic dissipation
rate that appears as a heat flux per
unit volume.
** The default value is 0.9.
*Inelastic Heat Fraction
 0.9,
**********************************
**********************************
***
*plastic
1400.00000, 0,    25
1452.12447, 1.229E-4    , 25
1515.26031, 2.4463E-4   , 25
1578.39616, 3.6635E-4   , 25
1641.53201, 4.8805E-4   , 25
1704.66786, 6.0975E-4   , 25
1767.8037,  7.3143E-4   , 25
1830.93956, 8.5311E-4   , 25
1894.06479, 9.8125E-4   , 25
1957.20947 , 0.00112    , 25
2020.34822 , 0.00127    , 25
2083.48223 , 0.00143    , 25
2146.61851 , 0.00158    , 25
2209.75457 , 0.00174    , 25
2272.89048 , 0.00189    , 25
2336.02638 , 0.00205    , 25
2399.16226 , 0.00221    , 25
2462.29811 , 0.00237    , 25
2525.43399 , 0.00253    , 25
2588.56983 , 0.0027     , 25
2651.70566 , 0.00287    , 25
2714.84152 , 0.00304    , 25
```

```
2777.97737 , 0.00321  , 25        2399.1621   , 0.00243  , 200
2841.11319 , 0.00338  , 25        2462.29788  , 0.00262  , 200
2904.24902 , 0.00356  , 25        2525.43364  , 0.00282  , 200
2967.38485 , 0.00374  , 25        2588.56936  , 0.00302  , 200
3030.52067 , 0.00393  , 25        2651.70507  , 0.00323  , 200
3093.65645 , 0.00412  , 25        2714.8407   , 0.00345  , 200
3156.79223 , 0.00431  , 25        2777.97629  , 0.00368  , 200
3219.92801 , 0.00451  , 25        2841.11186  , 0.00391  , 200
3283.06374 , 0.00471  , 25        2904.24739  , 0.00416  , 200
3346.19945 , 0.00493  , 25        2967.38286  , 0.00442  , 200
3409.33511 , 0.00515  , 25        3030.5184   , 0.00469  , 200
3472.4708  , 0.00537  , 25        3093.6539   , 0.00497  , 200
3535.60641 , 0.00561  , 25        3156.78953  , 0.00527  , 200
3598.74195 , 0.00585  , 25        3219.92525  , 0.00559  , 200
3661.87761 , 0.00611  , 25        3283.0611   , 0.00593  , 200
3725.01319 , 0.00638  , 25        3346.19708  , 0.00629  , 200
3788.14883 , 0.00666  , 25        3409.333    , 0.00667  , 200
3851.28449 , 0.00696  , 25        3472.46891  , 0.00708  , 200
3914.42018 , 0.00728  , 25        3535.60479  , 0.00751  , 200
3977.5559  , 0.00761  , 25        3598.74047  , 0.00797  , 200
4040.69163 , 0.00797  , 25        3661.87591  , 0.00846  , 200
4103.82734 , 0.00834  , 25        3725.011    , 0.00899  , 200
4166.96285 , 0.00874  , 25        3788.14551  , 0.00955  , 200
4230.09824 , 0.00917  , 25        3851.27918  , 0.01017  , 200
4293.23324 , 0.00962  , 25        3914.41152  , 0.01084  , 200
4356.36775 , 0.01011  , 25        3977.5415   , 0.01158  , 200
4419.50129 , 0.01064  , 25        4040.66746  , 0.01242  , 200
4482.63349 , 0.01122  , 25        4103.78614  , 0.01337  , 200
4545.76318 , 0.01186  , 25        4166.89094  , 0.01449  , 200
4608.88865 , 0.01258  , 25        4229.96879  , 0.01585  , 200
4672.00605 , 0.01339  , 25        1400.00000, 0.00000,    400
4735.10797 , 0.01434  , 25        1452.12447, 1.2366E-4  , 400
4798.17887 , 0.0155   , 25        1515.26032, 2.4325E-4  , 400
4861.18647 , 0.01697  , 25        1578.39576, 3.6427E-4  , 400
1400.00000, 0.00000,    200       1641.51478, 5.0957E-4  , 400
1452.12446, 1.1479E-4  , 200      1704.66722, 6.7576E-4  , 400
1515.2603, 2.3443E-4   , 200      1767.80251, 8.4702E-4  , 400
1578.39617, 3.5405E-4  , 200      1830.93904 , 0.00102   , 400
1641.53201, 4.7367E-4  , 200      1894.07522 , 0.0012    , 400
1704.66787, 5.9327E-4  , 200      1957.21116 , 0.00138   , 400
1767.8036, 7.163E-4    , 200      2020.34701 , 0.00156   , 400
1830.92547, 8.6152E-4  , 200      2083.48281 , 0.00175   , 400
1894.07734 , 0.00102   , 200      2146.61856 , 0.00195   , 400
1957.21016 , 0.00119   , 200      2209.75428 , 0.00215   , 400
2020.34659 , 0.00136   , 200      2272.88992 , 0.00235   , 400
2083.48279 , 0.00153   , 200      2336.02551 , 0.00257   , 400
2146.61874 , 0.0017    , 200      2399.16094 , 0.00279   , 400
2209.75465 , 0.00188   , 200      2462.29626 , 0.00302   , 400
2272.89048 , 0.00206   , 200      2525.43145 , 0.00326   , 400
2336.02632 , 0.00224   , 200      2588.5664   , 0.00352   , 400
```

```
2651.7011    , 0.00379  , 400      2693.69684  , 0.00919   , 600
2714.83555   , 0.00408  , 400      2735.71414  , 0.01049   , 600
2777.9699    , 0.00438  , 400      2777.6635   , 0.01227   , 600
2841.10416   , 0.00472  , 400      2820.06343  , 0.01513   , 600
2904.23866   , 0.00508  , 400      550.000000, 0.00000,     800
2967.37357   , 0.00547  , 400      589.26801,  2.2684E-4  , 800
3030.50904   , 0.0059   , 400      631.35857,  4.5489E-4  , 800
3093.64495   , 0.00637  , 400      673.44912,  6.8678E-4  , 800
3156.78099   , 0.00689  , 400      715.53968,  9.2306E-4  , 800
3219.91673   , 0.00745  , 400      757.63021   , 0.00116   , 800
3283.05158   , 0.00807  , 400      799.72071   , 0.00141   , 800
3346.18494   , 0.00876  , 400      841.81119   , 0.00167   , 800
3409.31589   , 0.00953  , 400      883.90161   , 0.00193   , 800
3472.44267   , 0.01039  , 400      925.99191   , 0.0022    , 800
3535.56196   , 0.01138  , 400      968.08203   , 0.00248   , 800
3598.66701   , 0.01255  , 400      1010.17188  , 0.00278   , 800
3661.74369   , 0.01396  , 400      1052.26123  , 0.00309   , 800
3724.76389   , 0.01578  , 400      1094.34978  , 0.00343   , 800
1300.00000, 0.00000,     600      1136.43708  , 0.00379   , 800
1388.98863, 1.1642E-4  , 600      1178.52255  , 0.00418   , 800
1431.07918, 2.3896E-4  , 600      1220.60581  , 0.00463   , 800
1473.16972, 3.6362E-4  , 600      1262.68738  , 0.00513   , 800
1515.26029, 4.9059E-4  , 600      1304.76944  , 0.00571   , 800
1557.35082, 6.2009E-4  , 600      1346.85502  , 0.00639   , 800
1599.44137, 7.5234E-4  , 600      1388.9443   , 0.00719   , 800
1641.53191, 8.8763E-4  , 600      1431.03255  , 0.00813   , 800
1683.62242   , 0.00103  , 600      1473.11186  , 0.00925   , 800
1725.71291   , 0.00117  , 600      1515.16972  , 0.01063   , 800
1767.80341   , 0.00132  , 600      1557.17692  , 0.01238   , 800
1809.89387   , 0.00147  , 600      1599.44004  , 0.01487   , 800
1851.98429   , 0.00162  , 600      1641.52282  , 0.01905   , 800
1894.07469   , 0.00178  , 600      300.00,       0,     900
1936.16503   , 0.00195  , 600      357.7677,   1.6569E-4  , 900
1978.2553    , 0.00213  , 600      378.81409,  3.5443E-4  , 900
2020.34548   , 0.00231  , 600      399.86024,  5.483E-4   , 900
2062.43553   , 0.00251  , 600      420.90561,  7.4512E-4  , 900
2104.52543   , 0.00271  , 600      441.95093,  9.4531E-4  , 900
2146.61512   , 0.00293  , 600      462.9962    , 0.00115   , 900
2188.70456   , 0.00316  , 600      484.04141   , 0.00136   , 900
2230.79376   , 0.00341  , 600      505.08656   , 0.00157   , 900
2272.88262   , 0.00369  , 600      526.13159   , 0.0018    , 900
2314.97119   , 0.00398  , 600      547.17633   , 0.00203   , 900
2357.05944   , 0.00431  , 600      568.22056   , 0.00228   , 900
2399.14736   , 0.00467  , 600      589.26388   , 0.00255   , 900
2441.23496   , 0.00508  , 600      610.30609   , 0.00284   , 900
2483.32203   , 0.00554  , 600      631.34807   , 0.00316   , 900
2525.40813   , 0.00606  , 600      652.39254   , 0.00352   , 900
2567.49215   , 0.00665  , 600      673.44086   , 0.00393   , 900
2609.57192   , 0.00735  , 600      694.48996   , 0.00438   , 900
2651.64318   , 0.00818  , 600      715.53721   , 0.00488   , 900
```

```
736.58304   , 0.00541   , 900
757.62809   , 0.00598   , 900
778.67255   , 0.00661   , 900
799.71617   , 0.00729   , 900
820.7584    , 0.00804   , 900
841.798     , 0.0089    , 900
862.83206   , 0.0099    , 900
883.85349   , 0.0111    , 900
904.84302   , 0.01266   , 900
925.99106   , 0.01491   , 900
947.02921   , 0.01888   , 900
** Waermekapazitaet
*Specific Heat
 0.21e9 , 25.2
 0.26e9 , 250.9
 0.286e9 , 504.0
 0.293e9 , 603.4
 0.301e9 , 702.4
 0.314e9 , 801.8
 0.326e9 , 901.5
 0.33e9 , 1001.4
**
```